Geophys. J. Int. (1991) **106,** 433–490

Active tectonics of the north and central Aegean Sea

Tuncay Taymaz, James Jackson and Dan McKenzie
Department of Earth Sciences, Bullard Laboratories, Madingley Road, Cambridge CB3 0EZ, *UK*

Accepted 1991 March 1. Received 1991 February 27; in original form 1990 August 10

SUMMARY

In this paper we examine the connection between the westward motion of Turkey relative to Europe and the extension in and around the Aegean Sea. The principal new data available since the last attempt to synthesize the tectonics of this region by McKenzie (1978) are much improved focal mechanisms of earthquakes, constrained by *P* and *SH* body wave modelling as well as by first motions. These mechanisms show that the faulting in the western part of the Aegean region is mostly extensional in nature, on normal faults with a NW to WNW strike and with slip vectors directed NNW to NNE. There is evidence from palaeomagnetism that this western region rotates clockwise relative to stable Europe. In the central and eastern Aegean, and in NW Turkey, distributed right-lateral strike–slip is more prevalent, on faults trending NE to ENE, and with slip vectors directed NE. Palaeomagnetic data in this eastern region is more ambiguous, but consistent with very small or no rotations in the northern part and possibly anticlockwise rotations, relative to Europe, in the south. The strike–slip faulting that enters the central Aegean from the east appears to end abruptly in the SW against the NW-trending normal faults of Greece.

The kinematics of the deformation is controlled by three factors: the westward motion of Turkey relative to Europe; the continental collision between NW Greece–Albania and the Apulia–Adriatic platform in the west; and the presence of the Hellenic subduction zone to the south. As the right-lateral slip on the North Anatolian Fault enters the Aegean region it splays out, becoming distributed on several parallel faults. The continental shortening in NW Greece and Albania does not allow the rotation of the western margin of the region to be rapid enough to accommodate this distributed E–W right-lateral shear, and thus leads to E–W shortening in the northern Aegean, which is compensated by N–S extension as the southern Aegean margin can move easily over the Hellenic subduction zone. The dynamics of the system, once initiated, is self-sustaining, being driven by the high topography in eastern Turkey and by the roll-back of the subducted slab beneath the southern Aegean.

The geometry of the deformation resembles the behaviour of a system of broken slats attached to margins that rotate. In spite of its extreme simplicity, a simple model of such broken slats is able to reproduce quantitatively most of the features of the instantaneous velocity field in the Aegean region, including: the slip vectors and nature of the faulting in the eastern and western parts; the senses and approximate rates of rotation; the overall extensional velocity across the Aegean; and the distribution of strain rates, as seen in the seismicity and topography or bathymetry, and using geodetic measurements.

As part of this study, we re-examined the relation between the surface faulting and the focal parameters determined seismologically for the three large 1981 Gulf of Corinth earthquakes, and reassessed the evidence for associating particular earthquakes in the sequence with observed surface faulting. An important result is that in one of the events there is a resolvable discrepancy between the slip vector measured at the surface and that determined from the seismic body waves.

Key words: continental tectonics, earthquakes, faulting, Greece, kinematics, Mediterranean, Turkey.

1 INTRODUCTION

The Aegean Sea, and its surrounding coastal areas of Greece and western Turkey, is one of the most seismically active and rapidly deforming regions on the continents (Fig. 1). This paper is concerned with the active tectonics of the north and central Aegean, which is dominated by the westward motion of Turkey and the southwestward motion of the southern Aegean, both relative to Eurasia (Fig. 2 and McKenzie 1972, 1978; Le Pichon & Angelier 1979, 1981). The westward motion of Turkey relative to Eurasia is in turn related to the collision between Arabia and Eurasia in the Caucasus and eastern Turkey, which is thought to have begun about 12 Myr ago in the mid-Miocene (Dewey *et al.* 1986; Philip *et al.* 1989). The thickened crust in eastern Turkey provides the gravitational potential energy, or buoyancy force, that drives Turkey westwards, most of this motion being accommodated on the North and East Anatolian strike–slip fault systems (Ketin 1948; McKenzie 1972; Şengör, Görür & Şaroğlu 1985). The seismically active regions of western Turkey, eastern and northern Greece and the north Aegean Sea have lower elevation (Fig. 3) and thinner crust (Makris & Stobbe 1984) than the Anatolian plateau of central Turkey. These western regions are dominated by extension, as the southern Aegean Sea moves in a roughly southwest direction relative to Eurasia. This extension cannot be driven by the buoyancy forces in eastern Turkey, and is thought to be driven principally by the 'roll-back' of the subducting slab beneath the southern Aegean (McKenzie 1978; Le Pichon 1982), as it sinks into the mantle with a component of velocity normal to its surface: this, too, is a form of buoyancy force that releases gravitational potential energy.

McKenzie (1972) realized that the westward motion of Turkey relative to Eurasia was accommodated by shortening in the Hellenic Trench, as the southern Aegean overrides the Mediterranean sea-floor. For this reason he suggested that the strike–slip faulting associated with the North Anatolian Fault system continued through the North Aegean and central Greece to link up with the northwestern end of the Hellenic Trench system near the Ionian islands (Fig. 2b). The manner in which this was originally suggested to occur (McKenzie 1972) is now known to be too simplistic

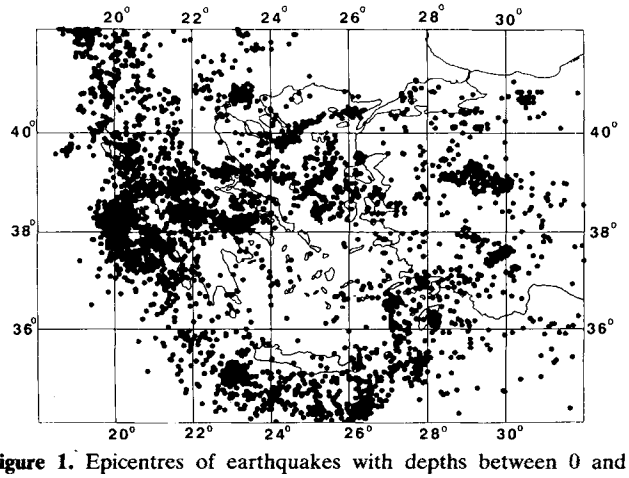

Figure 1. Epicentres of earthquakes with depths between 0 and 50 km reported by the USGS PDE during the period 1963 to 1988.

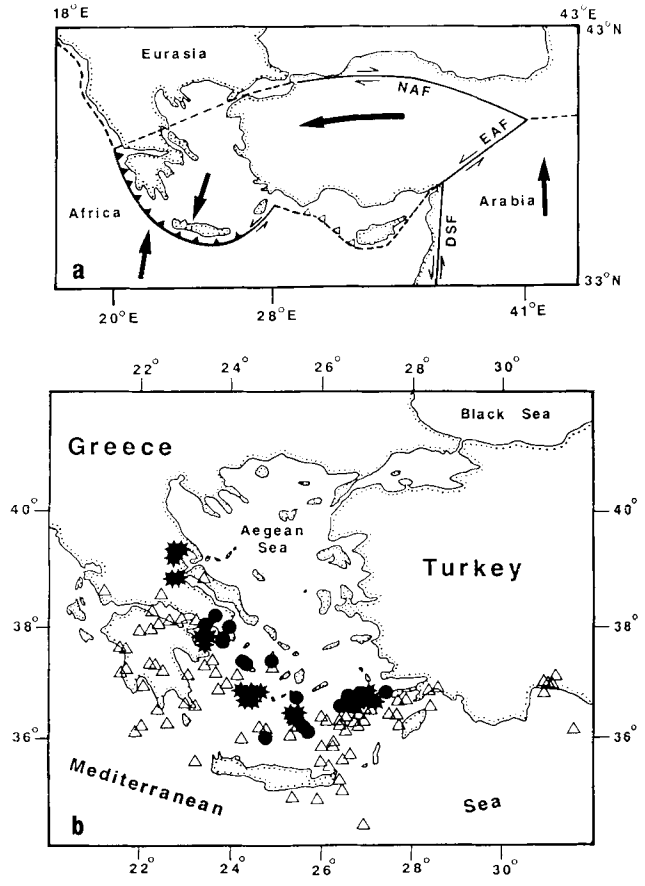

Figure 2. (a) Sketch to show the motions of the Arabian and African plates, central Turkey, and the southern Aegean Sea, relative to Europe. The dashed line in the north Aegean is not a plate boundary: it joins the end of the North Anatolian Fault (NAF) to the northern end of the Hellenic Trench (shown as a thrust), and emphasizes that the westward motion of Turkey is accommodated partly by convergence along the west and southwest coast of Greece and Albania. EAF: East Anatolian Fault; DSF: Dead Sea Fault. (b) Epicentres of earthquakes in the depth range 100–150 km (open triangles) and deeper than 150 km (filled circles), indicating the position of the slab associated with the Hellenic subduction zone. Quaternary volcanoes are marked by stars.

(McKenzie 1978): there is no single strike–slip fault with a NE–SW strike in central Greece, where the tectonics is dominated by normal faulting with a WNW–ESE strike (Mercier *et al.* 1976; McKenzie 1978; Jackson & McKenzie 1983; Roberts & Jackson 1991). McKenzie's (1972) reasoning was nonetheless correct: the NE–SW motion must cross central Greece and the north Aegean, though the manner in which it does so is more complicated than was at first thought, and involves rotations of blocks about both vertical and horizontal axes (McKenzie & Jackson 1983, 1986; Kissel, Laj & Mazaud 1986; Kissel & Laj 1988; Kissel *et al.* 1989). The onset of this NE–SW right-lateral shear in the Aegean is thought to have taken place about 10 Myr ago (Mercier *et al.* 1991).

East of about longitude 31°E the North Anatolian Fault system has a narrow and localized character, defined most obviously by the surface ruptures along almost its entire 1000 km length that were associated with a series of large

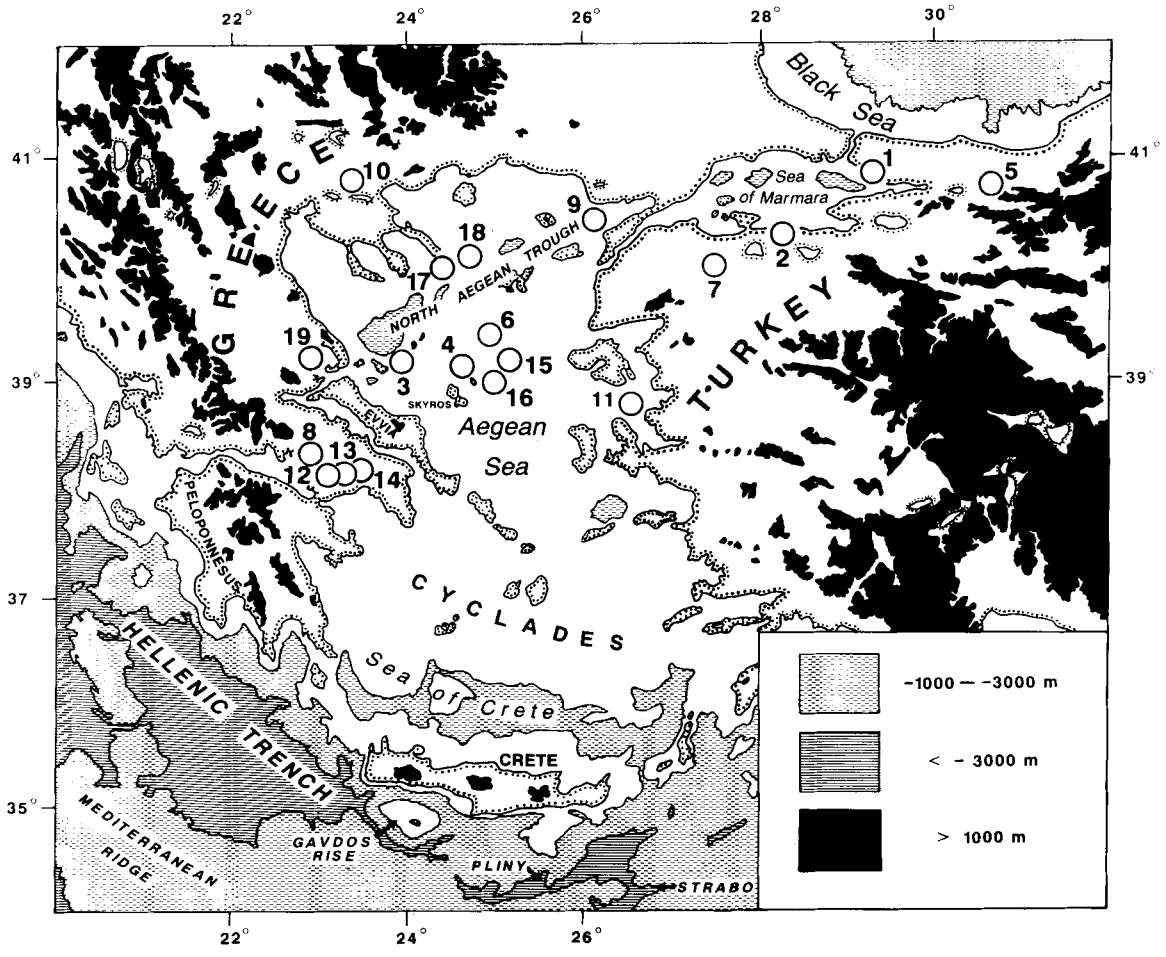

Figure 3. Topographic and bathymetric map of the Aegean region, showing the locations (open circles) of the earthquakes whose waveforms we studied. Numbers identify the events in Table 1.

earthquakes between 1939 and 1967 (Ketin 1948; Ambraseys 1970). West of 31°E, within the Aegean extensional province, the North Anatolian Fault system appears to branch into a series of sub-parallel strands that cross NW Turkey and the north Aegean Sea (McKenzie 1978; Dewey & Şengör 1979; Lybéris 1984; Barka & Kadinsky-Cade 1988). Within this same region, many normal faults are also known to be active, from geomorphological, seismological, and marine geophysical observations (McKenzie 1978; Lalechos & Savoyat 1979; Brooks & Ferentinos 1980; Jackson *et al.* 1982a; Lybéris 1984). There is a variety of estimates of present deformation rates in the region (see Jackson & McKenzie 1988b for a review), based on either kinematic arguments (McKenzie 1978; Le Pichon & Angelier 1979), seismic moment rates (Jackson & McKenzie 1988a,b; Ekström & England 1989; Main & Burton 1989), or, more recently by direct measurement using satellite laser-ranging (Sellers & Cross 1989).

Likely N–S extension rates across the Aegean as a whole are in the range 40–60 mm yr^{-1}, much of which might occur in the north and central Aegean where the seismicity is most intense (Fig. 1). Jackson & McKenzie (1984) used slip vectors of earthquakes on the North Anatolian Fault to define a pole of rotation of Turkey relative to Eurasia. Based on this pole, the motion of Turkey relative to Eurasia at the longitude of the North Aegean Trough would be in the direction 250°. The magnitude of the velocity is estimated to be about 32 mm yr^{-1} (Jackson & McKenzie 1988b), but this is based on an interpretation of the motions in eastern Turkey, and is probably an upper bound.

In this paper we will re-examine the tectonics of the north and central Aegean in an attempt to improve our understanding of how the westward motion of Turkey and the southwestward motion of the Aegean (relative to Eurasia) are related when the deformation changes from being localized (east of 31°E) to diffuse (west of 31°E). Our principal new data are much improved focal mechanisms of earthquakes, which are based on body waveform analysis and are better constrained than the mechanisms based solely on first motion polarities that were already available (McKenzie 1972, 1978; Jackson, King & Vita-Finzi 1982b; Lybéris & Deschamps 1982). These data allow us to discuss the slip vectors in the earthquakes with much more confidence. We also make use of several other studies that have been published since the last attempt to synthesize the relevant tectonic data by McKenzie (1978), which include field studies of faulting in earthquakes, active geomorphology, palaeomagnetism, and a variety of marine geophysical observations. The various geographical locations mentioned in the text are shown in Fig. 9(b).

2 EARTHQUAKE SOURCE MECHANISMS

2.1 Data reduction

McKenzie (1972, 1978), Jackson *et al.* (1982b), Lybéris & Deschamps (1982) and Jackson & McKenzie (1984), among others, have all published first motion fault plane solutions of earthquakes in the north Aegean region. Jackson & White (1989) replotted the focal spheres of some of McKenzie's earlier first motion solutions using a crustal velocity, rather than a mantle velocity, to calculate take-off angles of ray paths at the focus. These solutions were good enough to reveal the general pattern and character of faulting, but can rarely constrain the slip vector tightly, especially for the normal faulting events. We aimed to improve the constraint on focal parameters using waveform data. We were able to examine 17 earthquakes in detail, and there were another two that had been examined, using the same algorithm and procedure, by Liotier (1989). The locations of these 19 events are shown in Fig. 3 and Table 1. There were another 20 earthquakes (Table 2) for which centroid moment tensor (CMT) solutions were published by Ekström & England (1989) or in the Preliminary Determination of Epicentres (PDE) by the US Geological Survey (USGS). Of these 20 events, 18 produced long-period waveforms that were too small to analyse using our procedure, while two of them (numbers 5* and 10* in Table 2) occurred shortly after much larger events elsewhere whose surface waves obscured the body waveforms of interest to us. Later in the paper we compare the mechanisms of the events analysed by ourselves and Liotier (in Table 1) with those reported by Ekström & England and the PDE (in Table 2). We now describe briefly the procedure we used to analyse the events in Table 1.

We used both *P*- and *SH*-waveforms and first motion polarities of *P*-waves to constrain earthquake source parameters. The approach we followed is that described by Molnar & Lyon-Caen (1989), which we also used in a study of earthquakes in the Hellenic Trench (Taymaz, Jackson & Westaway 1990). We compared the shapes and amplitudes of long-period *P*- and *SH*-waveforms recorded by WWSSN and GDSN stations in the distance range 30°–90° with synthetic waveforms. To determine source parameters we used McCaffrey & Abers's (1988) version of Nábělek's (1984) inversion procedure, which minimizes, in a weighted least-squares sense, the misfit between observed and synthetic seismograms (McCaffrey & Nábělek 1987; Nelson, McCaffrey & Molnar 1987; Fredrich, McCaffrey & Denham 1988). Seismograms are generated by combining direct (*P* or *S*) and reflected (*pP* and *sP*, or *sS*) phases from a point source embedded in a given velocity structure. Receiver structures are assumed to be homogeneous half-spaces. Amplitudes are adjusted for geometrical spreading, and for attenuation using Futterman's (1962) operator, with $t^* = 1$ s for *P* and $t^* = 4$ s for *SH*. As explained by Fredrich *et al.* (1988), uncertainties in t^* affect mainly source duration and seismic moment, rather than source orientation or centroid depth. Seismograms were weighted according to the azimuthal distribution of stations, such that stations clustered together were given smaller weights than those of isolated stations (McCaffrey & Abers 1988). The inversion routine then adjusts the strike, dip, rake, centroid depth and source time function, which is described by a series of overlapping isosceles triangles (Nábělek 1984, 1985) whose number and duration we selected.

Our experience with the inversion routine was very similar to that of Nelson *et al.* (1987), McCaffrey (1988), Fredrich *et al.* (1988) and Molnar & Lyon-Caen (1989). For all except the two largest events (numbers 5 and 6 in Table 1) we found that a point source, in which all slip occurs at the same point (the centroid) in space but not in time, was a good approximation: i.e. we saw no indication of the systematic azimuthal variations in waveforms that might be associated with rupture propagation. Waveforms from the

Table 1. Source parameters of north Aegean earthquakes obtained from body wave inversion.

No	Date (d m y)	Origin Time (h m s)	Location Lat. N(°)	Long. E(°)	m_b	M_s	M_o $\times 10^{16}$ (N m)	Centr. Depth (km)	Strike (°)	Dip (°)	Rake (°)	Slip Vec. (°)
1	18.09.1963	165812.5	40.90	29.20	5.2	6.4*	96	15±3	304±10	56±5	-82±8	034
2	06.10.1964	143123.0	40.30	28.23	5.9	6.9*	410	14±2	100±10	40±5	-90±5	010
3	09.03.1965	175754.5	39.34	23.82	5.7	6.3*	147	7±2	135±5	85±5	15+3/-7	045
4	04.03.1967	175809.0	39.25	24.60	6.0	6.5*	243	10±2	313±7	43±5	-56±6	001
5	22.07.1967	165658.0	40.67	30.69	6.0	7.1*	7500	12±2	275±3	88±4	-178±2	095
6	19.02.1968	224542.4	39.40	24.94	6.0	7.2*	3450	15±3	311±6	90±3	20±5	041
7	03.03.1969	005910.5	40.08	27.50	5.6	6.0*	50	5-1/+2	60±10	40±5	68±5	330
8	08.04.1970	135028.2	38.34	22.86	5.8	6.2*	91†	9	75	67	-94	355
9	27.03.1975	051507.9	40.45	26.12	6.0	6.6*	200	15±3	68±8	55±5	-145±8	046
10	20.06.1978	200321.5	40.78	23.24	6.1	6.4	424†	7	271	42	-74	340
11	14.06.1979	114445.1	38.79	26.57	5.9	5.8	67	8±2	262±10	41±5	-108±10	352
12	24.02.1981	205337.0	38.23	22.97	6.1	6.7*	875	12±2	264±15	42±5	-80±10	340
13	25.02.1981	023553.5	38.17	23.12	5.7	6.4*	397	8±2	241±6	44±5	-85-10/+7	324
14	04.03.1981	215807.2	38.24	23.26	5.8	6.3*	270	7±3	230±5	45±5	-90±10	320
15	19.12.1981	141051.1	39.22	25.25	6.0	7.2	2600	10±3	60±5	79±5	175±3	061
16	27.12.1981	173913.3	38.91	24.92	5.4	6.4*	382	6±1	216±8	79±5	175±5	037
17	18.01.1982	192725.0	39.96	24.39	5.8	6.9	732	7±1	233±5	62±5	187-10/+7	050
18	06.08.1983	154351.9	40.14	24.74	6.0	6.9	1940	7±1	47-5/+8	83±6	180±10	047
19	30.04.1985	181412.9	39.26	22.81	5.4	5.5	30	11±2	77±5	50±5	-105±5	010
F	30.07.1967	013102.0	40.72	30.52	5.6	—	—	—	121	50	-111	061

* After N. Ambraseys (pers. comm.).
† After Y. Liotier (1989).
F After M°Kenzie (1972).

Table 2. CMT solutions of Aegean earthquakes.

No.	Date (d m y)	Origin Time (h m s)	Location Lat. N(°)	Long. E(°)	m_b	I.S.C M_s	h (km)	M_o $\times 10^{16}$ (N m)	Centr. Depth (km)	Str. (°)	Dip (°)	Rake (°)	Slip Vec. (°)
1*	23.05.1978	233411.4	40.76	23.27	5.6	5.8	9	57.1	10	74	36	-96	351
2*	19.06.1978	103105.4	40.75	23.22	5.3	5.1	10	10.7	15	280	44	-67	339
3*	16.06.1979	184200.3	38.75	26.63	4.9	5.0	11	12.0	15	127	45	-48	345
4*	18.07.1979	131202.5	39.67	28.66	5.2	4.9	7	11.5	15	111	34	-85	014
5*	09.07.1980	021152.8	39.27	23.04	5.8	6.3	8	867.0	10	58	41	-128	014
6*	10.07.1980	193900.6	39.31	22.92	5.3	5.5	22	30.8	15	79	31	-123	026
7*	11.08.1980	091558.3	39.27	22.66	5.2	4.8	27	7.5	15	226	47	-124	—
8*	05.03.1981	065906.8	38.21	23.13	5.3	5.3	20	18.4	15	276	43	-59	—
9*	29.12.1981	080045.0	38.80	24.77	5.0	5.4	28	13.7	15	330	63	10	060
10*	05.07.1983	120127.4	40.33	27.23	5.5	5.8	7	165.0	15	254	49	-173	069
11*	26.08.1983	125209.8	40.51	23.92	4.9	4.8	3	6.4	15	72	73	-168	068
12*	10.10.1983	101658.2	40.27	25.32	4.9	5.1	4	13.5	15	71	58	-175	068
13*	21.10.1983	203449.1	40.13	29.38	5.0	4.9	12	16.4	15	217	90	-180	—
14*	11.02.1984	080250.0	38.38	22.07	5.3	5.5	19	33.1	15	77	28	-121	—
15*	06.05.1984	091201.7	38.82	25.66	5.0	5.2	12	16.3	10	243	86	-179	063
16*	17.06.1984	074802.6	38.86	25.72	5.0	4.5	3	6.2	15	156	73	-9	066
17*	09.11.1985	233042.3	41.24	23.93	5.5	5.3	18	7.5	21	256	33	-85	346
18*	25.03.1986	014134.5	38.36	25.15	5.2	5.5	4	20.0	15	168	63	-7	078
19†	19.03.1989	053702.5	38.61	23.53	5.2	5.3	10	14.0	15	230	90	180	050
20†	05.09.1989	065237.2	40.20	25.10	4.9	5.0	10	15.0	15	64	34	-159	046
A	11.04.1964	160042.8	40.50	25.00	5.1	—	33	—	—	40	90	180	040
B	29.04.1964	042106.7	39.30	23.70	5.1	—	33	—	—	225	80	-140	048
C	23.07.1949	150330.1	38.66	26.29	6.7	—	—	—	—	—	—	—	—
D	06.04.1969	034933.5	38.50	26.42	5.5	—	14	—	—	101	50	-90	011
E	20.12.1965	000815.3	40.20	24.80	5.3	5.8	33	—	—	73	40	-140	042

* After Ekström and England (1989).

† After PDE monthly listings.

A and C after M^{c}Kenzie (1972).

B After Jackson et al. (1982b).

D and E after M^{c}Kenzie (1972), Jackson and White (1989).

two largest events show evidence of multiple ruptures which we attempted to match by later subevents of a different orientation from the first: these are discussed in greater detail in Appendix A. The focal sphere was generally covered by observations in all quadrants, though with more stations to the north than the south, and we found that estimates of the strike, dip, rake and centroid depth were relatively independent of each other. Thus if one parameter was fixed at a value within a few degrees or km of its value yielded by the minimum misfit of observed and synthetic seismograms, the inversion routine usually returned values for the other parameters that were close to those of the minimum misfit solution. The strikes and dips of nodal planes were consistent, within a few degrees, with virtually all first motion polarities (Fig. 4): the few inconsistencies are documented in Appendix A, and are mostly at close stations, for which the take-off angle of the ray path leaving the source is uncertain. The estimate of seismic moment clearly depended on the duration of the source time function, and to some extent on centroid depth and velocity structure. As our main interest is in source orientation and depth, we did not concern ourselves much with uncertainties in seismic moment, which in most cases is probably about 30 per cent. We estimated the lengths of the time functions by increasing the number of isosceles triangles until the amplitudes of the later ones became insignificant. The seismogram lengths we selected for inversion were sufficient to include the reflected phases *pP*, *sP* and *sS*. We examined the *P*-waves for *PcP* arrivals, where they were anticipated within the selected window, but this phase was never of significant amplitude. *ScS* presented a greater problem, and we generally truncated our inversion window for *SH*-waves before the *ScS* arrival. Where *ScS* arrives within the window we retained, we marked its arrival time explicitly (see, for example, MAT and BAG in Fig. 5).

All the 17 events we analysed in Fig. 3 and Table 1 had centroid depths in the range 5–15 km. The source velocity structures we used to calculate the synthetic seismograms are listed in Table 3. In all cases we assumed the centroid was in a layer with *P* velocity 6.8 km s^{-1}, which is a likely lower crustal velocity (Makris & Stobbe 1984) and appropriate for calculating the take-off angles of ray paths leaving the source. We took an average *P* velocity of 6.0 km s^{-1} above the source for all cases except where the epicentres were near or within known sedimentary basins, such as those associated with the North Aegean Trough, Skyros basin or Gulf of Corinth, where lower average velocities above the source were used. These basins are known to have thick sequences of Neogene sediment (e.g. Lalechos & Savoyat 1979; Brooks & Ferentinos 1980, 1984; Le Pichon, Lybéris & Alvarez 1984; Ginzburg, Makris & Hirschleber 1987; Higgs 1988), but detailed velocity structures based on seismic refraction are unavailable. Uncertainty in the average velocity above the source leads directly to an uncertainty in centroid depth, which we estimate to be about ±2 km for the range of depths involved in this study.

2.2 Uncertainties in source parameters

Having found a set of acceptable source parameters, we followed the procedure described by McCaffrey & Nábělek

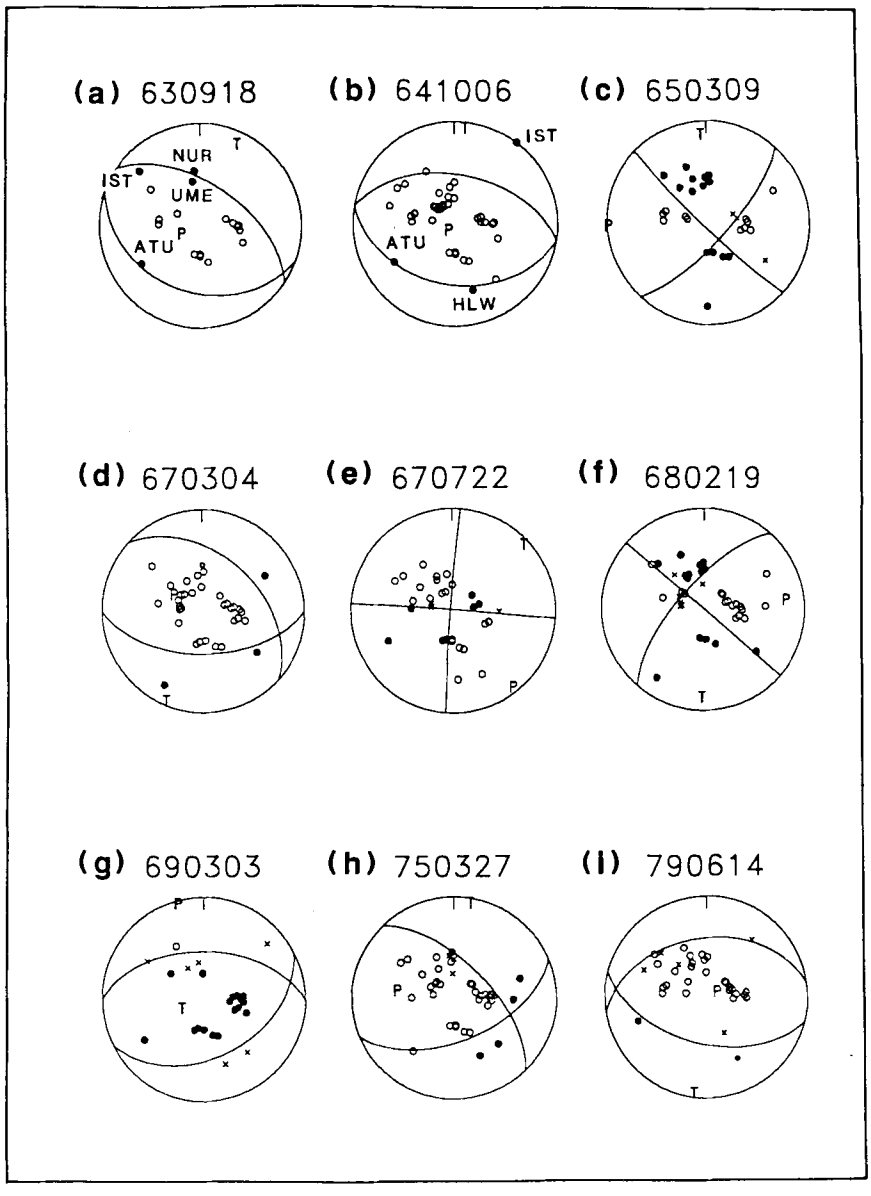

Figure 4. Lower hemisphere equal area projections of the first motion polarity data. Station positions of the focal sphere have been plotted using the same velocity below the source (6.8 km s^{-1}) that was used in our waveform inversion procedure. Filled circles are compressional first motions, open are dilatational. All were read on long-period instruments of the WWSSN. Nodal planes are those of the minimum misfit solutions. Above each sphere is the event's date (year, month, day).

(1987), Nelson *et al.* (1987), Fredrich *et al.* (1988), Molnar & Lyon-Caen (1989) and Taymaz *et al.* (1990), in which the inversion routine is used to carry out experiments to test how well individual source parameters are resolved. We investigated one parameter at a time by fixing it at a series of values either side of its value yielded by the minimum misfit solution, and allowing the other parameters to be found by the inversion routine. We then visually examined the quality of fit between observed and synthetic seismograms to see whether it had deteriorated from the minimum misfit solution. In this way we were able to estimate the uncertainty in strike, dip, rake and depth for each event. In common with the authors cited above, we believe this procedure gives a more realistic quantification of likely errors than the formal errors derived from the covariance matrix of the solution. We will now illustrate this procedure using the earthquake of 1967 March 4 (no. 4 in Table 1 and Fig. 7), near Skyros island.

The minimum misfit solution for the earthquake of 4.3.1967 is shown in Fig. 5. The nodal planes of this solution are compatible with all first motion *P* polarities, shown in Fig. 4(d). The *P* and *SH* pulses are simple at all azimuths and characteristic of normal faulting with a shallow focal depth. There is good coverage of the focal sphere at all azimuths, for both first motion and waveform data. Fig. 6 summarizes some of the tests we carried out to estimate the uncertainties in strike, dip, rake and centroid depth. The top row of waveforms compares observed *P* and *SH* seismograms (solid lines) at selected stations with synthetic seismograms (dashed) generated for the minimum misfit

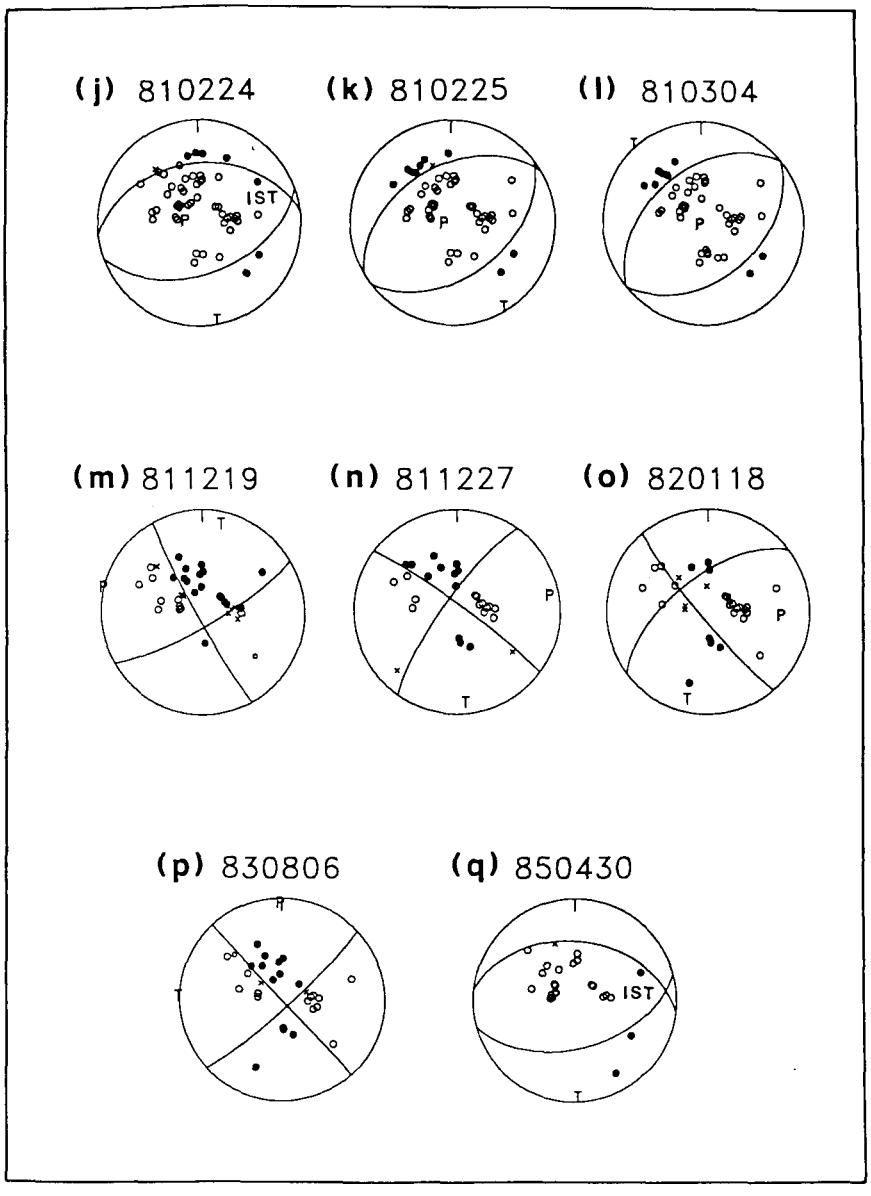

Figure 4. (*continued*)

solution. To calculate the synthetic seismograms in the second row, we fixed the centroid depth at 4 km deeper than that found by the minimum misfit solution and allowed all the other parameters to change in the inversion. The fit of observed to synthetic seismograms is noticeably worse at the stations marked by a vertical bar, as the pulse width widens with increasing depth. Note that the fit at one station (the SH wave at WIN, marked by a star) has improved: it is quite common for the fit at one or two stations to improve slightly when a parameter is set to a value that is clearly unacceptable because of a poor fit at many other stations (see also Molnar & Lyon-Caen 1989). We found that changing the depth of this earthquake by more than 2 km produced a noticeable degradation in the fit of waveforms, and take this to be a realistic estimate of the uncertainty in focal depth. This estimate, which is listed in Table 1, does not include the uncertainty related to the unknown average velocity above the source, discussed above. Row three illustrates a similar test for uncertainty in strike, which was fixed at 10° more than that of the minimum misfit solution. The match of seismograms is noticeably worse, particularly for *SH* at WIN and WES. In row four the dip has been fixed at a value 8° less than that in row one: this degrades the fit

Table 3. Source velocity structures used in waveform inversion.

Velocity Structures	V_p (kms^{-1})	V_s (kms^{-1})	Density (kgm^{-3})	Thickness (km)	Events
A	6.00	3.45	2780	10	1, 2, 5
	6.80	3.92	2910	half-space	
B	5.80	3.31	2710	5	3(1.0), 4(0.3), 6(0.3),
	6.80	3.92	2910	half-space	9(0.3), 11(0.2), 15(0.2) 16(0.3), 17(1.0), 18(0.5)
C	6.00	3.45	2780	4	7
	6.80	3.92	2910	half-space	
D	4.50	2.59	2400	1	12(0.9), 13(0.8)
	6.80	3.92	2910	half-space	
E	6.00	3.45	2780	6	14
	6.80	3.92	2910	half-space	
F	6.00	3.45	2780	8	19
	6.80	3.92	2910	half-space	

Water depths (where appropriate) are shown in km in brackets after the event numbers.

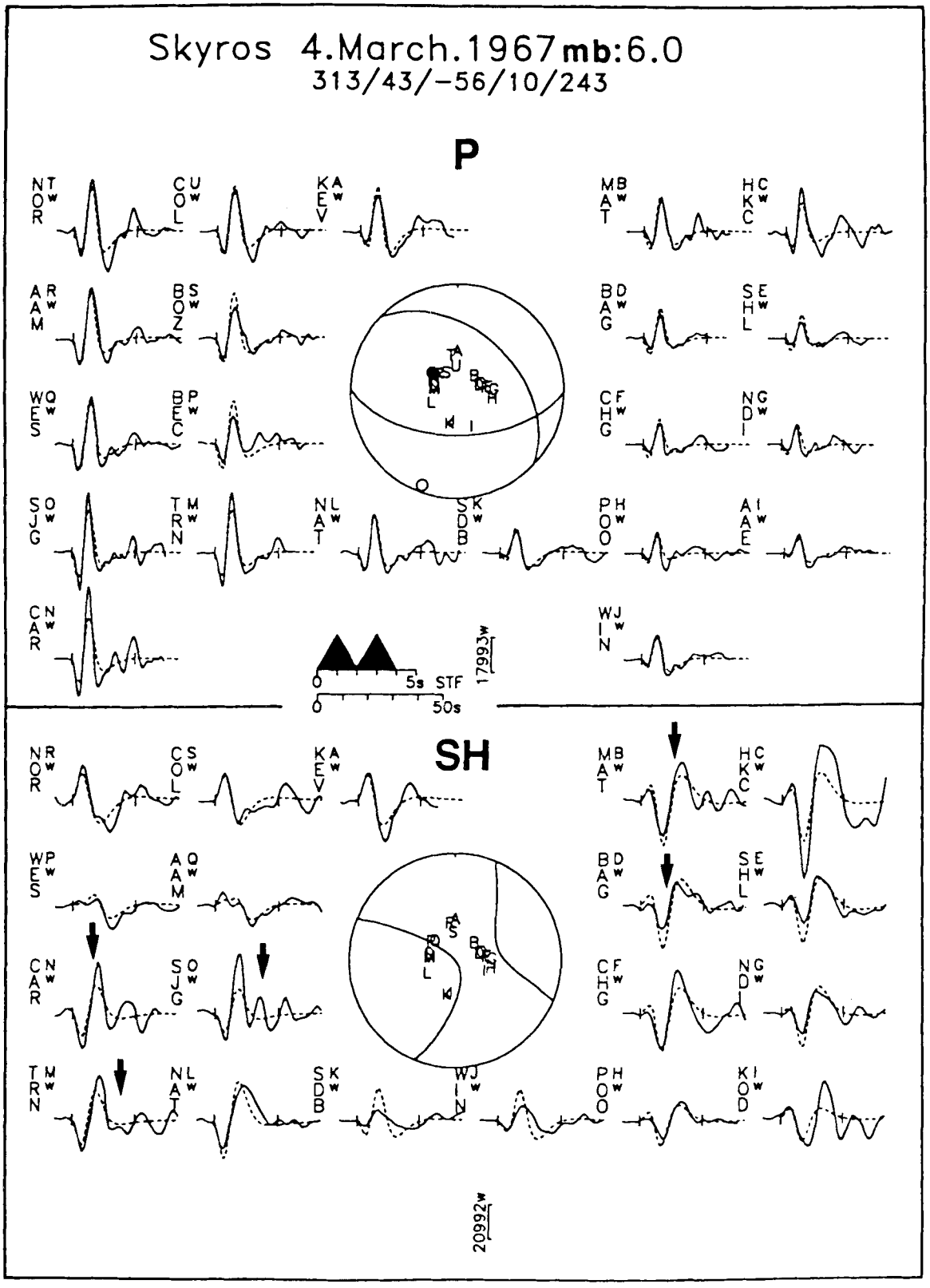

Figure 5. This (and subsequent similar figures in Appendices A and B) shows the radiation patterns and synthetic waveforms for the minimum misfit solution returned by the inversion procedure, as well as the observed waveforms. For the purposes of display, waveform amplitudes have been normalized to that of an instrument with a gain of 3000 at a distance of 40°. Solid lines are observed waveforms, and the inversion window is identified by vertical bars. Synthetic waveforms are dashed lines. The station code is identified to the left of each waveform, together with an upper case letter, which identifies its position on the focal sphere, and a lower case letter that indicates the type of instrument (w = WWSSN long period; d = GDSN long period). The vertical bar beneath the focal sphere shows the scale in μm, with the lower case letter indicating the instrument type, as before. The source time function is shown in the middle of the figure, and beneath it is the time-scale used for the waveforms. Focal spheres are shown with *P* and *SH* nodal planes, in lower hemisphere projection. Station positions are indicated by letter, and are arranged alphabetically clockwise, starting from north. P and T axes are marked by solid and open circles. Where *ScS* is expected to arrive within the inversion window its predicted arrival time is marked with a black arrow (e.g. for MAT in this figure). Beneath the header at the top of the figure, which shows the date and body wave magnitude, are five numbers which show the strike, dip, rake, centroid depth and seismic moment (in units of 10^{16} N m) of the minimum misfit solution.

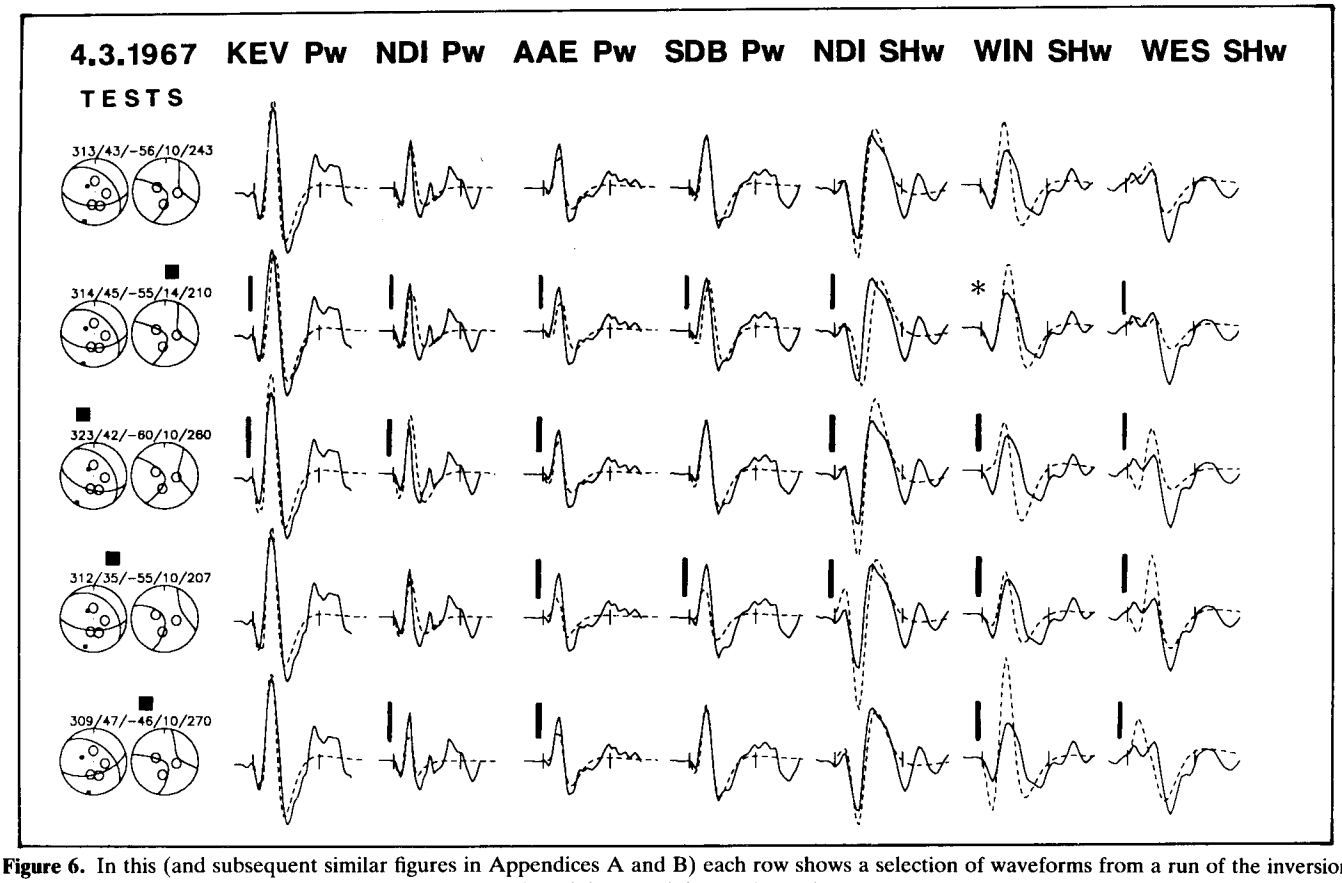

Figure 6. In this (and subsequent similar figures in Appendices A and B) each row shows a selection of waveforms from a run of the inversion program. The top row always shows waveforms from the minimum misfit solution. The stations are identified at the top of each column, with the type of waveform marked by *P* or *SH* and followed by the instrument type, as in Fig. 5. At the start of each row are the *P* and *SH* focal spheres for the focal parameters represented by the five numbers (strike, dip, rake, depth and moment, as in Fig. 5), showing the positions on the focal spheres of the stations chosen. A filled square above one of the focal parameters means that it was held fixed in that inversion: thus in rows 2, 3, 4 and 5 the depth, strike, dip and rake were held fixed, respectively. The displayed waveforms are in the same convention as in Fig. 5, but in this type of figure the large bars show matches of observed to synthetic waveforms that are worse than in the minimum misfit solution, and asterisks show matches that are improvements.

of seismograms, particularly for *SH*. Finally, in row five the rake has been fixed at a value 10° less than that in row one. Here, too, the degradation of the fit is clear, particularly for *SH*. In each of rows 2 to 5 one parameter has been perturbed from the minimum misfit solution and then fixed: yet the values returned by the inversion routine for the other parameters have not shifted significantly from those of the minimum misfit solution. This gives us some confidence that there is not significant trade-off between source parameters for this event. The greatest change occurs to the value of seismic moment, which varies by 20 per cent.

We carried out many experiments of the sort illustrated in Fig. 6, and, based on these, estimate the source parameters and uncertainties of the 1967 March 4 Skyros earthquake to be: strike $313 \pm 7°$; dip $43 \pm 5°$; rake $-56 \pm 6°$, and depth 10 ± 2 km (though this does not include uncertainty related to velocity structure). Other earthquakes are discussed in Appendix A. For all of them we carried out similar tests to those described above. Their source parameters, and our estimates of their uncertainties, are summarized in Table 1.

2.3 The pattern of focal mechanisms

The 17 focal mechanisms we determined, and the two determined by Liotier using the same inversion algorithm and procedure, are shown in Fig. 7. West of 30°E they nearly all have approximately N–S T axes, reflecting the dominance of N–S extension in the Aegean (see Jackson & McKenzie 1988a). Two types of mechanism are common: normal faulting with roughly E–W nodal planes and strike–slip faulting with nodal planes trending NE–SW and NW–SE. Most of the strike–slip solutions are in the offshore regions of the north and central Aegean Sea, whereas most of the normal faulting solutions are on the surrounding land or coast. The one obvious anomaly is the high-angle reverse faulting solution of 1969 March 3 (no. 7 in Fig. 7 and Table 1) in NW Turkey, which shows shortening in a roughly N–S direction. Our solution for this event is well constrained by first motion polarities (Fig. 4g) and waveforms (Fig. A6, Appendix A), and is similar to that given by McKenzie (1972), which was based on first motions alone. This earthquake was almost the smallest event we were able to study (Table 1), with a moment of 5×10^{17} N m. It occurred close to a restraining bend in the ENE–WSW striking right-lateral strike–slip fault that moved in the much larger 1953 Yenice–Gönen earthquake (Ketin & Roesli 1954; Barka & Kadinsky-Cade 1988), which had a moment of about 10^{20} N m (Jackson & McKenzie 1988a). The faulting in this anomalous earthquake could be related to the local geometry of the main strike–slip system,

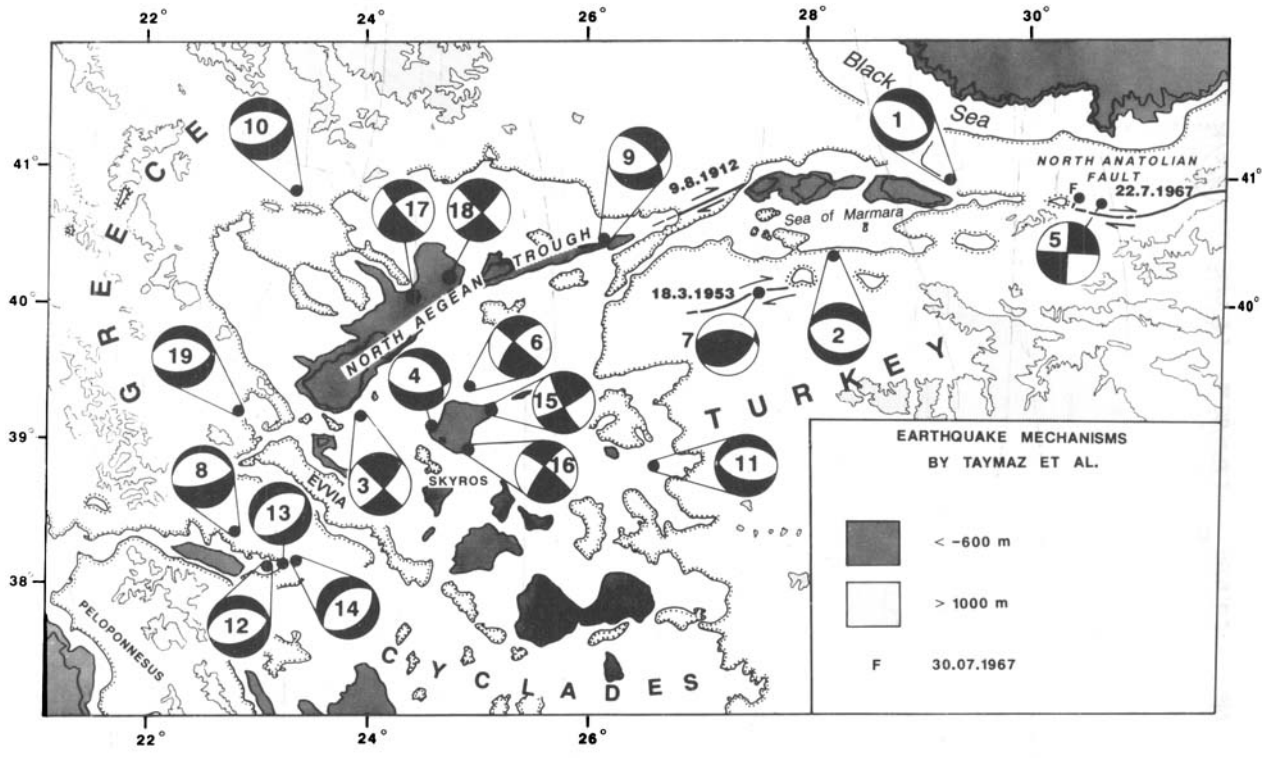

Figure 7. Lower hemisphere projections of the focal mechanisms corresponding to the minimum misfit solutions of the earthquakes studied by us and by Liotier (1989). Compressional quadrants are shaded. Numbers identify the events in Table 1. Also shown are the faults that moved in the 1912, 1953 and 1967 earthquakes in NW Turkey, and the epicentre of the large aftershock of the 1967 Mudurnu earthquake, marked F.

and may not be a reliable guide to the regional strain field in western Turkey. It is common for small earthquakes, particularly aftershocks, to have mechanisms incompatible with a uniform regional strain field (e.g. Richens *et al.* 1987; Lyon-Caen *et al.* 1989; Mercier & Carey-Gailhardis 1989), but unusual to see this effect with earthquakes large enough to study teleseismically. We return to this earthquake in the later discussion of kinematics.

We can now compare the pattern obtained by us and by Liotier (1989) with the CMT solutions reported by Ekström & England (1989) and the PDE, which are shown in Fig. 8 and Table 2. The patterns are essentially the same. Fig. 8 also shows mechanisms with T axes approximately N–S, with most strike–slip solutions in the offshore regions of the north and central Aegean Sea, and most normal faulting solutions on the surrounding land or coast. Fig. 8 contains mechanisms for 17 earthquakes that have smaller seismic moments than the reverse faulting event 1969 March 3 (no. 7 in Fig. 7), yet none of these stands out as anomalous in the same way. The main difference between the population of events in Fig. 7 and those in Fig. 8 is size: those in Fig. 8 are generally much smaller, with only three events (1*, 5*, 10*) having moments of comparable size to those in Fig. 7 (see Tables 1 and 2). The similarity between the patterns in Figs 7 and 8 gives us some confidence that the CMT solutions for the smaller events in Fig. 8 are essentially correct, even though we cannot confirm them individually by our inversion procedure.

We will therefore make cautious use of them in the following discussion of the tectonics. Note that, when we refer to events by their numbers in Tables 1 and 2 and Figs 7 and 8, an asterisk after the number means the solution is a CMT inversion (i.e. in Fig. 8 and Table 2). Numbers without asterisks refer to solutions by ourselves and by Liotier (1989), in Fig. 7 and Table 1.

3 ACTIVE FAULTING

In this section we review the principal characteristics of the active faulting around the north and central Aegean, using the new earthquake data, as well as geophysical and field-based observations. This information is summarized in Fig. 9(a). Fig. 9(b) shows the geographical locations discussed in the text.

3.1 Northwest Turkey and the Sea of Marmara

The westernmost of the large ($Ms > 7.0$) earthquakes of 1939–1967 that ruptured almost the entire length of the North Anatolian Fault between 31°E and 41°E was the Mudurnu earthquake of 1967 July 22 (no. 5, Fig. 7). This earthquake produced about 80 km of surface faulting, with up to 2 m of right-lateral strike–slip offset (Ambraseys & Zatopek 1969). Its waveforms suggest that it was a multiple event (Fig. A4 in Appendix A, and Stewart & Kanamori 1982), with the mechanism of the early part of the rupture well-constrained to a strike–slip solution, compatible with the surface faulting. It was followed by an aftershock (on 1967 July 30: marked F in Fig. 7) at the western end of the surface faulting, whose waveforms were too small to model teleseismically, but whose first motions polarities are sufficient to demonstrate normal faulting with a roughly NNW strike (McKenzie 1972; Jackson & White 1989). West of the 1967 Mudurnu surface ruptures, the North Anatolian

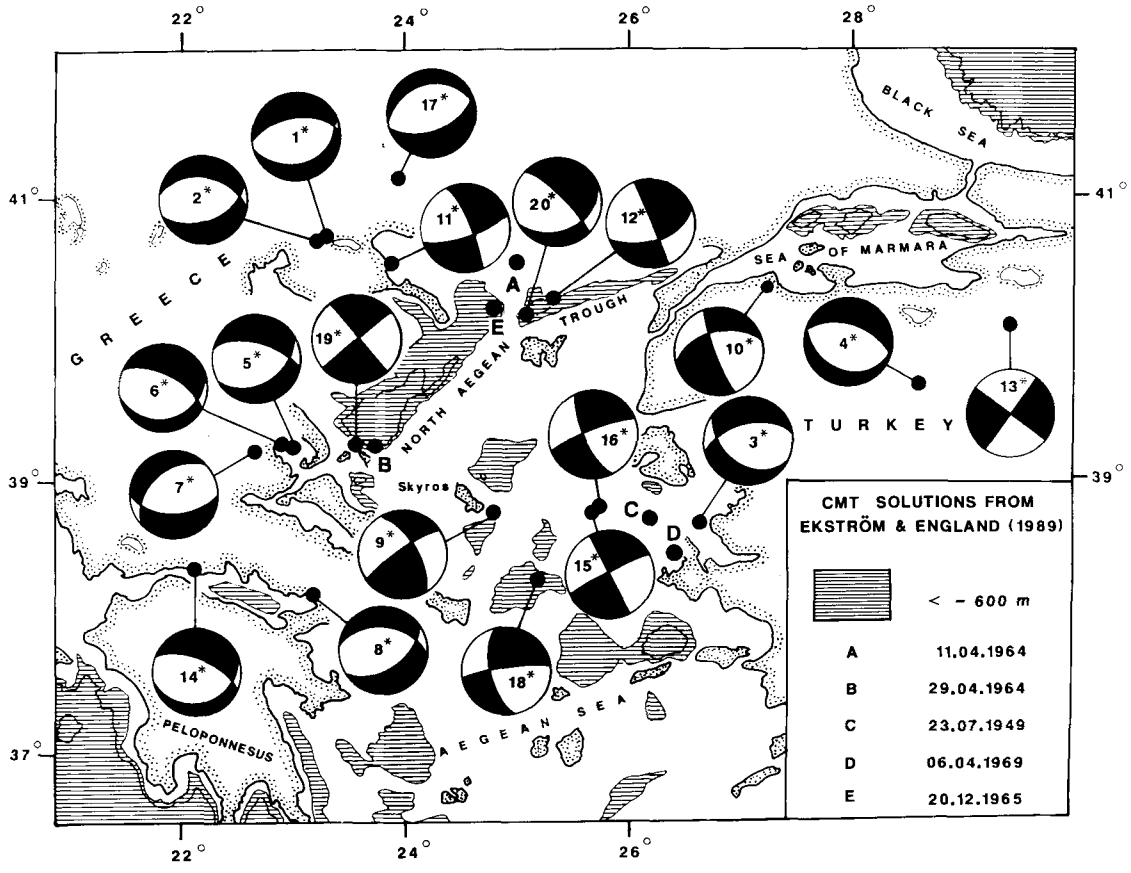

Figure 8. Focal mechanisms corresponding to the best double couple solutions of the CMT inversions reported by Ekström & England (1989) or the USGS PDE. Numbers identify the events in Table 2. The epicentres of a number of events that were too small for body waveform analysis using our procedure, but which were large enough to obtain first motion solutions using long-period WWSSN instruments, are marked A to E (see inset).

Fault system bifurcates (Fig. 9a), losing its simple appearance, and enters a region of distributed strike–slip and normal faulting that characterizes the whole of the north and central Aegean Sea, the Sea of Marmara and NW Turkey (McKenzie 1978; Dewey & Şengör 1979; Lybéris 1984; Crampin & Evans 1986; Barka & Kadinsky-Cade 1988). Fig. 7 shows two normal faulting solutions in NW Turkey: for the Çınarcık earthquake of 1963 September 18 (No. 1), and for the Manyas earthquake of 1964 October 6 (No. 2), which produced surface faulting along a north-dipping normal fault between the two lakes south of the Sea of Marmara (Ketin 1966; Öcal, Uçar & Taner 1968). Other normal faults with an approximately E–W strike are known from this region. Normal faults dipping both north and south bound the deep basins in the Sea of Marmara: their presence is clear from tilting seen on seismic reflection records (Turkish Petroleum, unpublished data, and Taymaz *et al.*, in preparation) and they are responsible for uplifted islands (such as Marmara, Îmralı and the Princes islands) and coastal regions (such as Ganoşdağ) in their footwalls. Another normal fault, which Barka & Kadinsky-Cade (1988) suggest may have been responsible for an earthquake in 1855, is clear from the morphology of the escarpment south of Bursa.

Two parallel strands of right-lateral strike–slip faulting with an E–W strike enter the eastern end of the Sea of Marmara (Dewey & Şengör 1979; Barka & Kadinsky-Cade 1988). Farther west, the strike–slip faulting has a more ENE strike. Two events are known to have produced surface ruptures involving right-lateral strike–slip on such faults: the 1912 Saros earthquake (Ambraseys & Finkel 1987) and the 1953 Yenice–Gönen earthquake (Ketin & Roesli 1954), shown in Fig. 7. McKenzie (1972) gives a first motion fault plane solution for the 1953 event that is consistent with observations of Ketin & Roesli (1954), but is not well constrained. A fault parallel to, and 20 km NW of, the one responsible for the 1953 earthquake is clear on satellite images (McKenzie 1978; Lybéris 1984). Between the 1912 and 1953 earthquake faults the dominant drainage pattern, and the Dardanelles itself, has a similar ENE trend, suggesting that other, less obvious, strike–slip faults may also be present. One such fault may have been responsible for the 1983 July 5 Biga earthquake (No. 10* in Fig. 8).

Thus NW Turkey and the Sea of Marmara are dominated by normal faulting with an E–W strike and right-lateral strike–slip faulting with an ENE strike. The reverse faulting in the earthquake of 1969 March 3 (No. 7 in Fig. 7), which we discussed earlier, is clearly anomalous, and stands out from the pattern revealed by the larger earthquakes and the geomorphology.

3.2 The north and central Aegean Sea

The most dramatic bathymetric feature of the north Aegean Sea is the North Aegean Trough (Figs 7 and 8), which consists of a series of deep fault-bounded basins (Lybéris

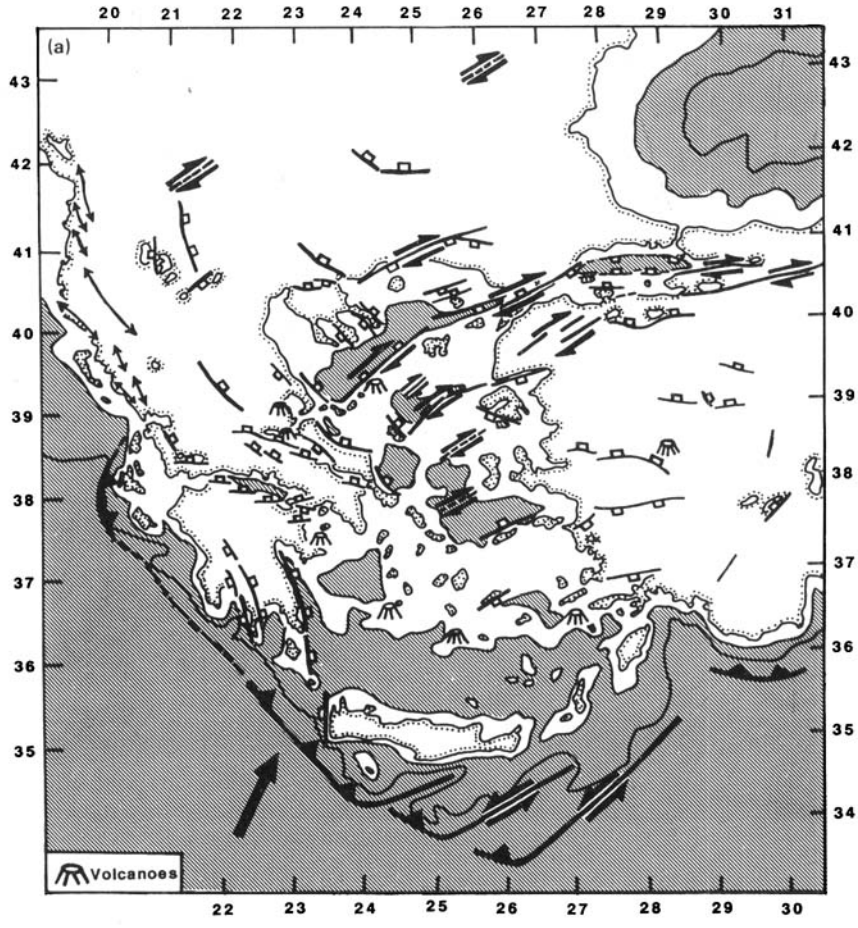

Figure 9. (a) Summary sketch of the faulting and bathymetry in the Aegean region, compiled from our observations and those of Lyberis (1984), Le Pichon *et al.* (1984), Şaroğlu, Emre & Boray (1987) and Mercier *et al.* (1989). Normal faults are shown with open blocks on the downthrown side: many of these in the central Aegean have large strike–slip components, which are shown by heavy black arrows. Most of the normal faults are not as continuous as they are shown here, but are typically segmented on a scale of 15–20 km (see Roberts & Jackson 1991). This map shows only faults that are large, and are clearly associated with major topographic and bathymetric features or with earthquakes. Many smaller faults, including several in central Greece that are antithetic to the major graben-controlling fault systems, and some in western Turkey that have an approximately N–S strike (see Şengör *et al.* 1985) have been omitted. Strike–slip faults that are shown dashed have been identified on the basis of focal mechanisms alone. Double-headed arrows in NW Greece and Albania are the axes of major anticlines visible on satellite images. The Hellenic trench is marked as a thrust with filled triangles on the hanging wall. The large black arrow in the SW is the direction of convergence in the Hellenic Trench near SW Crete (from Taymaz *et al.* 1990). Bathymetric contours are at 500 and 2000 m, and shaded below 500 m. (b) Geographic locations of places mentioned in the text.

1984; Le Pichon *et al.* 1984). Those in the west have a NE trend, while those in the eastern part of the system trend ENE. The easternmost basin, the Saros trough, is also the narrowest: in its western part, south of Samothraki, the bathymetry and gravity suggest it is a half-graben bounded by a large normal fault system along its northern margin (Le Pichon *et al.* 1984). Such faulting was probably responsible for the earthquake of 1975 March 27 (No. 9 in Fig. 7), whose mechanism is consistent with right-lateral and normal slip on a fault dipping south. Similar mechanisms are seen for two other, much smaller, earthquakes in the Saros trough (Nos 12* and 20*, Fig. 8). The fault that crosses the Gallipoli peninsula, and which was responsible for the 1912 earthquake, is a continuation of the ENE trend of the Saros trough. Surface ruptures in 1912 also showed a combination of right-lateral and normal slip, which is reflected in the topography (Ambraseys & Finkel 1987). Thus the faulting associated with the Saros trough is a semi-continuous feature from about 25°E to the western basin of the Sea of Marmara (Fig. 7) at about 27.5°E, though the asymmetry, and presumably the polarity of the normal faulting, change along strike: with the faults dipping SE in the western part of the trough (Le Pichon *et al.* 1984), NW along the north shore of the Gallipoli peninsula, and SE along Ganoşdağ, bounding the NW side of the deep offshore basin in the western Sea of Marmara. Such a change in the polarity of tilting and faulting along the strike of a basin occurs also in the North Gulf of Evvia in central Greece (Roberts & Jackson 1991), and is a common feature of extensional graben (e.g. Rosendahl *et al.* 1986).

Between the island of Samothraki and the mainland is another ENE-trending graben (Fig. 9a), parallel to the Saros trough, but now filled with Plio-Pleistocene sediments (Biju-Duval, Letouzey & Sancho 1972; Lybéris 1984). It may continue eastwards into a Neogene basin on land in eastern Thrace (Burke & Uğurtaş 1974; Mercier *et al.* 1991).

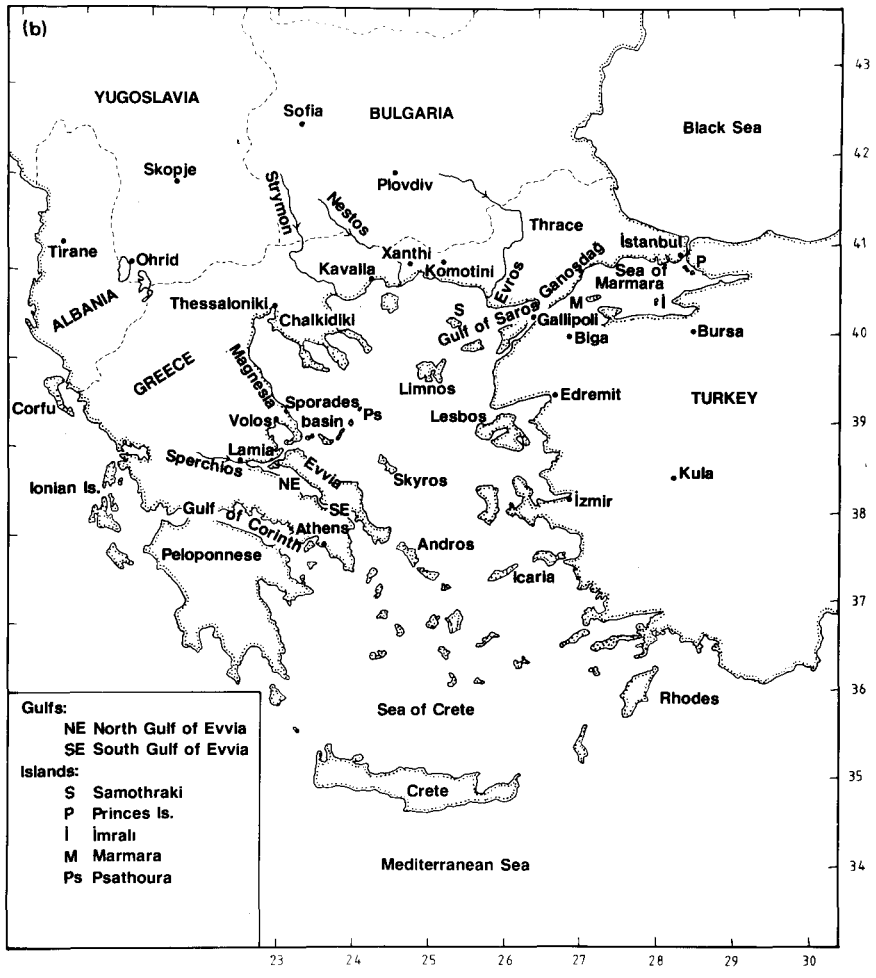

Figure 9. (*continued*)

The faults bounding these basins are thought to be active (Mercier *et al.* 1991): the lack of bathymetric expression offshore is probably related to the great volume of sediment that is washed into this area by the Evros and Nestos rivers. McKenzie (1972) gives a first motion solution for an earthquake (on 1964 November 4, marked A in Fig. 8) that is located in this region: the first motions are consistent with right-lateral slip on a NE–SW trending fault, but the mechanism is not well constrained. Eastern Thrace has been the site of many historically damaging earthquakes (N. N. Ambraseys, personal communication).

The western basin of the North Aegean Trough system lies north of the Sporades islands and south of the Chalkidhiki peninsulas. Its bathymetry is dominated by faults trending NW–SE, such as those bounding the eastern of the three Chalkidhiki peninsulas, and NE–SW (Brooks & Ferentinos 1980; Lybéris 1984; Le Pichon *et al.* 1984). The subsidence history of the basin is not known in detail because of uncertainty in dating the sediments penetrated by boreholes: but subsidence had certainly begun by middle to late Miocene time (Lybéris 1984; Kojumdgieva 1987). Lalechos & Savoyat (1979) report evaporites from the late Miocene in basins to the east of Chalkidhiki, though they are apparently absent in the basins to the south and west. Alkali basaltic volcanism 0.5 Myr old is known on the island of Psathoura, on the SE flank of the Sporades basin, apparently similar in composition to the young basalts at Volos (Fig. 2) in eastern Greece and at Kula in western Turkey (Innocenti *et al.* 1979; 1982). The Sporades basin is asymmetric.

Its bathymetry is dominated by steep scarps dipping NE along the mainland coast and dipping NW along the SE margin of the basin: slopes in the northwest part of the basin dip gently SE (Brooks & Ferentinos 1980; Lybéris 1984). The basin is clearly extensional in origin, with probable displacements of several km on its bounding faults: the precise amount of extension is controversial, because of different interpretations of gravity, heatflow and magnetic data (Le Pichon *et al.* 1984; Brooks & Kiriakidis 1986, 1987; Le Pichon, Lybéris & Alvarez 1987).

Fault plane solutions in the western part of the North Aegean Trough show mainly strike–slip faulting, consistent with right-lateral slip on NE–SW striking faults (Nos 3, 17, 18 in Fig. 7, and 19* in Fig. 8). The aftershock zones of two of these earthquakes (Nos 17 and 18 in Fig. 7) are elongated NE–SW suggesting that the nodal planes with this strike were the fault planes (Figs. 10b and 10c). The lack of normal faulting solutions is perhaps surprising, and may simply reflect the short time period over which high-quality data are available. McKenzie (1972) gave one first motion solution showing normal faulting with a NW strike (on 1965 December 12, located at E in Fig. 8). However, he plotted

the station positions on the focal sphere using a mantle velocity at the source: when replotted with a crustal source velocity, a large oblique component is required (Jackson & White 1989). A first motion solution is also available for an event on 1964 April 29 (marked B in Fig. 8): this has a well-constrained vertical nodal plane striking NE (Jackson *et al.* 1982b), but the other nodal plane is controlled only by the first motion polarity at Athens, which is too close for its position on the focal sphere to be certain.

South of the North Aegean Trough is the Skyros basin (Fig. 9). The bathymetry of this basin is asymmetric, with the deepest water and steepest escarpment along its SW margin, offshore from the island of Skyros. This escarpment is presumably a normal fault, which may have been responsible for the earthquake of 1967 March 4 (No. 4 in Fig. 7). The island of Skyros appears to be the tilted, emergent crest of the footwall block of this fault (Roberts & Jackson 1991). Like the North Aegean Trough, the Skyros basin is also the site of strike–slip faulting, with mechanisms 6, 15 and 16 in Fig. 7 and 9* in Fig. 8 consistent with right-lateral slip on NE to ENE trending nodal planes. The aftershock zone following the earthquakes of 19 and 1981 December 27 (Nos 15 and 16 in Fig. 7) is elongated NE (Fig. 10a) suggesting that the NE-striking nodal planes were the fault planes. The NE end of the Skyros basin is connected to the straight coastline trending ENE on mainland Turkey by narrow deep basins also elongated ENE (Figs 11 and 12). The right-lateral slip on the easternmost of the mechanisms in the Skyros basin (No. 15 in Fig. 7) occurs on a nodal plane with a strike almost parallel with this ENE bathymetric trend, and significantly different from the NE strike in mechanisms 6 and 16. Thus, in going from Skyros to the Turkish mainland there is evidence for the same change of faulting and bathymetric trend (NE changing to ENE) that is seen in going from west to east along the North Aegean Trough system.

Active faulting in the north and central Aegean Sea is not confined to the North Aegean Trough and Skyros basin systems, though the NE strike of the strike–slip faulting in these two places is the most obvious trend in the seismicity map (Fig. 1). The rugged emergent coastline of NE Evvia suggests that the deep basin offshore is bounded by a normal fault dipping NE (Roberts & Jackson 1991). The morphology of Icaria, and seismic reflection data offshore (Zachos 1977) suggest that the southern margin of the basin north of Icaria is bounded by a north-dipping normal fault. Fig. 8 shows three strike–slip fault plane solutions SE of the Skyros basin (Nos 15*, 16*, 18*), all of them consistent with right-lateral motion on NE to ENE striking faults. A normal fault probably bounds the SW coast of Lesbos and the deep basin offshore: the mechanism of 1979 June 14 (No. 11 in Fig. 7) is consistent with motion on such a fault, and is similar to that of 1979 June 16 (No. 3* in Fig. 8) in the same region. McKenzie (1972) gives two first motion solutions from this coastal region of western Turkey: that of 1949 July 23 (marked C in Fig. 8) is old and of poor quality; that of 1969 April 6 (marked D in Fig. 8) was replotted with a crustal source velocity by Jackson & White (1989) and requires a substantial component of normal faulting, though its strike is not well constrained. Normal faulting with a similar orientation to that in mechanisms 11 and 3* dominates the tectonics farther east in central western Turkey (McKenzie 1978; Eyidoğan & Jackson 1985; Şengör *et al.* 1985).

In summary, the focal mechanisms in Figs 7 and 8 give the impression that the north and central Aegean Sea is dominated by distributed strike–slip faulting: most of it right-lateral with a NE to ENE strike. Normal faulting must, however, be present: strike–slip faulting alone cannot produce the deep basins, and normal faults are obvious in the bathymetry and limited seismic reflection data. Several of the islands appear to be the uplifted footwall crests of such normal faults, and are adjacent to deep basins offshore (Jackson *et al.* 1982b). It may be because high-quality data are limited to the last 25 years that only two large normal faulting events are known: both of these (Nos 9 and 4 in Fig. 7) had significant and well-resolved oblique-slip components. We return to this question in the later discussion on kinematics.

3.3 Northern Greece and Thrace

The four available mechanisms from northern Greece (No. 10 in Fig. 7, and Nos 1*, 2* and 17* in Fig. 8) all show normal faulting with an E–W strike. The Thessaloniki sequence of 1978 occurred on faults dipping north (Soufleris & Stewart 1981; Soufleris *et al.* 1982) and was associated with surface faulting (Mercier *et al.* 1979a, 1983). However, the most dramatic structure in northern Greece is the Kavalla–Xanthi fault, farther east (Fig. 9a). This is a large and obvious SE-dipping escarpment, clearly visible in the morphology and satellite images, and with a vertical offset estimated by Lybéris (1984) to be about 7 km. It is sub-parallel to the North Aegean Trough system, with which it has several characteristics in common. As well as the substantial vertical offset, the youngest striations on fault surfaces show right-lateral and normal oblique slip (Lybéris 1984; Mercier *et al.* 1989). At its southwest end it terminates in a large normal fault with a NW–SE strike, bounding the Strymon valley: similar to the way the North Aegean Trough terminates in the fault along coastal Magnesia. In its eastern part it is associated with a normal fault striking E–W. On land, there have been no recent earthquakes on the Strymon–Kavalla–Xanthi system large enough for focal mechanisms to be determined. The rather small event of 1983 August 26 (No. 11* in Fig. 8) is consistent with right-lateral slip at the SW (offshore) end of the Kavalla–Xanthi fault. The epicentres of many damaging historical earthquakes can be located in the Kavala–Xanthi–Komotini region (N. N. Ambraseys, personal communication).

3.4 Central Greece

Central Greece is dominated by normal faulting, as is clear from both the geological structure and morphology (Roberts & Jackson 1991) and the focal mechanisms in Figs 7 and 8. Several large graben with a NW–SE strike, such as the Gulf of Corinth and North and South Gulfs of Evvia, are bounded by segmented faulting with a more WNW–ESE strike, which sometimes changes polarity, leading to reversals in the direction of tilting. The drainage in central Greece is controlled by such fault segmentation and variations in footwall lithology (Roberts & Jackson 1991).

Faulting on land was observed dipping north after the 1894 earthquakes along the North Gulf of Evvia (Ambraseys & Jackson 1990); dipping south after the 1980 Volos sequence (Nos 5*, 6*, 7* in Fig. 8; Papazachos *et al.* 1983); and dipping both north and south after the 1981 Gulf of Corinth sequence (Nos 12, 13, 14 in Fig. 7; Jackson *et al.* 1982a; see also Appendix B). There is no sign of right-lateral strike–slip faulting with a NE–SW strike crossing central Greece to link the North Aegean Trough with the Hellenic Trench (McKenzie 1978; McKenzie & Jackson 1983).

4 SLIP VECTORS

Figures 11 and 12 show the directions of the horizontal projections of the slip vectors in the earthquakes in Figs 7 and 8. To compile Figs 11 and 12 we have had to identify the fault plane from the two possible nodal planes in each fault plane solution. We made our choices in the following ways.

Some of the earthquakes were associated with surface faulting, and the choice of nodal plane was thus straightforward. These events were numbers 5 (Ambraseys & Zatopek 1969); 2 (Ketin 1966); 12, 13, 14 (Jackson *et al.* 1982a and Appendix B); 10, 1*, 2* (Mercier *et al.* 1979a, 1983; Soufleris *et al.* 1982); 5*, 6*, and 19 (Papazachos *et al.* 1983).

Some of the offshore events occurred in or adjacent to basins whose clear asymmetry suggests the polarity of the faulting and hence which nodal plane is likely to be the fault plane. Thus the asymmetry of the Saros trough basin (Le Pichon *et al.* 1984) and the proximity of known right-lateral slip in the 1912 Saros earthquake on land (Ambraseys & Finkel 1987), suggest that the SE-dipping nodal plane is the fault plane in events 9, 12* and 20*. It is reasonable to assume that event 4 occurred on the large NE-dipping fault that bounds the Skyros basin. We have assumed that the fault plane dips south in the 1963 Çınarcık earthquake (No. 1), which is consistent with the dip of the known fault along the north side of the eastern deep basin in the Sea of Marmara that is presumably responsible for uplifting the Princes' Islands in its footwall. We have assumed a south-dipping fault for event 11 because it is close to the fault bounding the basin on the south side of Lesbos, and we have assumed the same polarity for the fault in event 3*, because of its proximity to event 11.

The NE elongation of the aftershock zones of events 15, 16, 17 and 18 (Fig. 10) suggest that the NE-striking nodal planes are the fault planes in these events. Since NE-trending right-lateral strike–slip faulting is so prevalent in the central Aegean, we have chosen the NE-trending nodal plane as the fault plane in events 3, 6, 9*, 11*, 15*, 16*, 18* and 19*.

The choice of nodal plane in events 7, 8, 4*, 17* is unimportant, because they are so nearly pure dip–slip. Our choice of fault plane in event 8* is based on the similarity of the NE-dipping slip vector with those in the nearby events 8, 12, 13, and 14. The choice for event 10* is based on the known ENE-trending right-lateral strike–slip faulting that crosses the Biga peninsula, such as that responsible for the 1953 Yenice–Gönen earthquake (Ketin & Roesli 1954). For events 7*, 8*, 13* and 14* we had no reason to choose either nodal plane as the fault plane, so we have omitted

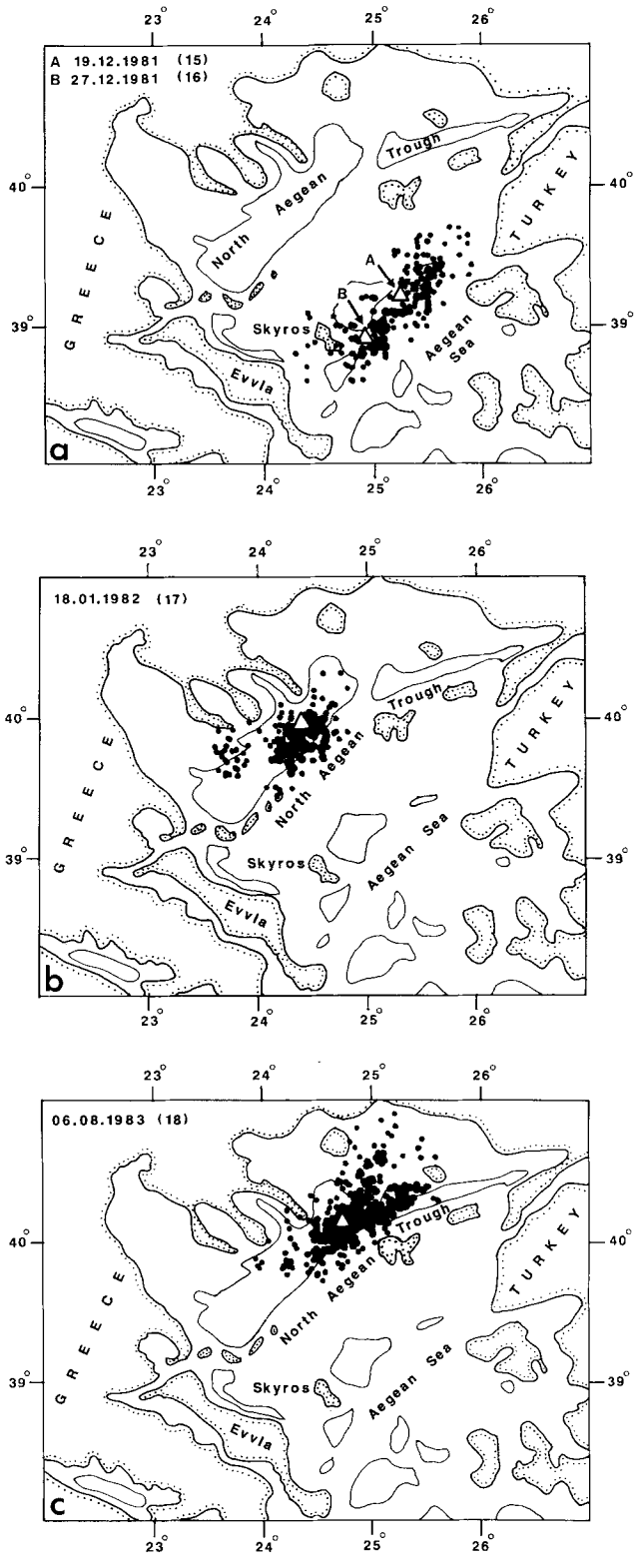

Figure 10. ISC locations of aftershocks following large earthquakes in the central Aegean. In each case the aftershocks are plotted for one month after the main shock.

their slip vectors from Figs 7 and 8. The slip vector in the anomolous reverse faulting event (No. 7) in NW Turkey is shown by convergent black arrows in Fig. 7.

The slip vectors we chose are included in Tables 1 and 2.

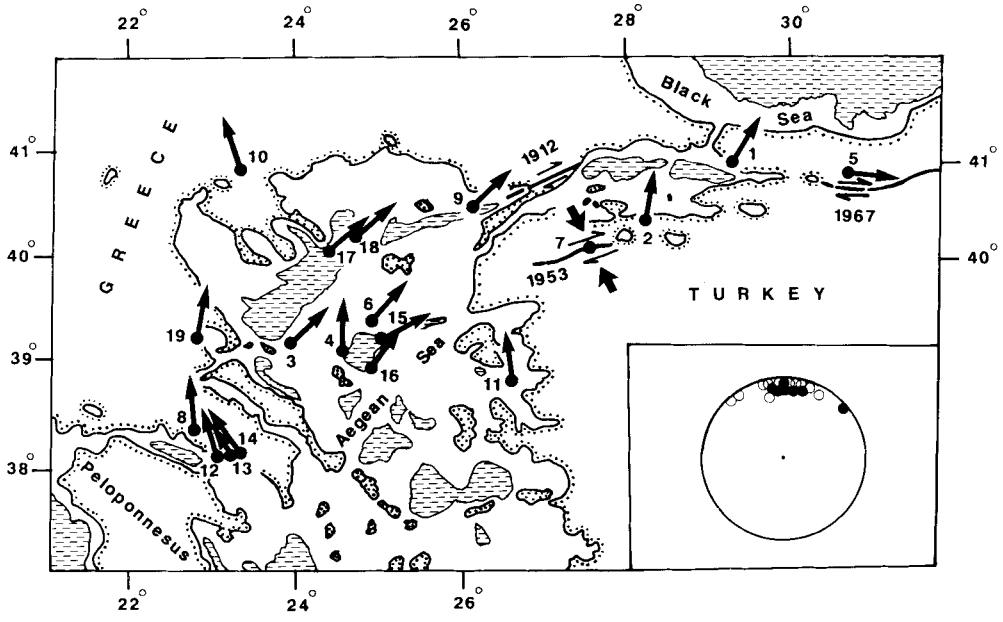

Figure 11. Horizontal projections of the slip vectors for the focal mechanisms obtained by our inversion procedure. Numbers identify the events in Fig. 7 and Table 1. Arrows show the direction of motion of the north side relative to the south. Bathymetry is shaded below 600 m. The inset shows the lower hemisphere projection of the T axes for these events: open circles are the normal faulting mechanisms, filled circles are the strike–slip. The slip vector in the anomolous reverse faulting event in NW Turkey (No. 7) is shown by opposing black arrows. The T axis for this event is not plotted in the inset.

For consistency, we have shown the direction of movement for the north side relative to the south side for all the events. There are several important characteristics of the pattern of slip vectors shown in Figs 11 and 12. The most obvious is that there appear to be two sets of slip vector directions: one group (predominantly normal faulting) with a roughly N–S slip vector, and another (predominantly strike–slip faulting) with slip vectors trending NE. The strike–slip events in the central and north Aegean have slip vectors that average $047 \pm 7°$ for those in Fig. 11, or $056 \pm 11°$ for those in Figs 11 and 12 combined. This is similar to the direction of 070° predicted for the motion of Eurasia relative to Turkey at this longitude, using the pole of rotation from Jackson & McKenzie (1984). However, we believe that the difference between this predicted value of 070° and the average slip vector from the seven strike–slip events in Fig. 11 of $047 \pm 7°$ is real and resolvable: the uncertainty in slip vector for these events is not as great as 20°. We conclude that the predicted slip direction between Turkey and Eurasia has been perturbed at this longitude by the N–S extension in the Aegean. There is a noticeable, and resolvable, change in the strike of the strike–slip faulting from NE in the western Aegean to ENE in the eastern Aegean, which is seen both in the fault plane solutions (compare events 3 and 9, and 16 and 15 in Fig. 7) and the bathymetry. However, it is not clear whether this change in strike is accompanied by a systematic change in slip vector: we do not think the data in Figs 11 and 12 are sufficiently dense to be conclusive. It is nonetheless certain that the slip vectors on strike–slip faults in the Aegean are different from those at the eastern end of the Sea of Marmara (e.g. in event 5), which are almost E–W.

Throughout the study region, the slip vectors on the normal faults are approximately N–S: clearly different from those on the strike–slip faults. The average slip vector in the eight normal faulting events west of the coast of Turkey in Fig. 11 is $345° \pm 16°$. If those from Fig. 12 are included, the average is $350° \pm 18°$. The difference between the slip vectors on the normal and strike–slip faults demonstrates that the faulting is not of the simple *linked* or *transfer* type that is seen when ridges are offset by transform faults in the oceans, and which is sometimes thought to have occurred in older extensional basins (e.g. Gibbs 1984): in those situations the slip vectors on both types of fault should be the same.

In central Greece there are no NE-trending earthquake slip-vectors, nor is there any evidence on land for a continuation of the NE-trending strike-slip faulting seen offshore in the North Aegean Trough. The geological structure of mainland central Greece is dominated by normal faults with a WNW strike (Mercier *et al.* 1976, 1979b; McKenzie 1978), many of which expose fault planes with striations that also trend NNW to North (Roberts & Jackson 1991, and Appendix B). It was the dramatic difference between the N–S slip vectors on the normal faults in central Greece and the NE-trending slip vectors on the strike–slip faults in the North Aegean Trough that led McKenzie & Jackson (1983, 1986) to postulate that block rotations about a vertical axis occurred in central Greece. The faulting in this region thus provides an illustration of the importance of considering slip vectors in continental tectonics: nearly all the earthquake focal mechanisms in the central Aegean have T axes trending approximately N–S (insets to Figs 11 and 12), and are thus consistent with N–S extension (Jackson & McKenzie 1988a). Only when the slip vectors are examined does it become clear that the Turkey–Eurasia motion cannot connect with the Hellenic Trench system without block rotations occurring in central

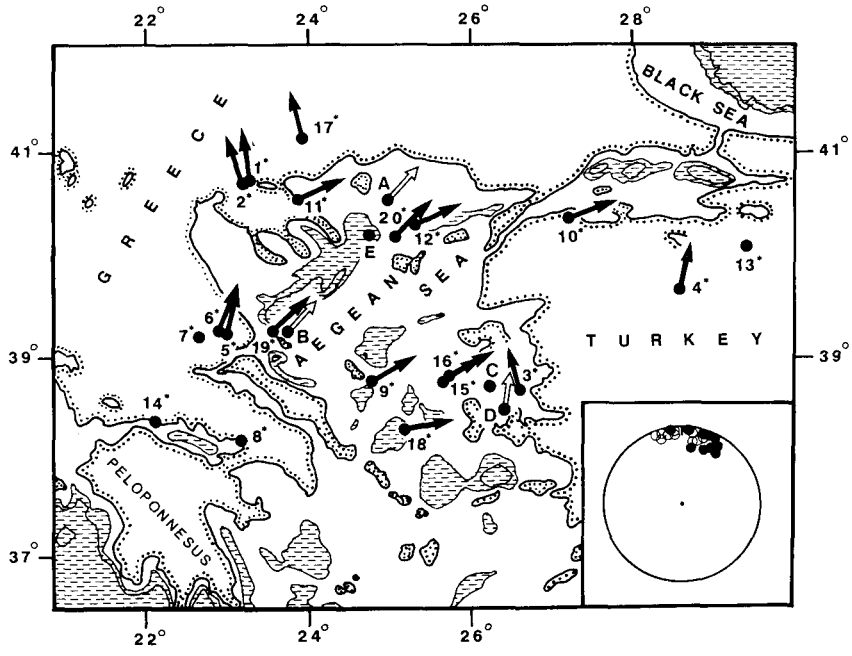

Figure 12. Horizontal projections of the slip vectors for the CMT solutions by Ekström & England (1989) and the USGS PDE. Numbers identify the events in Fig. 8 and Table 2. The polarity of the arrows follows the convention of Fig. 11. Open arrows are the slip vectors for the first motion solutions marked A to E in Fig. 8. Bathymetry is shaded below 600 m. The inset shows the T axes for these events, as in Fig. 11.

Greece. It is therefore important to examine the evidence for such rotations, and to consider their relations with the strain rates.

5 BLOCK ROTATIONS

5.1 Palaeomagnetic evidence

The best evidence that block rotations have occurred in central Greece comes from palaeomagnetic declinations measured in Neogene rocks. These data are reviewed by Kissel & Laj (1988) and Kissel *et al.* (1989), and need only be summarized here.

In the western part of the central Aegean, declinations of 026° ± 8° are seen in andesites 15 Myr old on the island of Skyros, and declinations (with a reverse polarity) of 228° ± 8° are seen in both volcanic rocks of 13 Myr and sediments of probable Pliocene age on the island of Evvia (Kissel & Laj 1988; Kissel *et al.* 1989). The interpretation of these measurements is not straightforward. On the basis of palaeomagnetic inclination data, Kissel & Laj (1988) conclude that during the period 60–10 Myr the Aegean area had the same latitudinal motion as Africa, and that the Miocene African pole should be used to calculate the rotation of these sites. This leads to an expected declination of 006°, and thus a clockwise rotation of Evvia and Skyros of 43° ± 8° and 20° ± 8° respectively. How is the age of this rotation constrained? A maximum age is given by the age of the rocks involved. However, Kissel & Laj (1988) and Kissel *et al.* (1989) argue that, because palaeomagnetic evidence shows no rotation of the Ionian islands during the period 12–5 Myr, and 25° ± 5° clockwise rotation since 5 Myr, the rotations observed in Evvia and Skyros occurred during the last 5 Myr. This interpretation is consistent with (**a**) the probable (but unquantifiable) Pliocene age of sediments in Evvia that have rotated 43° ± 8°, and (**b**) with the views that most of the extension in the Aegean occurred in the last 5 Myr (Mercier *et al.* 1989); that the clockwise rotation of the Ionian islands is related to their southwestwards movement over the thrust in the Hellenic Trench; and that most of the subduction in the present Hellenic Trench occurred in the last 5 Myr (Taymaz *et al.* 1990). However, the argument is not conclusive. Mercier *et al.* (1989) point out that during the period 12–5 Myr the Ionian islands were part of a stable region west of the zone of active shortening, and that it was not until the lower Pliocene that the site of active shortening jumped to its present position west of the Ionian islands.

Thus the lack of rotation in the Ionian islands during the period 12–5 Myr is no guarantee that rotations did not occur at that time farther east. We conclude that, while it is demonstrable that Evvia and Skyros have rotated clockwise (relative to their expected orientation) by about 40° and 20°, the timing of the rotation is uncertain: it probably occurred in the last 5 Myr, but could have occurred over 15 Myr.

The palaeomagnetic data from the eastern Aegean are even less easy to interpret as the apparent rotations are less uniform and their age more uncertain. Declinations of 006° ± 7° are seen in volcanic rocks of 18–15 Myr on Lesbos, and similar declinations are found farther north on the mainland, just east of the Dardanelles, in rocks of uncertain (probably Miocene) age (Kissel & Laj 1988; Kissel *et al.* 1989). Because of the inclination data, Kissel & Laj (1988) again use the Miocene African pole to calculate the expected declination (006°), and conclude that these data imply no net rotation. It seems safe to conclude that the net rotation of these rocks is not significantly different from zero, and certainly less than those on Evvia and Skyros. Farther south on the Turkish mainland the situation is more complicated: 100 km east of Lesbos declinations of 327° ± 9°

have been found in rocks 7 and 18 Myr old, while 100 km south of Lesbos declinations of 049° ± 16° were found in rocks 17–21 Myr old (Kissel *et al.* 1989).

Palaeomagnetic data from the northern Aegean is more sparse and, for our purposes, inconclusive because of either scatter in the declinations or the relatively old rocks in which they were measured. On the island of Limnos, Kondopoulou & Lauer (1984) report declinations varying from 349° ± 22° to 031° ± 9° in volcanic rocks of 17 to 22 Myr. In Thrace Kissel *et al.* (1986b) report declinations of 007° ± 7° in rocks 33–28 Myr old, while farther west in Chalkidiki, Kondopoulou & Westphal (1986) report declinations of 037° ± 9° in plutonic rocks 40 Myr old.

5.2 Structural evidence

It is, in principle, not possible to determine rigid body rotations uniquely using observations of faulting (see Jackson & McKenzie 1988a). Inferences about rotations can be made from fault slip data if some *a priori* information is assumed about the overall velocity field that the faulting must accommodate, as was done by McKenzie & Jackson (1983, 1986) in their discussion of the faulting in central Greece. Mercier *et al.* (1989, 1991) review the structural data from the north Aegean region. The principal tool of their analysis is the construction of an average regional stress tensor from measurements of slip on numerous faults of different orientation (Carey 1979). The main result of Mercier *et al.* (1989 and 1991) that is of interest to this study is that the principal direction of extension in the northern Aegean changed from NE–SW in the Pliocene–lower Pleistocene to N–S from the middle Pleistocene to the present day. On structural grounds alone, it is not possible to distinguish a rotation of the stress field that caused the faulting (anticlockwise from Pliocene to present) from a passive rigid-body rotation (clockwise) of the blocks within which the faults were measured. Mercier *et al.* (1989, 1991) argue that rigid block rotations are unlikely, because the same two extensional directions are observed in Lesbos and Thrace, where no significant net rotation of palaeomagnetic declination has occurred in rocks of 18–15 and 33–28 Myr (see above): they therefore favour a rotation of the stress field. This is a good argument, but may not be completely secure. The palaeomagnetic data in Lesbos and Thrace are from rocks that are relatively old, and the observation of no *net* rotation does not rule out the possibility that rotations (of opposite senses) occurred since the rocks were deposited (see also Mercier *et al.* 1991, who reach similar conclusions). This may seem far-fetched, but with adjacent rotations of different senses known in western Turkey (see above, Kissel & Laj 1988), the possibility exists. Furthermore, we do not believe that Thrace is the stable northern edge of the Aegean extensional domain (see later), and thus do not think that the similarity between extensional directions in Thrace and the north Aegean islands is a safe indication of the lack of block rotations. We think it likely that the conclusions of Mercier *et al.* (1989) are correct, but think that it is safer to conclude that the islands of the north Aegean (Lesbos, Thasos, Samothraki) and Thrace are part of the same rotational (or non-rotational) domain. We return to this evidence in the discussion on kinematics.

5.3 Geodetic evidence

It is possible to detect block rotations by geodetic means, if networks within the deforming region are linked to stable points outside. No such networks have yet been re-measured in Greece. Billiris *et al.* (1991) report the remeasurement in 1988 of a triangulation network installed in 1890–1990 within the actively deforming part of central Greece. As the 1890–1900 network was not linked to external stable regions of central Europe, it has no unique orientation and cannot be used to determine rotations unambiguously: the main result of the resurvey was to establish strain rates, which are used below. However, Billiris *et al.* (1991) analysed the resurveyed data assuming *a priori* that the northernmost part of the network had not rotated. They then found a displacement field across central Greece that was orientated NE–SW: this is the same as the direction of NE–SW right-lateral shear that is expected to cross central Greece to link the North Aegean Trough with the Hellenic Trench in the Ionian islands, but different from the slip direction on the faults (see Figs 11 and 12). This result is consistent with the clockwise rotation about a vertical axis of the fault-bounded blocks in the deforming zone, but does not prove it: the assumption Billiris *et al.* (1991) made to obtain the orientation of the network was the most reasonable they could make, but was entirely arbitrary.

5.4 Relations between rotations and strain rates in the western Aegean

The most compelling evidence for block rotations within the central and northern Aegean comes from palaeomagnetic studies. The palaeomagnetic declination data is not ideal, because signals with sufficient amplitude to overcome the noise are only obtained from rocks several million years old, and this in turn leads to uncertainty in the timing of the rotations. This problem is particularly serious in the Aegean, where it is clear that the orientation and rates of deformation have changed substantially over the last 10–15 Myr. The evidence for clockwise rotation is convincing on the islands of Skyros and Evvia in the western Aegean, and its timing is less uncertain here than elsewhere because of the many measurements in rocks 0–12 Myr old farther west, obtained by Laj *et al.* (1982). The uncertainty in timing is nonetheless a factor of two and the corresponding uncertainty in rotation rates is large, even if the rates were uniform, which is unlikely. Thus average rotation rates in Evvia and Skyros could be as high as $8° \text{ Myr}^{-1}$ or as low as $2° \text{ Myr}^{-1}$. The value of $5° \pm 3° \text{ Myr}^{-1}$ is probably realistic.

How is this rotation related to the strain rates across central Greece? The basic geometry of the deformation is described by McKenzie & Jackson (1983, 1986): the overall NE–SW motion across the region is accommodated by oblique (left-lateral and normal) slip on normal faults striking approximately WNW that rotate about a vertical axis (clockwise) and also about a horizontal axis as they move. Previous attempts to investigate this relation quantitatively (McKenzie & Jackson 1983, 1986; Jackson & McKenzie, 1988a, 1988b) did not have the slip vector and strain rate data that are now available. The best estimate of

the velocity across the deforming zone, from the south side of the Gulf of Corinth to the Sporades islands, comes from Billiris *et al.*'s (1991) resurvey of the 1890–1900 triangulation network. They obtained an extensional velocity, averaged over 100 years, of 12 ± 2 mm yr^{-1}. The direction of this velocity is uncertain (see above), but we will proceed assuming that it is in the same direction as the slip vectors on the strike–slip faults in the north and central Aegean (i.e. 047° ± 7°). There is no clearly defined boundary to the edge of the deforming zone, though the faulting in all the major graben and basin systems of central Greece dies out along strike to the SE, and does not appear to cross the Sperchios–Lamia valley in the north (Roberts & Jackson 1991). In the simplest models of distributed deformation there are no gradients of velocity along strike of the deforming zone, and the slip vectors on the major faults should be perpendicular to the zone boundary (McKenzie & Jackson 1983, 1986). In central Greece the average slip vector in the normal faulting earthquakes is 345° ± 16° (see above), which is similar to the direction of the striations seen on the major exposed fault planes in the region (Roberts & Jackson 1991). This would imply a boundary to the deforming zone with a strike of 075°, which is similar to the 090° assumed in earlier analyses. The average strike of the normal faults within the deforming zone is in the region of 305° ± 15°, based on geology and geomorphology (Roberts & Jackson 1991). The width across the strike of this zone, over which the strain was measured by Billiris *et al.* (1991), is about 130 km. We can now examine some of the models that have been suggested to link these observations.

McKenzie & Jackson (1983, 1986) discuss two simple models which fulfill the requirement that there is no gradient of velocity along strike of the deforming zone (in both, the slip vectors on the faults are perpendicular to the boundaries of the zone). They resolve the overall motion across the zone into a shear parallel to the zone boundary (Wa), and an extension perpendicular to the boundary

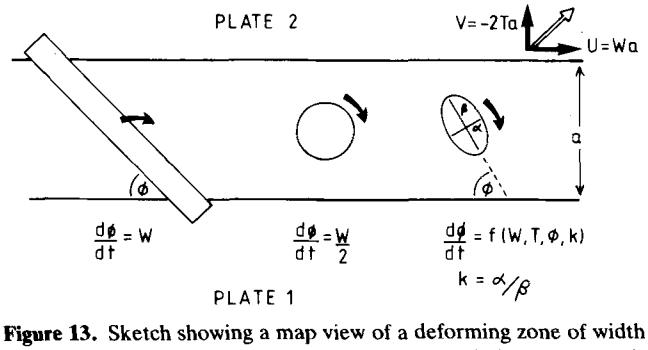

Figure 13. Sketch showing a map view of a deforming zone of width a separating two plates. The motion of plate 2 relative to plate 1 is shown by the white arrow, and can be resolved into components $-2Ta$ and Wa perpendicular and parallel to the zone boundary. The velocity gradient across the deforming zone is constant. The rates at which rigid bodies in the zone rotate depends on their size, shape, and orientation. Large blocks that span the zone (left) and move with the zone boundaries rotate at a rate W. Small equidimensional blocks within the zone (centre) rotate at $W/2$. The rotation rate of elliptical blocks depends on their shape (k) and orientation (ϕ) as well as on the velocity gradients T and W. See text for further discussion.

($-2Ta$), where a is the width of the zone (see Fig. 13). In this notation, the strain measured by Billiris *et al.* (1991) is resolved into components $Wa = 10.7 \pm 1.8$ mm yr^{-1} and $-2Ta = 5.4 \pm 0.9$ mm yr^{-1} for the orientations assumed above. The two models discussed by McKenzie & Jackson (1983, 1986) differ in the strike of the faults relative to the zone boundary (angle ϕ), and in their rotation rates.

In the first model (*the pinned block model*) the fault blocks span the width of the deforming zone and are constrained to move with the zone boundaries (Fig. 13, left). The overall motion across the zone should be perpendicular to the strike of the faults, and the rotation rate should be W (clockwise). In this case, the observed angle between the faults (strike 305° ± 15°) and the overall motion (047° ± 7°) is 102° ± 22°, which is not resolvably different from the predicted 90°. The predicted rotation rate is $W = 4.7 \pm 0.8°$ Myr^{-1}, which is within the range of $5° \pm 3°$ Myr^{-1} estimated from the palaeomagnetic data. We conclude that this *pinned* model is compatible with the observations, given their errors.

In the second model (*the floating block model*), the blocks are assumed to be small compared with the width of the deforming zone and roughly equidimensional (Fig. 13, centre). The rotation of such blocks is driven by the continuously deforming lithosphere beneath the seismogenic upper crust. Their strike relative to the zone boundary is given by $\tan \phi = -W/4T$, and their rotation rate should be $W/2$ (clockwise). In this case the observed value of ϕ is 50° ± 15° and the predicted value is about 44° ± 10°. The predicted rotation rate is 2.4° ± 0.4° Myr^{-1}. Thus this model also can not be excluded on the basis of fault strikes and rotation rates, though the rotation rates are perhaps rather low.

A third model, which is a variation on *the floating block* model of McKenzie & Jackson (1983, 1986), was suggested by Lamb (1987), who considered the rotation of elongated elliptical blocks in a velocity field that again fulfilled the requirement of no velocity gradients along the strike of the zone (Fig. 13, right). In this case the rotation rate depends both on the shape of the block (given by aspect ratio k, of the short to long axes of the ellipse) and its orientation ϕ_L, where $\phi_L = (180 - \phi)°$. Lamb's expression (his equation 7) for the rotation rate, R, is

$$R = (W/2)[(\cos 2\phi_L + \tan\theta \sin 2\phi_L)(1 - k^2)/(1 + k^2) - 1],$$

where $\theta = -\arctan(2T/W)$. If we assume $k = 0$ (i.e. long narrow blocks), take $\theta = 27° \pm 7°$, and $\phi = 50° \pm 15°$, then the predicted rotation rate is 4° Myr^{-1} clockwise with a range of from 2.4° to 5° Myr^{-1}. Thus this model may also not be discounted on the basis of rotation rates.

It is of interest to know whether the block rotations, which are such a common feature of continental tectonics, are driven by forces on their lateral boundaries or by the flow of the continuously deforming lithosphere beneath them. In the western Transverse Ranges of southern California fault slip and geodetic data favour, but not conclusively, block rotation in response to continuous flow below (Jackson & Molnar 1990). In the case of central Greece we must conclude that we cannot tell, because the errors in the observed rotation rates are large enough to allow both possibilities. Of the three simple models discussed above, the second (*the equidimensional floating*

block model) is probably the least appropriate, for two reasons. Firstly, the blocks do not appear to be equidimensional in central Greece: they form elongated narrow ranges and basins up to 100 km in length. Secondly, the angle ϕ between the strike of the blocks and the strike of the zone boundary is 45°, or possibly less, in central Greece. If ϕ is less than 45° the equidimensional blocks cannot remain in contact along faults, and the logic used by McKenzie & Jackson (1983) to calculate the relation between ϕ and the velocity field (W and T) breaks down. (This was pointed out to us by Simon Lamb, personal communication). Whatever the nature of the forces driving the rotations, it is unlikely that the rotation is uniform throughout the zone, and there is weak confirmation of this in the different palaeomagnetic declinations in rocks of similar ages on Evvia and Skyros. Variations in the rotation rate may be responsible for the segmentation of the normal fault systems bounding the major graben and ranges, that is such a striking feature of central Greece (Roberts & Jackson 1991).

We have examined the relations between faulting and rotations in this part of central Greece in some detail because it is where the strain and rotation rates are best determined. We discuss the rotations in a more regional context in the next section, where we will see that all three of the simple models discussed above are probably inappropriate for two reasons: (i) the velocity field is unlikely to be 2-D in this part of central Greece, and (ii) the rotations are probably not confined to an E–W striking zone with a non-rotating southern margin.

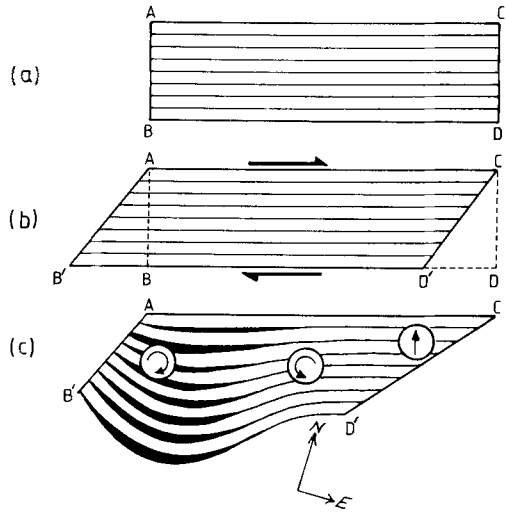

Figure 14. Sketches to illustrate a simple analogue for the deformation in the Aegean region. (a) Sideways view of a book with parallel sheets of paper. (b) If the book has no binding, then simple shear of the right-hand margin, such that CD rotates to CD′, produces a corresponding shear and rotation of the left-hand margin. The sheets remain in contact and do not rotate. (c) If the book (which has a soft lower cover) has a binding on its left-hand side, such that the line AB cannot increase in length, then shear of the left-hand margin, increasing the length of CD to CD′, produces shortening parallel to the sheets. This is balanced by extension as the sheets bulge out and gaps (in black) appear. Circles with arrows show the senses of rotation. Note that no rotation occurs in the region where there is no extension and the sheets remain parallel and in contact. North and east arrows are to facilitate a comparison with the Aegean (Fig. 9a).

6 KINEMATICS

6.1 Relations between strike–slip motion, extension and rotations

Fig. 9(a) summarizes the active tectonics of the central and northern Aegean region. The principal characteristics of the deformation are as follows.

(**a**) West of 31°E the right-lateral strike–slip faulting associated with the North Anatolian fault becomes distributed over several strike–slip faults that cross the Aegean Sea with a NE to ENE strike.

(**b**) These strike–slip faults do not cross central Greece to link with the Hellenic Trench. Instead they appear to end in deep basins bounded by normal faults with a NW or WNW strike, and with slip vectors trending about 350°. There are at least three such systems: the Kavala–Xanthi fault ending in the Strymon basin; the Saros–North Aegean Trough system ending in the western part of the Sporades basin; and the Edremit–central Aegean faulting ending in the Skyros basin. The basins NE of Andros and NW of Icaria may have similar origins.

(**c**) The density of palaeomagnetic observations over the age range 0–12 Myr along the western seaboard of Greece (Laj *et al.* 1982; Kissel & Laj 1988) demonstrates conclusively the clockwise rotation of this region by about 25°, relative to stable Europe or Africa, over the last 5 Myr. The evidence is strong that the islands of the western Aegean (Evvia and Skyros) have undergone a rotation of the same sense and similar magnitude. In the east, the rotations are less certain and apparently more complicated: there may be little or no rotation where the deformation is principally distributed strike–slip on parallel faults (between Lesbos and Thrace). Farther south on the Turkish coast, where normal faulting becomes more obvious, there is some evidence for both clockwise and anticlockwise rotation.

A simple 2-D analogue of this deformation style is available from everyday experience. Consider a book or magazine with a flexible cover, such as a telephone directory (Fig. 14a). If the book has no binding, so that is simply a stack of parallel paper sheets, then distributed simple shear, such that edge CD rotates to CD′, is accomplished by sliding the parallel sheets over each other, and the left hand edge rotates from AB to AB′ (Fig. 14b). The sheets do not rotate and the deformation resembles distributed strike–slip faulting on parallel faults. If the book has a binding, such that the left hand edge AB in Fig. 14a cannot change in length, then the distributed simple shear on the right hand edge (movement of D to D′) causes deformation like that in Fig. 14(c). Here, strike–slip faulting in parallel faults occurs only on the right-hand side. Towards the centre gaps (shaded in black) appear between the sheets, which start to bulge out towards the bottom of the picture. The gaps represent extension perpendicular to the top of the picture (line AC) which accompanies overall shortening in the orthogonal direction. In the case of Fig. 14(c), this style of deformation arises because the binding of the book is rigid and cannot change length: thus AB in Fig. 14(a) must equal AB′ in Fig. 14(c). But the same style of deformation will

arise even if the edge AB can change in length, but does not rotate clockwise as fast as the edge CD.

The sketch in Fig. 14c resembles the deformation in the Aegean region (Fig. 9a) in several ways. For comparison, axes showing north and east directions have been added to Fig. 14(c). The eastern side is dominated by distributed right-lateral strike slip faulting on faults that change in strike from ENE to NE. Normal faulting, with a WNW to NW strike, is most prevalent in the west, and responsible for the growth of basins (gaps in Fig. 14c). The structures (sheets in Fig. 14c) only start to rotate when they enter the region where there is N–S extension. In the west, the sense of rotation is clockwise, in the east it is anticlockwise. The palaeomagnetic evidence in the extensional region of the Turkish coast south of Lesbos is not easy to interpret, showing both clockwise and anticlockwise rotations. It is possible that the anticlockwise rotations are related to the rotation of the big strike faults (as in Fig. 14c), whereas the clockwise rotations are seen in some smaller blocks caught up in the right-lateral shear between them (see also Mercier *et al.* 1991; Nicholson *et al.* 1986).

A major difference between the simple book analogy in Fig. 14(c) and the deformation in the Aegean is that the change in strike, from NE in the east to NW in the west, is gradual in Fig. 14(c) whereas it is clearly abrupt in the north and central Aegean. The faulting in the Aegean also appears to be concentrated on a few major structures that dominate the topography and bathymetry, and not to be as continuous, at least in the upper crust, as the impression given by bending a book. It resembles more a series of slats that have rotated and broken, as illustrated in Figs 15(a and b). As in Fig. 14(c), the left-hand side of Fig. 15(b) has rotated less than the right-hand side, and it is this that has caused the extension to occur. We discuss why this boundary condition might apply in the Aegean in the next section. Note that the clockwise rotation of the eastern margin is not really the rotation of a rigid plate: it is a distributed simple shear as the motion on the North Anatolian Fault is spread over several sub-parallel strike–slip faults. There are some features of the sketch in Fig. 15(b) that have no significance in the context of the Aegean. One is that the largest gaps (extension) occur at the top of the picture, because this is required in going from the unbroken (Fig. 15a) to the broken state (Fig. 15b). In the case of the Aegean, the deformation is now occurring in the broken configuration. Similarly, there is no significance to where the change in strike (the break) in each slat occurs. For simplicity, Fig. 15(b) has been drawn so that the break points line up, but in reality their position may be controlled by pre-existing structural weaknesses.

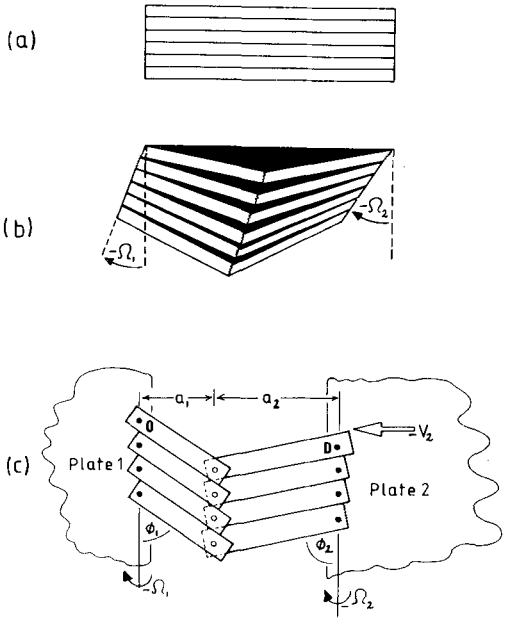

Figure 15. Sketches to illustrate the rotation of broken parallel slats. (a) Starting configuration, with parallel slats. (b) The right-hand margin of the slats has rotated more than the left. This has caused shortening parallel to the slats, which has been compensated by a rotation and breaking of the slats, which separate to produce gaps (in black). Compare with Fig. 14(c). (c) A simple model of broken rotating slats, which can be constructed with wood and screws. Filled circles are screws that attach the slats to the margins of plates 1 and 2. Open circles are screws that join only the two arms of each broken slat. The margins rotate at different rates, and the top screw (D) on the right-hand side can have a velocity $-V_2$ relative to the top screw (O) on the left-hand side. The analytical expressions for the velocity field in this model are derived in Appendix C. The negative signs for the rotation rates and velocity V_2 are to be consistent with the notation of McKenzie & Jackson (1983).

6.2 A simple block model

It is possible to investigate quantitatively one of the simplest configurations in which the deformation is accommodated by a system of broken slats, as illustrated in Fig. 15(c). This configuration may be constructed with wooden slats and screws. On the left- and right-hand margins, the slats are pinned at pivot points (screws) whose spacing remains fixed. At the break points each broken slat is held by a screw joining its two arms, but these screws do not remain a fixed distance apart. The left and right hand margins rotate relative to the top of the model (line OD in Fig. 15c), and the distance OD may shorten as the point D has a velocity V_2 perpendicular to the right hand margin. The instantaneous velocity field for this model can be calculated analytically, and is given in Appendix C. From the velocity field the slip vectors between the slats and their senses of rotations can be calculated.There are six parameters that control the solution: the two angular velocities of the margins (Ω_1, Ω_2); the velocity V_2 of point D; the orientation of the slats (ϕ_1 and ϕ_2); and the position of the break points (ratio a_1/a_2). Fig. 16 shows the calculated velocities of the break points and the slip vectors between the slats, for values of these six parameters that are reasonable for the situation in the Aegean. We have chosen $a_1 = 175$ km, $a_2 = 350$ km, $\phi_1 = 60°$, $\phi_2 = 75°$, $V_2 = 0$. For the rotation rates, we have chosen $-5°\,\mathrm{Myr}^{-1}$ for the western margin of Greece (Ω_1), and $-10°\,\mathrm{Myr}^{-1}$ for the eastern margin, in Turkey (Ω_2). These values are similar to the $5°\,\mathrm{Myr}^{-1}$ (clockwise) rotation rate estimated by Laj *et al.* (1982) from palaeomagnetic measurements in western Greece, and to the slip rate on the North Anatolian fault of about $30\,\mathrm{mm\,yr}^{-1}$ (Jackson & McKenzie 1984) distributed over 200 km ($8.6°\,\mathrm{Myr}^{-1}$).

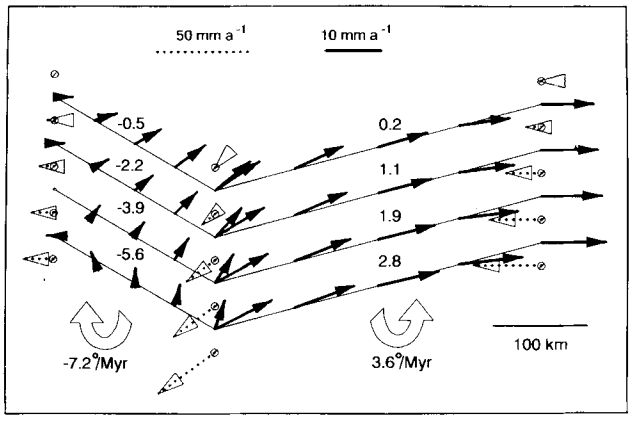

Figure 16. Velocities and rotation rates for the broken slat model (Fig. 15c), calculated using the expressions in Appendix C, with dimensions and geometry comparable to those in the Aegean (see text). Slats are drawn in thin lines. Screws are open circles with a bar. The spacing of the screws on the left- and right-hand margins is 50 km. Slip vectors are thick lines with arrows, showing the velocity of the north side relative to the south (the same convention as in Figs 11 and 12) at the point on the slat boundary marked by the foot of each arrow. The length of each arrow is proportional to the magnitude of the velocity (see the scale at the top). Broken lines show the velocity vector of each screw (in the direction away from the screw) relative to the origin (top left hand screw): again, the length of the line is proportional to the magnitude of the velocity, with a separate scale at the top. Curled open arrows show the senses of rotations of the left- and right-hand arms, with rates given for the bottom (5th) slat on each side. Rotation rates increase downwards: the rates for the other slats are marked on each side (in °/Myr). Note that the eastern set of slip vector arrows shows the distributed shear of the North Anatolian Fault.

The purpose of Fig. 16 is to illustrate general features of the velocity field in the simple broken slat model, not to produce a detailed simulation of the tectonics of the Aegean. Fig. 16 shows the slip vectors on the faults separating the slats, and their length is proportional to their magnitude. The slats are pinned at 50 km intervals along the rotating margins. The most important general feature is that normal faulting is dominant in the west and strike–slip faulting is dominant in the east. The slip vectors in the southwest are approximately N–S, with a scatter similar to that observed in Figs 11 and 12. We do not observe the NE slip vectors predicted at the northern end of the western set of slats, though there are no reliable focal mechanisms north of the 1978 Thessaloniki earthquakes. Of the two mechanisms in the NW of Greece and Albania in Fig. 18, one, (Q: 1967 May 1) is well constrained by first motions (Anderson & Jackson 1987) and has one slip vector directed NE, while the other (R: 1967 November 30) is less well constrained. Slip vectors on the eastern slats of the model show mainly strike–slip motion, with components of extension or even shortening perpendicular to the faults that are relatively small. The precise directions are dependent on the values of the parameters that we used. Nonetheless, the general agreement with the geometry of the deformation in Figs 9, 11 and 12 is remarkable. In the context of this model, the anomalous reverse faulting event in western Turkey (event 7 in Fig. 7) may not be surprising, and may be taking up a small shortening component on faults whose main motion is strike slip. In the model, the shortening between the eastern parts of the eastern arms is partly caused by the imposed constant separation of the screws along the eastern margin. In NW Turkey, N–S extension on E–W trending normal faults occurs, and this boundary condition may not be appropriate. Nonetheless, the shortening in event 7 occurs in a region where there are no conspicuous E–W normal faults. The abrupt change in slip vector near the break points on the slats is another important feature of the model in Fig. 16, and is similar to that seen in the Aegean, for example near Skyros. The rotations of the two sets of arms are in opposite senses and increase in rate towards the bottom of the picture (south). Note that the expected palaeomagnetic rotation rate of the eastern slats is much slower than that of the western slats. The rates of rotation of the slats in Fig. 16 are similar to those in the Aegean (see caption to Fig. 16, and below). The velocities of the break points on each slat are also shown in Fig. 16, and are all directed SW, with a velocity for the bottom (most southerly) screw of 40 mm yr^{-1}, similar to that estimated for the Aegean as a whole (e.g. Jackson & McKenzie 1988b). Note that the slip vectors on the western sets of slats are largest (indicating fastest velocities) close to the break points, and decrease towards the western margin. This is also seen in Greece, where the best-developed extensional structures are in the eastern coastal regions of mainland Greece, rather than farther west. But the slip rates are greatest on the eastern arms, where the motion is mostly strike–slip. The normal component at the western end of the eastern arms is nonetheless substantial (comparable to the normal component on some of the western slats). Thus, even though the motion on the eastern arms is mostly strike–slip, it can still produce deep basins, such as those in the central and northern Aegean. This may account for the relative lack of normal faulting events in the central and northern Aegean, pointed out earlier.

Two points must be appreciated when comparing the broken slat model with the deformation in the Aegean. Firstly, we emphasize that the simple model in Fig. 16 and Appendix C describes only the instantaneous geometry, like the earlier block models of McKenzie & Jackson (1983, 1986). The finite evolution of the deformation is a much more complicated problem (see McKenzie & Jackson 1983). Consequently, the southern edges of the model would not correspond to the Hellenic Trench, but to the edge of the seismically active region in the central and northern Aegean, located approximately along the volcanic arc in the Cyclades. The Sea of Crete, which lies between the volcanic arc and the Hellenic Trench (Fig 2b and 9b) is currently almost aseismic (Fig. 1), though it has been stretched perhaps more than any other part of the Aegean (Le Pichon & Angelier 1979, 1981; Angelier *et al.* 1982). This extension, which is no longer thought to be active, took place in the late Miocene–Pliocene, and is not simulated by the motions of the broken slat model: it is discussed further by Sonder & England (1989). The outer part of the Hellenic arc, close to and immediately above the thrusting in the trench, is currently extending in an E–W direction, perhaps related to the lengthening of the outer arc as the bend or 'kink' in the central Aegean develops (see Lyon-Caen *et al.* 1988).

Secondly, the model must not be taken to imply that we believe that continental deformation can usefully be described by subdividing the lithosphere into an increasing number of smaller and smaller plates. We think that at large length scales and within the lithosphere beneath the seismogenic layer, the deformation resembles that of a continuum. However, in the upper crust, this apparently continuous velocity field is evidently accommodated by discontinuous motion, concentrated on major faults. The question then is: how do the faults do it? To this extent, simple descriptive models such as that in Fig. 15(c) are useful. The related question, of how the motions of the upper crust are coupled to those at depth, is the reason for considering the relations between strain rates and rotation rates, such as in Section 5.4 (see also McKenzie & Jackson 1983; Jackson & Molnar 1990).

Thus, in the broken slat model the Peloponnese corresponds to the area SW of the western slats and rotates clockwise relative to Europe. It can now be seen why the simple earlier block models of McKenzie & Jackson (1983, 1986), which are discussed in Section 5.4, are probably unrealistic: the palaeomagnetic declinations observed in Evvia and Skyros may not be revealing rotations relative to a non-rotating southern boundary. In the broken slat model there is little *relative* rotation between the southernmost block (*cf.* Peloponnese) and the adjacent blocks to the north (*cf.* Locris and Evvia).

6.3 Seismic strain rates

It is of interest to know whether the moment release in earthquakes can account for the deformation required by the broken slat model. In Appendix C we show how the summed moment tensors for both left and right hand sets of slats may be calculated. The moment tensors do not depend on the number of slats or faults in each set, but only on the product of their number and the spacing between them: i.e. on the total length of the margins in the x direction (Figs 15c and C1). The horizontal components of the moment tensor are also independent of the dips of the faults. We calculated the predicted horizontal components of the moment tensors for the left and right sets of slats, using the configuration and dimensions of the model shown in Fig. 16, and assuming a value for the rigidity, μ, of 3×10^{10} N m^{-2} and for the seismogenic thickness of 10 km. The component of vertical thinning (zz) may be obtained from the xx and yy horizontal components, as the three of them must sum to zero to preserve volume.

To obtain the observed seismic moment rate, we examined earthquakes with magnitude ≥ 6.0 in the time interval 1909 to 1983. For comparison with the model in Fig. 16, we chose events that occurred within the latitude–longitude box 38°–42°N 22°–28°E (Table 4). To calculate moment tensor components for each earthquake, we needed to know both the scalar moment and the focal mechanism. Our approach to doing this is that followed by Jackson & McKenzie (1988a,b) and Ambraseys & Jackson (1990). Focal mechanisms were either taken from Tables 1 and 2 in this paper, or were assigned on the basis of first motions, surface faulting, or proximity to other events. Scalar moments were obtained from three different sources: from values given in Tables 1 and 2; from surface faulting; or from an empirical $M_s : M_o$ relation. We used two such relations: Ekström & Dziewonski's (1988) global relation, and also their continental relation. There is evidence that the global relation systematically overestimates M_o for a given M_s in the Aegean (see Ekström & England 1989; Jackson & McKenzie 1988b; Ambraseys & Jackson 1990), and the continental relation is likely to be more appropriate. These data are listed in Table 4.

In Table 5 we compare the observed and predicted moment rate tensor components for both sets of slats. To ease the comparison with the previous work of Jackson & McKenzie (1988a,b), Ekström & England (1989) and Ambraseys & Jackson (1990), we have rotated all the moment rate components into the frame in which x = east, y = north and z = up are positive. We give two estimates of the observed components, using both the continental $M_s : M_o$ relation (which we regard as giving the minimum likely estimate) and the global relation (which we regard as giving a maximum likely estimate). The realistic uncertainties in each observed component are likely to be around 50 per cent, arising from an uncertainty in M_s alone for the older events (see Jackson & McKenzie 1988a). On the left-hand side, the model predicts larger xx and xy components than are observed, reflecting the lack of earthquakes in the north with the expected NE directed slip vectors on NW-striking faults (Figs 12 and 14). Such faults exist (Fig. 9), but have not been seismically active this century. The observed and predicted yy and zz components agree well. On the right-hand side, the observed and predicted xx and yy components are similar, while the seismicity accounts for a more negative zz component and a smaller xy component than is predicted by the model. The zz discrepancy arises from the E–W striking normal faulting in western Turkey, which is not a feature of the model (recall that we made the simplifying assumption that the separation of the screws along the eastern margin remains constant: see Section 6.2). The xy discrepancy is caused by there being insufficient right-lateral strike–slip on faults trending WSW: the observed value for this component is almost all contributed by the four largest events, on 1912.8.9, 1932.9.6, 1953.3.18 and 1981.12.19.

The agreement between observed and predicted components is encouraging. The left-hand slats should be dominated by N–S extension and crustal thinning, and the right-hand slats should be dominated by E–W shortening and N–S extension, as is observed. This much is not surprising, as we used the orientations of the faults and slip vectors to formulate the model in the first place. However, there is no circularity in the assertion that the absolute values of some of the observed and predicted components are similar. Those that differ significantly may be because either there has been insufficient seismicity on some faults this century (e.g. xx and xy on the left slats, and xy on the right slats), or because of deformation that is not predicted by the model (zz on the right slats). Note particularly that the N–S extension (yy component) is in agreement on both sides, so that essentially all this component of the velocity field can be accounted for by the large earthquakes, as noted by Jackson & McKenzie (1988a).

We also calculated the predicted moment rate components for a subset of slats, containing the southernmost

Table 4. Source parameters used for estimating moment rates.

Date	Lat	Long	M_s		M_oc	M_oo		M_og	str	dip	rake		
1909.1.19	38.70	26.90	6.0	A	1.7	0.0		2.0	(60	90	180)	r	3(53.3.18)
1912.8.9	40.75	27.20	7.4	Af	57.5	60.0	f	173.8	68	55	-145	r	2
1912.8.10	40.75	27.20	6.3	A	3.5	0.0		4.5	(68	55	-145)	r	3(12.8.9)
1912.9.13	40.10	26.80	6.9	A	13.8	0.0		30.9	(68	55	-145)	r	3(12.8.9)
1914.10.17	38.20	23.50	6.2	A	2.8	0.0		3.4	(100	45	-90)	l	4
1919.11.18	39.10	27.40	6.9	A	13.8	0.0		30.9	(270	45	-90)	r	4
1923.12.5	39.90	23.20	6.4	A	4.4	0.0		6.1	(315	45	-45)	l	4
1928.3.31	38.20	27.40	6.5	A	5.5	0.0		8.2	(90	45	-90)	r	4
1928.4.22	38.00	23.00	6.3	A	3.5	0.0		4.5	(264	42	-80)	l	3(81.2.24)
1930.3.1	39.60	23.20	6.0	A	1.7	0.0		2.0	(310	45	-70)	l	4
1931.3.8	41.30	22.50	6.7	A	8.7	0.0		15.5	(271	42	-74)	l	3(78.6.20)
1932.9.26	40.50	23.90	6.9	A	13.8	0.0		30.9	(72	73	-168)	r	3(83.8.26)*
1932.9.29	40.50	23.70	6.2	K	2.8	0.0		3.4	(72	73	-168)	r	3(83.8.26)*
1933.5.11	40.50	23.70	6.3	K	3.5	0.0		4.5	(72	73	-168)	r	3(83.8.26)*
1935.1.4	40.70	27.60	6.4	A	4.4	0.0		6.1	(100	40	-90)	r	3(64.10.6)
1938.7.20	38.30	23.80	6.1	A	2.2	0.0		2.6	(290	45	-70)	l	4
1939.9.22	39.10	27.00	6.5	A	5.5	0.0		8.2	(262	41	-70)	r	3(79.6.14)*
1941.3.1	39.70	22.40	6.1	A	2.2	0.0		2.6	(58	41	-128)	l	3(80.7.9a)
1944.10.6	39.70	26.80	6.8	A	11.0	0.0		21.7	(262	41	-70)	r	3(79.6.14)*
1949.7.23	38.70	26.70	6.6	A	6.9	0.0		11.3	(262	41	-108)	r	3(79.6.14)*
1953.3.18	40.00	27.40	7.2	Af	28.8	100.0	f	87.1	60	90	180	r	2
1954.4.30	39.30	22.20	6.7	Af	8.7	0.0		15.5	(300	45	-70)	l	2
1955.4.19	39.30	23.10	6.2	A	2.8	0.0		3.4	(58	41	-128)	l	3(80.7.9a)
1957.3.8a†	39.40	22.70	6.5	A	5.5	0.0		8.2	(58	41	-128)	l	3(80.7.9a)
1957.3.8b†	39.40	22.70	6.6	A	6.9	0.0		11.3	(58	41	-128)	l	3(80.7.9a)
1964.10.6	40.10	28.00	6.9	Af	13.8	4.1		30.9	100	40	-90	r	1
1965.3.9	39.40	24.00	6.5	A	5.5	1.5		8.2	135	85	15	r	1
1965.7.6	38.40	22.40	6.4	A	4.4	0.0		6.1	90	74	-115	l	5
1967.3.4	39.20	24.60	6.8	A	11.0	2.4		21.7	313	43	-56	l	1
1968.2.19	39.40	25.00	7.3	A	40.7	34.5		123.0	311	90	20	r	1
1970.4.8	38.43	22.66	6.2	A	2.8	0.9		3.4	75	67	-94	l	1
1975.3.27	40.42	26.14	6.7	A	8.7	2.0		15.5	68	55	-145	r	1
1978.6.20	40.73	23.25	6.4	Af	4.4	4.2		6.1	271	42	-74	l	1
1980.7.9a‡	39.23	22.76	6.4	Af	4.4	8.7		6.1	58	41	-128	l	1
1980.7.9b‡	39.23	22.59	6.0	A	1.7	0.0		2.0	(58	41	-128)	l	3(80.7.9a)
1981.2.24	38.10	22.84	6.7	Af	8.7	8.8		15.5	264	42	-80	l	1
1981.2.25	38.14	23.05	6.4	Af	4.4	4.0		6.1	241	44	-85	l	1
1981.3.4	38.18	23.17	6.2	Af	2.8	2.7		3.4	230	45	-90	l	1
1981.12.19	39.22	25.25	7.2	U	28.8	26.0		87.1	60	79	175	r	1
1981.12.27	38.91	24.92	6.4	A	4.4	3.8		6.1	216	79	175	r	1
1982.01.18	39.96	24.39	6.9	U	13.8	7.3		30.9	233	62	187	r	1
1983.08.06	40.14	24.74	6.9	U	13.8	19.4		30.9	47	83	180	r	1

† Origin times: 1957.3.8a [12:14]; 1957.3.8b [12:21]

‡ Origin times: 1980.7.9a [02:11]; 1980.7.9b [02:36]

Earthquake parameters used for summing seismic moment tensors. Columns are: date; latitude, longitude; M_s, followed by A if taken from Ambraseys (various publications and personal communications), K if taken from Karnik (1967), or U if taken from the USGS PDE, and by an f if the event produced surface faulting; three estimates of M_o in units of 10^{18} N m, based on Ekström & Dziewonski's continental M_s : M_o relation (c), or their global relation (g), or based on surface faulting (o); strike, dip and rake, in parentheses if assumed; l or r, depending on whether the event was assigned to the left or right set of slats; a number indicating on what basis the focal mechanism was assigned for each event: (1) is taken from this paper, based on P, SH or CMT solutions; (2) is from observed surface faulting; (3) is based on nearby events that are given in parentheses, followed by an * if the nearby event is in tables 1 or 2 rather than this table; (4) is a guess based on the orientation of nearby active faults; (5) is based on first motion P wave polarities.

Table 5. Observed and predicted seismic moment rates.

[units: 10^{17} N m/yr, co-ordinate system x=east, y=north, z=up (+ve)]

	all left hand slats				all right hand slats			
	xx	*yy*	*zz*	*xy*	*xx*	*yy*	*zz*	*xy*
minimum seismic rate	-0.1	11.0	-10.9	-0.1	-22.3	36.7	-14.4	8.6
maximum seismic rate	-0.2	17.2	-17.0	0.1	-59.6	91.9	-32.3	22.9
rate calculated from slat model	6.0	10.8	-16.8	8.3	-21.9	21.7	0.2	38.0

Moment rate summed over two southernmost *left faults*

	xx	yy	zz	xy
calculated rate	1.2	5.4	-6.6	2.6

Eigenvalues of calculated moment rate tensor of two southernmost left faults

value	6.64	-0.04	-6.60
plunge	0.0	0.0	90.0
azimuth	205.5	295.5	

two faults on the left-hand side. We did this using the same dimensions and configurations of the model that are shown in Fig. 16 and discussed above. The reason for considering this subset was that it corresponds roughly to the area occupied by the geodetic, network in central Greece analysed by Billiris *et al.* (1991), and discussed in Sections 5.3 and 5.4. The predicted moment rate tensor (Table 5) has one eigenvalue in the horizontal plane that is almost zero. It therefore approximately corresponds to uniaxial horizontal extension of 73 mm yr^{-1} in the direction 206°. This is comparable, within errors, to the average extension rate of 110 ± 28 mm yr^{-1} in the direction 210° measured by Billiris *et al.* (1991, Fig. 4).

7 DISCUSSION

We have shown that the instantaneous deformation of the central and northern Aegean resembles that of a simple set of broken slats attached to rotating margins, as in Figs 15 and 16. The model we have investigated here differs from others that describe the rotations of the western and eastern sides of the Aegean (e.g. Kissel & Laj 1988; Sorel 1989) in that it relates the deformation in the Aegean directly to the distributed westward motion of Turkey, and it is quantitative. Its reasonable success in matching slip vectors, strain rates and rotations raises several questions.

A crucial feature of a broken slat configuration in Figs 15 and 16 is that the 'rotation' (in reality, the distributed simple shear) of the eastern margin is faster than the rotation of the western one. There is some direct evidence for this in the Aegean region. The palaeomagnetic measurements of Laj *et al.* (1982) on the western margin of Greece demonstrate a clockwise rotation of about $5° Myr^{-1}$ over the last 5 Myr. Jackson & McKenzie's (1984) estimate of $32 mm yr^{-1}$ for the slip on the North Anatolian Fault, if distributed over 200 km (between Lesbos and Thrace), gives a rotation rate for the western margin of $9° Myr^{-1}$, which is close to the 2:1 ratio used in Fig. 16. Why should the rotation rate of the western margin be less than that required to accommodate the distributed shear of the eastern margin? One reason is that the right-lateral strike–slip motion is distributed over a greater width. But we think the main reason is that the western margin is prevented from behaving in the simple manner shown in Fig. 14(b) by its collision with the southern Adriatic and Apulia region. The shortening along the coast of Albania and NW Greece occurs within continental crust and is resisted by buoyancy forces: only south of about 38.5° N is the western margin of Greece flanked by oceanic crust, which allows shortening to be accommodated easily by overthrusting in the Hellenic Trench. The transition is manifest by the distribution of deep earthquakes and volcanic activity associated with the subduction zone (Fig. 2b). We believe that the resistance to the westward motion of the western margin caused by the continental collision in Albania and NW Greece is the reason why it rotates less rapidly than is needed to accommodate all the distributed simple shear in the east. This is why the relative magnitudes of the rotations used to generate Figs 15(b) and 16 are appropriate, and is what leads to the extension, as the southern margin of the Aegean moves over the Mediterranean Sea floor. This is illustrated schematically in Fig. 17. Our description of the kinematics is thus similar to that of Brunn (1976), who also suggested that the extension in Greece and the formation of the Aegean arc were results of bending in response to E–W shortening.

The original objective of this study was to examine the connection between the westward motion of Turkey relative to Europe and the extension in the Aegean, and also the transition from localized strike–slip motion on the North Anatolian Fault to the distributed deformation farther west. The kinematics of the deformation is now clearer: it is because the strike–slip faulting becomes distributed in NW Turkey that rotation of the western margin of Greece and Albania must occur, but because this rotation is insufficient to accommodate the distributed shear, extension in a N–S direction results. The geometry of the deformation at the

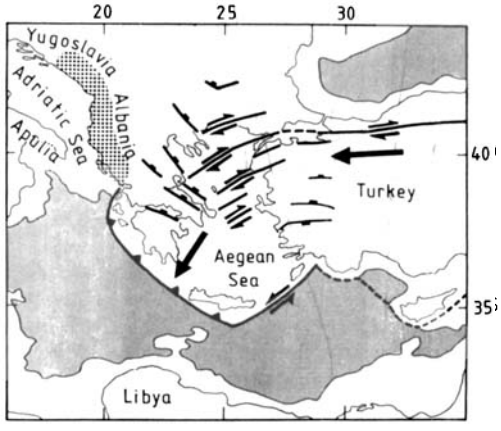

Figure 17. Sketch of the motions in the Aegean region. Faults are shown simplified and by thick lines: those with predominantly normal faulting have blocks in their hanging walls; predominantly strike–slip faults are marked by arrows. The Hellenic Trench has filled teeth on the overriding (Aegean) side. The dark shaded regions of the Mediterranean and Black Seas have water depths greater than 1000 fathoms (1800 m) and are approximately coincident with the regions underlain by oceanic crust. Continental crust is in white. Large arrows show the westward motion of Turkey and SW motion of the southern Aegean, both relative to Eurasia. The hatched region of coastal Yugoslavia and Albania is where active continental shortening and thickening are occuring, caused by the collision of this region with the Adriatic and Apulia platforms. It is this collision that resists the westward motion of Turkey, Greece and the Aegean, and forces the Aegean Sea SW, where it can easily override the Mediterranean oceanic crust in the Hellenic Trench.

moment resembles a set of broken slats (Figs 15 and 16), and can take up the westward motion of Turkey without requiring NE-trending right-lateral strike–slip faulting to cross central Greece. In the context of this geometry it is not surprising that the limited information on strain rates and rotations in central Greece (Section 5.4) is more compatible with the behaviour of elongated, rather than equidimensional, blocks. Furthermore, it is clear that not all of the NE–SW right-lateral shear passes through this part of central Greece, as originally assumed by McKenzie & Jackson (1983, 1986), who therefore predicted unrealistically high rotation rates. In addition, there is no reason to expect the rotations observed palaeomagnetically on Evvia and Skyros to be much different from those observed in adjacent regions along strike to the NW. The lack of a significant difference is supported by the observations of Mercier *et al.* (1991), who compared the trends of early Tertiary fold axes north and south of the Sperchios River (Fig. 9b), and found them to be approximately the same. Recall that in one of their analyses of the geodetically determined strain field in central Greece, Billiris *et al.* (1991) assumed that the top of the network did not rotate relative to Europe (Sections 5.3 and 5.4). In the broken slat model (Fig. 16) the rotation rates of the left-hand slats relative to the top of the model (*cf.* Europe) decrease rapidly northwards, suggesting that the assumption made by Billiris *et al.* (1990) is reasonable: though we emphasize, as before, that we cannot prove (and its agreement with any model does not demonstrate) its validity.

It is reasonable to ask why the strike–slip faulting

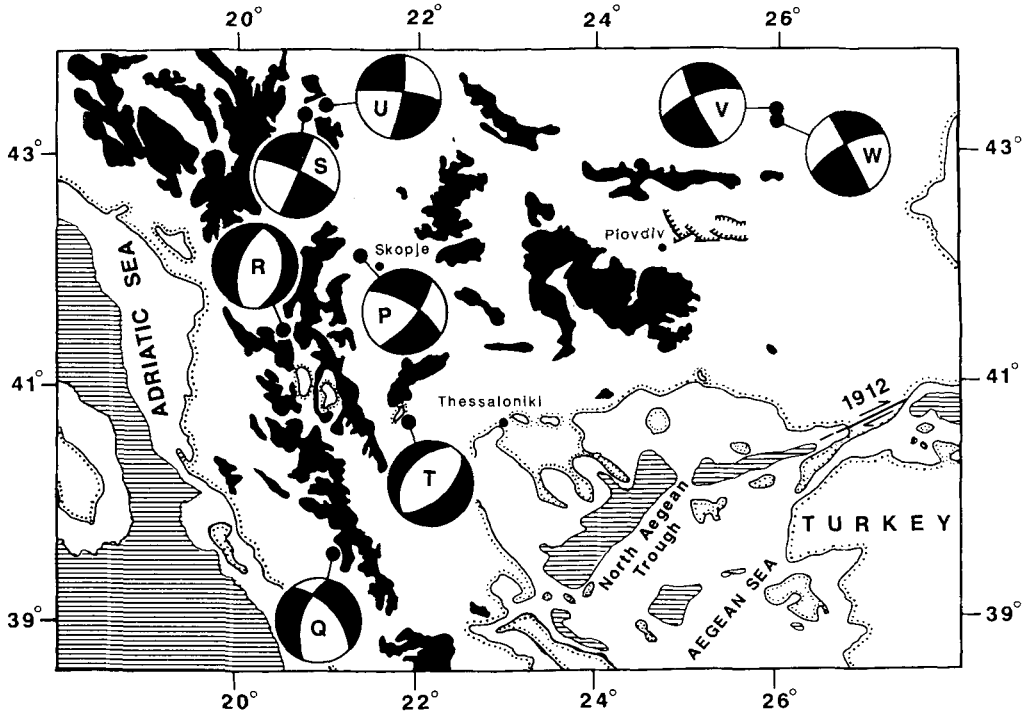

Figure 18. Map of Albania, southern Yugoslavia, Bulgaria and northern Greece, showing first motion solutions (from Anderson & Jackson 1987) and CMT solutions (from the USGS PDE), for events listed in Table 4. Topography is shaded above 1000 m, and bathymetry below 600 m. The faulting associated with the 1928 earthquakes near Plovdiv is taken from Richter (1958).

becomes distributed west of 31°E. One answer is that it is because of the extension, which is nearly always distributed over relatively wide regions on the continents, partly because this is the natural behaviour of a continuously deforming lithosphere (England, Houseman & Sonder 1985), and partly because of the buoyancy forces related to the generation of crustal thickness contrasts. The extension may be expected to distribute the strike–slip motion with it. This answer is not really satisfactory, because we have already argued that the extension is a consequence of the distributed strike–slip. We think it probable that the strike–slip motion became distributed as a result of the collision between the NW Greece and Albanian seaboard and the Apulia–Adriatic platform, which hindered the westward motion of Turkey, Greece and the Aegean. This sequence of events, if correct, would explain the apparent change in the direction of the extensional strain axis in the north Aegean observed by Mercier *et al.* (1989, 1991), from NE in the Pliocene (consistent with E–W right lateral shear) to N–S at the present day.

The dynamics of the deformation is now self-sustaining. The high topography in eastern Turkey and the Caucasus drives the westward motion of Turkey, and now that the extension in the Aegean has pushed continental material over the oceanic crust of the eastern Mediterranean to form a subduction zone, the sinking lithosphere slab beneath the Hellenic Trench can maintain the extension (McKenzie 1978; Le Pichon 1982; Wdowinski, O'Connell & England 1989). We do not know why the points which mark the abrupt changes in fault strike in the central and northern Aegean (the *break points* in the broken slat model) are where they are, whether they are related to the structure of the orogenic belt resulting from the late Mesozoic–early Tertiary shortening of the region (Aubouin 1965), or whether the slats were originally unbroken and continuous (as implied in the sketches of Figs 14 and 15). If the structures were originally continuous, then it should, in principle, be possible to estimate the offset on the North Anatolian Fault from their present shape, using simple models like those in Figs 14(c) and 15(b). In practice, because the western and eastern margins of the rotating structures are so poorly defined, and because some of the shape may have been accentuated by extension related to the sinking slab rather than motion on the North Anatolian Fault, the uncertainties in such estimates are large. Such estimates also require the northern boundary of the deforming zone to be identified. The extension clearly continues north of Greece into Bulgaria, as demonstrated by the Plovdiv earthquakes of 1928 (Fig. 18, and Richter 1958). Fig. 18 shows focal mechanisms in Albania, Bulgaria and southern Yugoslavia, taken from Andersen & Jackson (1987) and CMT solutions reported in the PDE. They are listed in Table 6. If the NE-trending nodal planes were the fault planes in the

Table 6. Mechanisms of earthquakes in Albania, South Yugoslavia and Bulgaria, shown in Fig. 18.

Code	Date (d m y)	Origin Time (h m s)	Location Lat. N(°)	Location Long. E(°)	I.S.C m_b	I.S.C h (km)	Str. (°)	Dip (°)	Rake (°)	Ref.
P	26.07.1963	041712.5	42.10	21.40	5.5	5	303	74	-21	*
Q	01.05.1967	070900.5	39.50	21.10	5.6	11	197	56	-44	*
R	30.11.1967	072351.5	41.41	20.44	6.0	21	200	58	-80	*
S	18.05.1980	200257.5	43.29	20.84	5.7	9	294	83	0	*
T	09.07.1984	185709.6	40.68	21.83	5.1	10	212	38	-105	*
U	07.09.1984	004441.8	43.31	20.96	5.1	13	278	78	-9	†
V	21.02.1986	053955.9	43.32	25.97	4.8	21	248	67	-170	†
W	07.12.1986	141709.6	43.27	25.91	5.2	21	243	71	175	†

* After Anderson & Jackson (1987).

† After PDE monthly listings.

strike–slip solutions, a case can be made for the distributed right-lateral strike–slip motion continuing as far north as 43°N, and perhaps causing the change in trend of the Albanian coastline near 42°N (Fig. 9a): but we cannot distinguish which planes are the fault planes with the data available. To the west, the normal faulting continues west of the Pindos mountains (event Q in Fig. 18) and into northern Albania (event R).

8 CONCLUSIONS

Three principal effects dominate the active tectonics of the Aegean region:

(a) the westward motion of Turkey relative to Europe, which is accommodated by localized slip on the North Anatolian Fault in central Turkey, but by distributed right-lateral shear in NW Turkey, the Aegean Sea and Thrace;

(b) the collision between the Albania–NW Greece margin and the Apulia–Adriatic platform in the west, which leads to shortening of continental crust and a consequent resistance to the rotation of Greece and Albania that is necessary to take up the distributed right-lateral shear; and

(c) the subducted lithosphere slab beneath the southern Aegean, which generates extension in the lithosphere above it, as it sinks into the mantle.

The dramatic change in the character of the deformation, from mainly strike–slip in the east to mainly normal faulting in the west, is related to the failure of the western seaboard of Greece and Albania to rotate rapidly enough to accommodate the westward motion of Turkey. It is this that probably initiated the extension in the Aegean Sea, causing its southern margin to override the oceanic crust of the eastern Mediterranean, and leading eventually to the establishment of a sinking slab that accentuated and helps sustain the deformation. A simple model, involving broken slats attached to margins that rotate, is able to reproduce quantitatively many of the features of the instantaneous deformation field seen in the central and northern Aegean region.

ACKNOWLEDGMENTS

We thank J.-L. Mercier, X. Le Pichon, N. Ambraseys and an anonymous reviewer for helpful reviews, Y. Liotier and J.-L. mercier for sending us preprints of their work, and P. England for discussions concerning the geodetic data. We are grateful to R. McCaffrey and G. Abers for allowing us to use their waveform inversion program. TT thanks Turkish Ministry of Higher Education for a scholarship, and JAJ thanks the Dean of the School of Earth Sciences, Stanford University, for support while this work was completed. This work was partly supported by NERC. Cambridge Earth Sciences contribution no. 1785.

REFERENCES

Ambraseys, N. N., 1970. Some characteristic features of the Anatolian fault zone, *Tectonophysics*, **9**, 143–165.

Ambraseys, N. N. & Zatopek, A., 1969. The Mudurnu Valley, West Anatolia, Turkey, earthquake of 22 July 1967, *Bull. seism. Soc. Am.*, **2**, 521–589.

Ambraseys, N. N. & Finkel, C. F., 1987. The Saros–Marmara earthquake of 9 August 1912, *Earthquake Eng. Struct. Dyn.*, **15**, 189–211.

Ambraseys, N. N. & Jackson, J. A., 1990. Seismicity and associated strain of central Greece between 1890 and 1988, *Geophys. J. Int.*, **101**, 663–708.

Anderson, H. J. & Jackson, J. A., 1987. Active tectonics of the Adriatic region, *Geophys. J. R. astr. Soc.*, **91**, 937–983.

Angelier, J., Lyberis, N., Le Pichon, X. & Huchon, P., 1982. The tectonic development of the Hellenic Trench and Sea of Crete: a synthesis, *Tectonophysics*, **86**, 159–196.

Aubouin, J., 1965. *Geosynclines*, Elsevier, Amsterdam.

Barka, A. A. & Kadinsky-Cade, K., 1988. Strike–slip fault geometry in Turkey and its influence on Earthquake activity, *Tectonics*, **3**, 663–684.

Bezzeghoud, M., Deschamps, A. & Madariaga, R., 1986. Broad-band modelling of the Corinth, Greece earthquakes of February and March 1981, *Annales Geophysicae*, **4**, 295–304.

Biju-Duval, B., Letouzey, J. & Sancho, J., 1972. Nouvelles données de sismique réflection précisant la structure du bassin Méditerranean oriental et du Nord de la Mer Egée (abstract), *4th Aegean Symposium*, Hannover.

Billiris, H. *et al.*, 1991. Geodetic determination of the strain of Greece in the interval 1900 to 1988, *Nature*, **350**, 124–129.

Briqueu, L., Javoy, M., Lancelot, J. R. & Tatsumoto, M., 1986. Isotope geochemistry of recent magmatism in the Aegean arc: Sr, Nd, Hf, and O isotopic ratios in the lavas of Milos and Santorini—geodynamic implications, *Earth planet. Sci. Lett.*, **80**, 41–54.

Brooks, M. & Ferentinos, G., 1980. Structure and evolution of the Sporadhes basin of the north Aegean trough, Northern Aegean sea, *Tectonophysics*, **68**, 15–30.

Brooks, M. & Ferentinos, G., 1984. Tectonics and Sedimentation in the Gulf of Corinth and the Zakynthos and Kefallina channels, Western Greece, *Tectonophysics*, **101**, 25–54.

Brooks, M. & Kiriakidis, L., 1986. Subsidence of the North Aegean Trough: an alternative view, *J. geol. Soc. Lond.*, **143**, 23–7.

Brooks, M. & Kiriakidis, L., 1987. Reply to comments of Le Pichon *et al.*, (1987), *J. geol. Soc. Lond.*, **144**, 350–351.

Brunn, J. H., 1976. L'arc concave zagro-taurique et les arcs convexes taurique et égé: collision et arc induits, *Bull. Soc. géol. France*, **18**, 553–567.

Burke, W. F. & Uğurtaş, G., 1974. Seismic interpretation of Thrace basin, *Proc. Second. Petroleum Congress of Turkey*, p. 229–249, TPAO internal report, Ankara.

Carey, E., 1979. Recherche des directions principales de contraintes associées au jeu d'une population de failles, *Rev. Géol. Dyn. Géogr. Phys.*, **XXI**, 57–65.

Collier, R. E., 1988. Sedimentary facies evolution in continental fault-bounded basins formed by crustal extension: the Corinth basin, Greece, *PhD thesis*, University of Leeds.

Collier, R. E., 1990. Eustatic and tectonic controls upon Quaternary coastal sedimentation in the Corinth Basin, Greece, *J. geol. Soc. Lond.*, **147**, 301–314.

Crampin, S. & Evans, R., 1986. Neotectonics of the Marmara Sea region of Turkey, *J. geol. Soc. Lond.*, **143**, 343–348.

Dewey, J. F. & Şengör, A. M. C., 1979. Aegean and surrounding regions: complex multiplate and continuum tectonics in a convergent zone, *Bull. geol. Soc. Am.*, **90**, 84–92.

Dewey, J. F., Hempton, M. R., Kidd, W. S. F., Şaroğlu, F., Şengör, A. M. C., 1986. Shortening of continental lithosphere: the neotectonics of Eastern Anatolia—a young collision zone, in *Collision Tectonics*, Spec. Publ. geol. Soc. London, vol. 19, pp. 3–36, eds Coward, M. P. & Ries, A. C., Blackwell Scientific Publications, Oxford.

Doutsos, T. & Piper, D. J. W., 1990. Listric faulting,

sedimentation, and morphological evolution of the Quaternary eastern Corinth rifts, Greece: first stages of continental rifting, *Geol. Soc. Am. Bull.*, **102,** 812–829.

Drakopoulos, J. C. & Ekonomides, A. C., 1972. Aftershocks of February 19, 1968. Earthquake in Northern Aegean Sea and Related Problems, *Pageoph.*, **95,** 100–115.

Ekström, G. A. & Dziewonski, A., 1988. Evidence of bias in the estimation of earthquake size, *Nature,* 319–323.

Ekström, G. A. & England, P. C., 1989. Seismic strain rates in regions of distributed continental deformation, *J. geophys. Res.*, **94,** 10 231–10 257.

England, P. C., Houseman, G. A. & Sonder, L. J., 1985. Length scales for continental deformation in convergent, divergent and strike-slip environments: analytical and approximate solutions for a thin viscous sheet model, *J. geophys. Res.*, **90,** 3351–3357.

Eyidoğan, H. & Jackson, J. A., 1985. A seismological study of normal faulting in the Demirci, Alaşehir, and Gediz earthquakes of 1969–70 in western Turkey: implications for the nature and geometry of deformation in the continental crust, *Geophys. J. R. astr. Soc.*, **81,** 569–607.

Fredrich, J., McCaffrey, R. & Denham, D., 1988. Source parameters of seven large Australian earthquakes determined by body waveform inversion, *Geophys. J.*, **95,** 1–13.

Futterman, W. I., 1962. Dispersive body waves, *J. geophys. Res.*, **67,** 5279–5291.

Gibbs, A., 1984. Structural evolution of extensional basin margins, *J. geol. Soc. Lond.*, **141,** 609–620.

Ginzburg, A., Makris, J. & Hirschleber, H., 1987. Geophysical investigations in the North Aegean Trough, *Annales Geophysicae,* **5B,** 167–174.

Higgs, B., 1988. Syn-sedimentary structural controls on basin formation in the Gulf of Corinth, Greece, *Basin Res.*, **1,** 155–165.

Innocenti, F., Manetti, P., Peccerillo, A. & Poli, G., 1979. Inner arc volcanism in NW Aegean Arc: geochemical and geochronological data, *N. Jb. Miner. Monats.*, 145–158.

Innocenti, F., Manetti, P., Mazzuoli, R., Pasquare, G. & Villari, L., 1982. Anatolia and North-Western Iran, in *Andesites,* pp. 327–349, ed. Thorpe, R. S., John Wiley & Sons, New York.

IOC–UNESCO, 1981. *International bathymetric chart of the Mediterranean,* Scale 1:1,000,000, 10 sheets, Ministry of Defence, Leningrad.

Jackson, J. A. & Fitch, T. J., 1979. Seismotectonic implications of relocated aftershock sequences in Iran and Turkey, *Geophys. J. R. astr. Soc.*, **57,** 209–229.

Jackson, J. A. & McKenzie, D., 1983. The geometrical evolution of normal fault systems, *J. Struct. Geol.*, **5,** 471–482.

Jackson, J. A. & McKenzie, D., 1984. Active tectonics of the Alpine–Himalayan Belt between western Turkey and Pakistan, *Geophys. J. R. astr. Soc.*, **77,** 185–264.

Jackson, J. A. & McKenzie, D., 1988a. The relationship between plate motions and seismic moment tensors, and the rates of active deformation in the Mediterranean and the Middle East, *Geophys. J.*, **93,** 45–73.

Jackson, J. A. & McKenzie, D., 1988b. Rates of active deformation in the Aegean Sea and surrounding areas, *Basin Res.*, **1,** 121–128.

Jackson, J. A. & White, N. J., 1989. Normal faulting in the upper continental crust: observations from regions of active extension, *J. Struct. Geol.*, **11,** 15–36.

Jackson, J. A. & Molnar, P., 1990. Active faulting and block rotations in the western Transverse ranges, California, *J. geophys. Res.*, **95,** 22 073–22 087.

Jackson, J. A., King, G. & Vita-Finzi, C., 1982b. The neotectonics of the Aegean: an alternative view, *Earth planet. Sci. Lett.*, **61,** 303–318.

Jackson, J. A., Gagnepain, J., Houseman, G., King, G. C. P., Papadimitriou, P., Soufleris, C. & Vireux, J., 1982a. Seismicity, normal faulting, and the geomorphological development of the Gulf of Corinth (Greece): the Corinth earthquakes of February & March 1981, *Earth planet. Sci. Lett.*, **57,** 377–397.

Karnik, V., 1967. *Seismicity of the European area/I,* Reidel, Dordrecht.

Karnik, V., 1970. *Seismicity of the European area/II,* Reidel, Dordrecht.

Keraudren, B. & Sorel, D., 1987. The terraces of Corinth (Greece): a detailed record of eustatic variations of the sea level during the last 500,000 years, *Mar. Geol.*, **77,** 99–107.

Ketin, I., 1948. Uber die tektonisch-mechanischen Folgerungen aus den grossen anatolischen Erdbeden des letzten Dezenniums, *Geol. Rundsch.*, **36,** 77–83.

Ketin, I., 1966. 6 Ekim 1964 Manyas depremi enasinda zeminde meydana gelen tansiyon çatlaklari, *Türkiye Jeoloji Kurumu Bülteni,* **10,** 1–2.

Ketin, I. & Roesli, F., 1954. Makroseismische Untersuchungen über das nordwestanatolische Beben wom 18. März 1953, *Ecloque Geologicae Helvetiae,* **46,** 187–208.

Kim, W.-Y., Kulhánek, O. & Meyer, K., 1984. Source processes of the 1981 Gulf of Corinth earthquake sequence from body-wave analysis, *Bull. seism. Soc. Am.*, **74,** 459–477.

King, G. C. P., Ouyang, Z. K., Papadimitriou, P., Deschamps, A., Gagnepain, J., Houseman, G., Jackson, J. A., Soufleris, C. & Virieux, J., 1985. The evolution of the Gulf of Corinth (Greece): an aftershock study of the 1981 earthquakes, *Geophys. J. R. astr. Soc.*, **80,** 677–693.

Kissel, C. & Laj, C., 1988. The Tertiary geodynamical evolution of the Aegean arc: a paleomagnetic reconstruction, *Tectonophysics,* **146,** 183–201.

Kissel, C., Laj, C. & Mazaud, A., 1986. First paleomagnetic results from Neogene formations in Evia, Skyros, and the Volos region, and the deformation of Central Aegean, *Geophys. Res. Lett.*, **13,** 1446–1449.

Kissel, C., Laj, C., Poisson, A. & Simeakis, K., 1989. A pattern of block rotations in central Aegea, in *Paleomagnetic Rotations and Continental Deformation,* pp. 115–129, eds Kissel, C. & Laj, C., Kluwer Academic Publishers, Dordrecht.

Kojumgdieva, E., 1987. Evolution géodynamique du bassin Egéen pendant le Miocene supérieur et ses rélations a la Paratethys orientale, *Geologica Balcanica,* **17,** 3–14.

Kondopoulou, D. & Lauer, J. P., 1984. Paleomagnetic data on the Northern part and a tentative overview on Neogene rotations in the Aegean Zone, *The Geological Evolution of the Eastern Mediterranean,* Vol. 17, pp. 681–686, Spec. Publ. Geol. Soc. London.

Kondopoulou, D. & Westphal, M., 1986. Paleomagnetism of the Tertiary intrusives from Chalkidiki (Northern Greece), *J. Geophys.*, **59,** 62–66.

Laj, C., Jamet, M., Sorel, D. & Valente, J. P., 1982. First paleomagnetic results from Mio-Pliocene series of the Hellenic sedimentary arc, Geodynamics of the Hellenic Arc and Trench, *Tectonophysics,* **86,** 45–67.

Lalechos, N. & Savoyat, E., 1979. La sédimentation Néogéne dans le Fossé Nord Egéen, *6th Colloquium on the Geology of the Aegean region,* vol. 2, pp. 591–603.

Lamb, S. H., 1987. A model for tectonic rotations about a vertical axis, *Earth planet. Sci. Lett.*, **84,** 75–86.

Le Pichon, X., 1982. Land-locked oceanic basins and continental collision: the eastern Mediterranean as a case example, in *Mountain Building Processes,* pp. 201–211, ed. Hsu, K., Academic Press, New York.

Le Pichon, X. & Angelier, J., 1979. The Hellenic arc and trench system: a key to the evolution of the Eastern Mediterranean area, *Tectonophysics,* **60,** 1–42.

Le Pichon, X. & Angelier, J., 1981. The Aegean Sea, *Phil. Trans. R. Soc. Lond.*, A, **300,** 357–372.

Le Pichon, X., Lybéris, N. & Alvarez, F., 1984. Subsidence history of the North Aegean trough, in *Geological Evolution of the*

Eastern Mediterranean, Spec. Publ. Geol. Soc. Lond., vol. 17, pp. 727–41, eds Dixon, J. E. & Robertson, A. H. F., Blackwell Scientific Publications, Oxford.

Le Pichon, X., Lybéris, N. & Alvarez, F., 1987. Discussion on the subsidence of the North Aegean Trough: an alternative view, *J. geol. Soc. Lond.,* **144,** 349–351.

Le Pichon, X. *et al.,* 1982a. Subduction in the Hellenic Trench: probable role of a thick evaporitic layer based on Seabeam and submerisble studies, in *Trench–Forearc Geology,* Spec. Publ. Geol. Soc. Lond., vol. 10, pp. 319–333, ed. Leggett, J. K., Blackwell Scientific Publications, Oxford.

Le Pichon, X., Lybéris, N., Angelier, J. & Renard, V., 1982b. Strain distribution over the East Mediterranean Ridge: A synthesis incorporating new Sea-Beam data, *Tectonophysics,* **86,** 243–274.

Liotier, Y., 1989. Modelisation des Ondes de Volume ses Seismes de L'arc Egéen, *Formation de 3^e Cycle,* UFR de Mechanique, Universite Joseph Fourier de Grenoble 1.

Lybéris, N., 1984. Tectonic evolution of the North Aegean trough, in *Geological Evolution of the Eastern Mediterranean,* Spec. Publ. Geol. Soc. Lond., vol. 17, pp. 709–725, eds Dixon, J. E. & Robertson, A. H. F., Blackwell Scientific Publications, Oxford.

Lybéris, N. & Deschamps, A., 1982. Sismo-tectonique du fossé Nord-Egéen: relations avec la faille Nord-Anatolienne, *C.R. Acad. Sci. Paris,* **295,** Sér. 2, 625–628.

Lyon-Caen, H. *et al.,* 1988. The 1986 Kalamata (S. Peloponessos) earthquake: Detailed study of a normal fault and tectonic implications, *J. geophys. Res.,* **93,** 14 967–15 000.

Main, I. G. & Burton, P. W., 1989. Seismotectonics and the earthquake frequency–magnitude distribution in the Aegean area, *Geophys. J. R. astr. Soc.,* **98,** 575–586.

Makris, J. & Stobbe, C., 1984. Physical properties and state of the crust and upper mantle of the Eastern Mediterranean sea deduced from geophysical data, *Mar. Geol.,* **55,** 347–363.

Mariolakos, I., Paparikolaou, D., Symeonidis, N., Lekkas, S., Karotsieris, Z. & Sideris, C., 1982. The deformation of the area around the eastern Korinthian Gulf affected by the earthquakes of February–March 1981, *Int. Symposium on the Hellenic arc and Trench (HEAT),* Athens, pp. 400–420.

McCaffrey, R., 1988. Active tectonics of the Eastern Sunda and Banda Arcs, *J. geophys. Res.,* **93,** 15 163–15 182.

McCaffrey, R. & Nábělek, J., 1987. Earthquakes, gravity, and the origin of the Bali Basin: an example of a nascent continental fold-and-thrust belt, *J. geophys. Res.,* **92,** 441–460.

McCaffrey, R. & Abers, G., 1988. SYN3: A program for inversion of teleseismic body wave forms on microcomputers, *Air Force Geophysics Laboratory Technical Report,* AFGL-TR-88-0099, Hanscomb Air Force Base, MA.

McKenzie, D., 1972. Active tectonics of the Mediterranean Region, *Geophys. J. R. astr. Soc.,* **30,** 109–185.

McKenzie, D., 1978. Active tectonics of the Alpine–Himalayan belt: the Aegean Sea and surrounding regions, *Geophys. J. R. astr. Soc.,* **55,** 217–254.

McKenzie, D. & Jackson, J. A., 1983. The relationship between strain rates, crustal thickening, paleomagnetism, finite strain and fault movements within a deforming zone, *Earth planet. Sci. Lett.,* **65,** 182–202.

McKenzie, D. & Jackson, J. A., 1986. A block model of distributed deformation by faulting, *J. geol. Soc. Lond.,* **143,** 249–253.

Mercier, J. L. & Carey-Gailhardis, E., 1989. Regional state of stress and characteristic fault kinematic instabilities shown by aftershock sequences: the 1978 Thessaloniki (Greece) and 1980 Campania-Lucania (Italy) earthquakes as examples, *Earth planet. Sci. Lett.,* **92,** 247–264.

Mercier, J. L., Sorel, D., Vergely, P. & Simeakis, K., 1989. Extensional tectonic regimes in the Aegean basins during the Cenozoic, *Basin Res.,* **2,** 49–71.

Mercier, J. L., Carey, E., Philip, H. R. & Sorel, D., 1976. La néotectonique plio-quaternaire de l'arc egéen externe et de la Mer egéen et ses relations avec séismicité, *Bull. Soc. géol. France,* **18,** 159–176.

Mercier, J. L., Mouyaris, N., Simeakis, C., Roundoyannis, T. & Angelidhis, C., 1979a. Intraplate deformation: a quantitative study of the faults activated by the 1978 Thessaloniki earthquakes, *Nature,* **278,** 45–48.

Mercier, J. L., Delibassis, N., Gautier, A., Jarrige, J. J., Lemille, F., Philip, H., Sebrier, M. & Sorel, D., 1979b. La néotectonique de l'Arc Egéen, *Rev. Géol. Dyn. Géog. Phys.,* **21,** 67–92.

Mercier, J. L., Vergeley, P., Simeakis, C., Kissel, C. & Laj, C., 1991. The continuation of the North Anatolian dextral strike–slip fault into the oblique fault zone of the North Aegean Trough (W. Turkey and N. Greece): timing, tectonic regimes, fault kinematics and rotations, *Tectonics,* submitted.

Molnar, P. & Lyon-Caen, H., 1989. Fault plane solutions of earthquakes and active tectonics of the Tibetan Plateau and its margins, *Geophys. J. Int.,* **99,** 123–153.

Nábělek, J. L., 1984. Determinations of earthquake source parameters from inversion of body waves, *PhD thesis,* MIT, Cambridge, MA.

Nábělek, J. L., 1985. Geometry and mechanism of faulting of the 1980 El Asnam, Algeria, earthquake from inversion of teleseismic body waves and comparison with field observations, *J. geophys. Res.,* **90,** 12 713–12 728.

Nelson, M. R., McCaffrey, R. & Molnar, P., 1987. Source parameters for 11 earthquakes in the Tien Shan, Central Asia, determined by P and SH waveform inversion, *J. geophys. Res.,* **92,** 12 629–12 648.

Nicholson, C., Seeber, L., Williams, P. & Sykes, L., 1986. Seismic evidence for conjugate slip and block rotation within the San Andreas fault system, southern California, *Tectonics,* **5,** 629–648.

Öcal, N., Uçar, S. B. & Taner, D., 1968. Manyas–Karacabey Depremi 6 Ekim 1964, *İstanbul Kandilli Rasathanesi,* Sismoloji Yayınları, vol. 11, Kandilli Observatory Internal Report.

Papazachos, B., Panagiotopoulos, D., Tsapanos, T., Mountrakis, D. & Dimopoulos, G., 1983. A study of the 1980 summer seismic sequence in the Magnesia region of Central Greece, *Geophys. J. R. astr. Soc.,* **75,** 155–168.

Perissoratis, C., Mitropoulos, D. & Angelopoulos, I., 1986. Marine geological research at the E. Korinthiakos Gulf, *Special issue of Geology and Geophysical Research,* pp. 381–401, Institute of Geology and Mineral exploration, Athens.

Philip, H., Cisternas, A., Gvishiani, A. & Gorshkov, A., 1989. The Caucasus: an actual example of the initial stages of continental collision, *Tectonophysics,* **161,** 1–21.

Richens, W. D., Pechmann, J. C., Smith, R. B., Langer, C. J., Goter, S. K., Zollweg, J. E. & King, J. J., 1987. The Borash Peak, Idaho, earthquake and its aftershocks, *Bull. seism. Soc. Am.,* **77,** 694.

Richter, C. F., 1958. *Elementary Seismology,* Freeman, San Francisco.

Roberts, S. & Jackson, J. A., 1991. Active normal faulting in central Greece: An overview, in *The Geometry of Normal Faults,* Spec. Publ. Geol. Soc. Lond., vol. 56, pp. 125–142, eds Roberts, A. M., Yielding, G. & Freeman, B., Blackwell Scientific Publications, Oxford.

Rosendahl, B. R., Reynolds, D. J., Lorber, P. M., Burgess, C. F., McGill, J., Scott, D., Lambiase, J. J. & Derken, S. J., 1986. Structural expressions of rifting: lessons from Lake Tanganyika, Africa, in *Sedimentation in the African Rifts,* Spec. Publ. Geol. Soc. Lond., vol. 25, pp. 29–43, eds Frostick L. E., Renaut, R. W., Reid, I. & Tiercelin, J. J., Blackwell Scientific Publications, Oxford.

Şaroğluo, F., Emre, Ö. & Boray, A., 1987. *Türkiye Diri Fay Haritası,* Maden Tetkik ve Arama Enstitüsü, Ankara, Turkey.

Sebrier, M., 1977. Tectonique récente d'une transversale a l'arc

egéen: le Golfe de Corinthe et ses régions périphériques, *Thesis,* Université de Paris-Sud, Orsay.

Sellers, P. C. & Cross, P. A., 1989. 1986 and 1987 Wegener–Medlas baselines determined using the Pseudo-Short Arc Technique, in *Proceedings Int. Conf. WEGENER-MEDLAS Project,* Scheviningen, 1989.

Şengör, A. M. C., Görür, N. & Şaroğlu, F., 1985. Strike slip faulting and related basin formation in zones of tectonic escape: Turkey as a case study, in *Strike Slip Deformation, Basin Formation, and Sedimentation,* no. 37, pp. 227–264, Society of Economic Paleontologists and Mineralogists, Tulsa, OK.

Şengör, A. M. C., 1987. Cross-faults and differential stretching of hanging walls in regions of low-angle normal faulting: examples from western Turkey, in *Continental Extensional Tectonics,* Spec. Publ. Geol. Soc. Lond., pp. 575–589, eds Dewey, M. P. & Hancock, P. L., Blackwell Scientific Publications, Oxford.

Sonder, L. J. & England, P. C., 1989. Effects of temperature-dependent rheology on large-scale continental extension, *J. geophys. Res.*, **94,** 7603–7609.

Sorel, D., 1989. L'evolution structurale De La Grece Nord-Occidentale Depuis Le Miocene, dans Le Cadre Geodynamique de L'arc Egeen, *PhD thesis,* Centre D'Orsay, Universite de Paris-Sud.

Soufleris, C., 1980. The Thessaloniki (N. Greece) 1978 earthquake sequence, *PhD thesis,* University of Cambridge, UK.

Soufleris, C. & Stewart, G. S., 1981. A source study of the Thessaloniki (northern Greece), 1978 earthquake sequence, *Geophys. J. R. astr. Soc.*, **67,** 343–358.

Soufleris, C., Jackson, J. A., King, G., Spencer, C. & Sholz, C., 1982. The 1978 earthquake sequence near Thessaloniki (N. Greece), *Geophys. J. R. astr. Soc.*, **68,** 429–458.

Stewart, G. S. & Kanamori, H., 1982. Complexity of rupture in large strike–slip earthquakes in Turkey, *Phys. Earth planet. Inter.*, **28,** 70–84.

Taymaz, T., Jackson, J. A., Westaway, R., 1990. Earthquake Mechanisms in the Hellenic Trench near Crete, *Geophys. J. Int.*, **102,** 695–731.

Vita Finzi, C. & King, G. C. P., 1985. The seismicity, geomorphology and structural evolution of the Corinth area of Greece, *Phil. Trans. R. Soc. Lond.*, A, **314,** 379–407.

Wdowinski, S., O'Connell, R. J. & England, P., 1989. A continuum model of continental deformation above subduction zones: application to the Andes and the Aegean, *J. geophys. Res.* **94,** 10 331–10 346.

Zachos, K., 1977. Oil possibilities in graben structures in the Hellenic area, in *Proc. VI Colloquium on the Geology of the Aegean region,* vol. 3, pp. 1191–1198, Inst. Geol. Mining Res., Athens.

APPENDIX A

This appendix contains the observed and synthetic seismograms for the earthquakes in this study that were not discussed individually in the main text. The first motion polarity observations for all the events we studied are shown in Fig. 4. For all the events in this appendix we carried out tests of the type summarized in Fig. 6, to estimate the uncertainties in strike, dip, rake and centroid depth. These uncertainties, together with the parameters of our minimum misfit solutions, are listed in Table 1. The uncertainties in depth estimates do not include the uncertainty related to the unknown average velocity above the source, which is likely to be no more than about ±2 km (see main text). The ISC locations and velocity structures of these events are given in Tables 1 and 3. The 1981 Gulf of Corinth earthquakes are discussed separately in Appendix B.

1963 September 18

The minimum misfit solution for this earthquake is shown in Fig. A1. The *P*- and *SH*-waveforms are simple at all azimuths and characteristic of normal faulting with a shallow focal depth. The number of available stations is not large, but the coverage of the focal sphere at all azimuths for both first motion and waveform data (especially *SH*-waves) enabled us to resolve the orientation of the nodal planes reasonably well. The first motion polarities require mostly normal faulting (Fig. 4a). Three compressional first motions plot just inside the dilatational quadrant of the minimum misfit solution. Two of them (ATU, IST) are for close stations whose ray paths are uncertain. The third (UME) is very close to the NE dipping nodal plane, and within our uncertainty in dip of this plane (Table 1). We suspect that the gain at NDI was in fact 3000, and not 1500, as marked on the WWSSN film chip. This suspicion comes from comparing the *P*-wave amplitude at NDI with those at QUE and LAH, which are close to NDI on the focal sphere. In Fig. A1 we have corrected the gain at NDI and its seismograms have been plotted with this new gain, though this did not affect the inversion significantly because of the other stations at almost the same position on the focal sphere. This anomalous gain value at NDI was also reported by Taymaz *et al.* (1990). Our mechanism for this earthquake has a greater normal faulting component than that of Jackson & McKenzie (1984), which was based on first motions alone. Their NE-dipping plane was steeper, and with a more easterly strike, to accommodate the compressional first motions at IST and UME.

1964 October 6

The waveforms for this event are shown in Fig. A2. The source orientation is well constrained by first motion polarities (Fig. 4b), with which the minimum misfit solution is compatible. Although few *SH*-waveforms are available, the focal sphere is covered at all azimuths by *P*-waveforms. The seismograms at stations in the west contain complexities and later arrivals that are not seen at stations in the east. Their origin might be associated with rupture propagation or structural effects. Our attempts to match the later arrivals by separate subevents were unsuccessful. The surface faulting in this event was not easy to interpret. It was mapped by Ketin (1966) who believed the surface features resulted from right-lateral strike–slip motion on an east–west fault. Our fault plane solution shows dominantly normal faulting. The large observed amplitudes of the *P*-waveform at CMC ($\Delta = 69°$) are not matched properly. We suspect this is because of an incorrect instrument gain reported on the WWSSN film chip, but we could find no direct evidence to confirm this, and have left it unchanged, though we weighted the station to zero. As in the event of 1963 September 18, it appeared that the gain at NDI should have been 3000 not 1500, and its seismograms have been plotted with this new gain in Fig. A2.

1965 March 9

This is our least satisfactory solution. In spite of the paucity of waveforms available for this event (Fig. A3), its focal parameters are well determined by first motion polarity

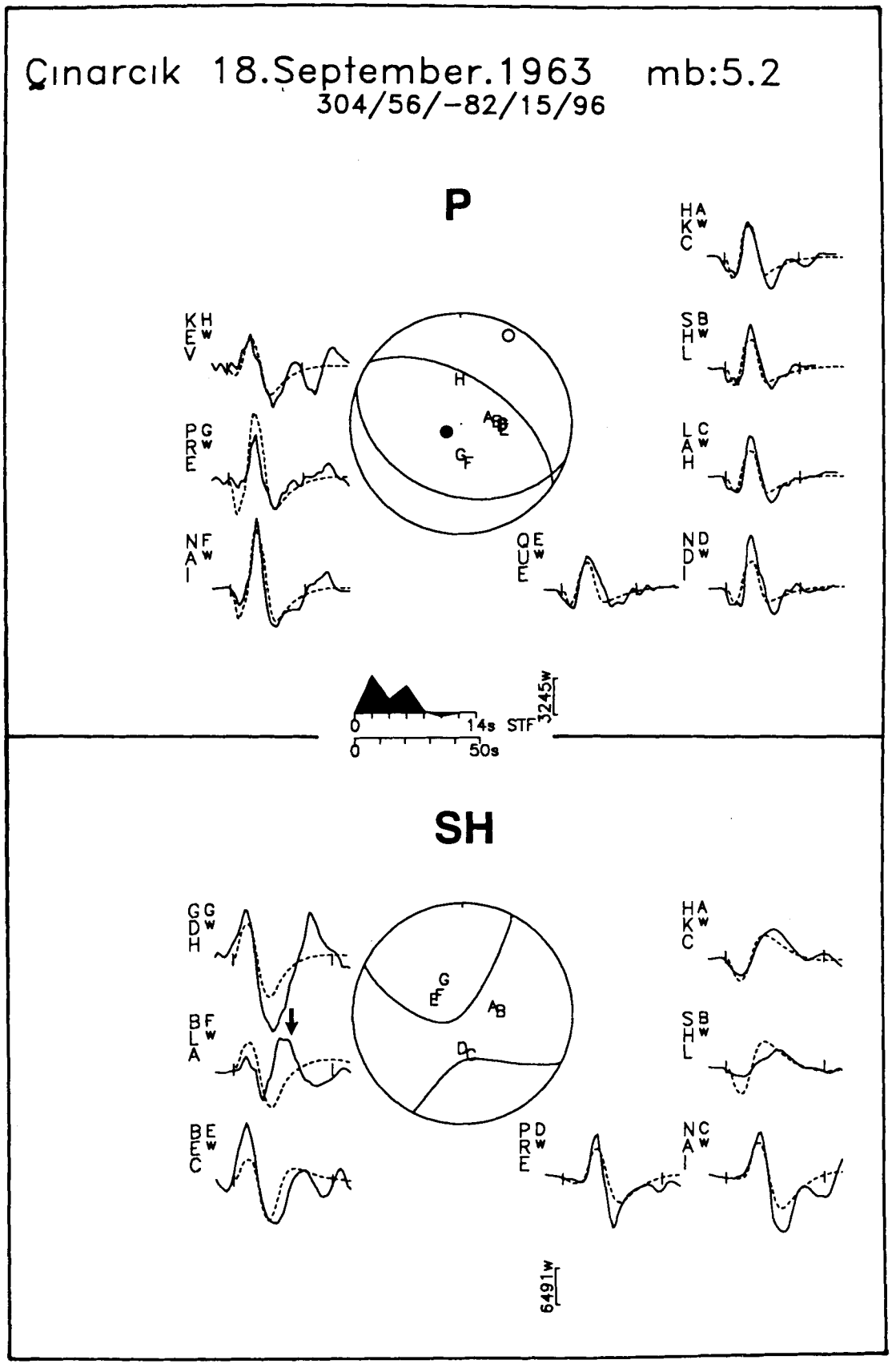

Figure A1. Minimum misfit solution for the earthquake of 1963 September 18. The display convention is the same as in Fig. 5.

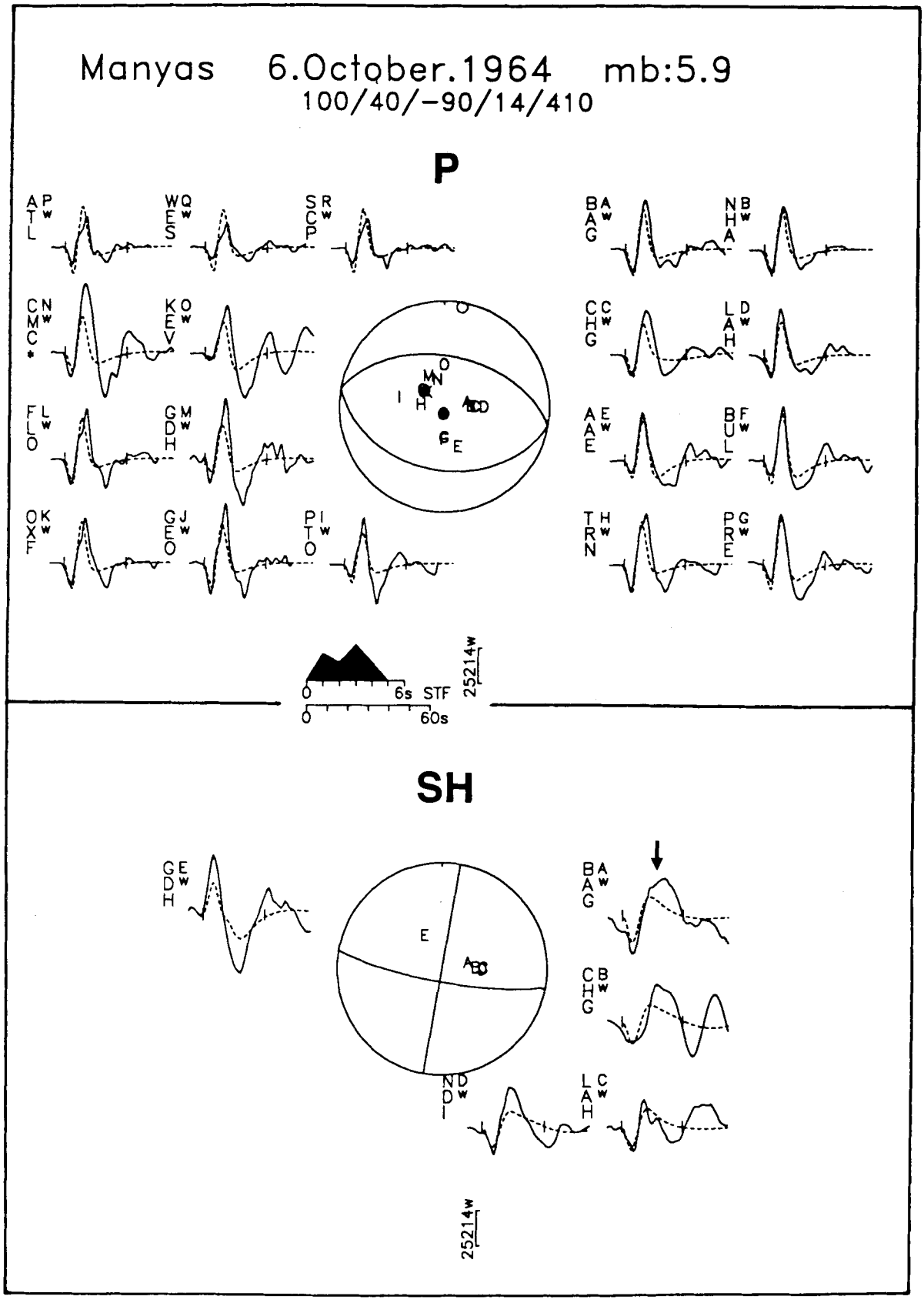

Figure A2. Minimum misfit solution for the earthquake of 1964 October 6. The display convention is the same as in Fig. 5. The asterisk under the station code for CMC indicates that this station had zero weight in the solution.

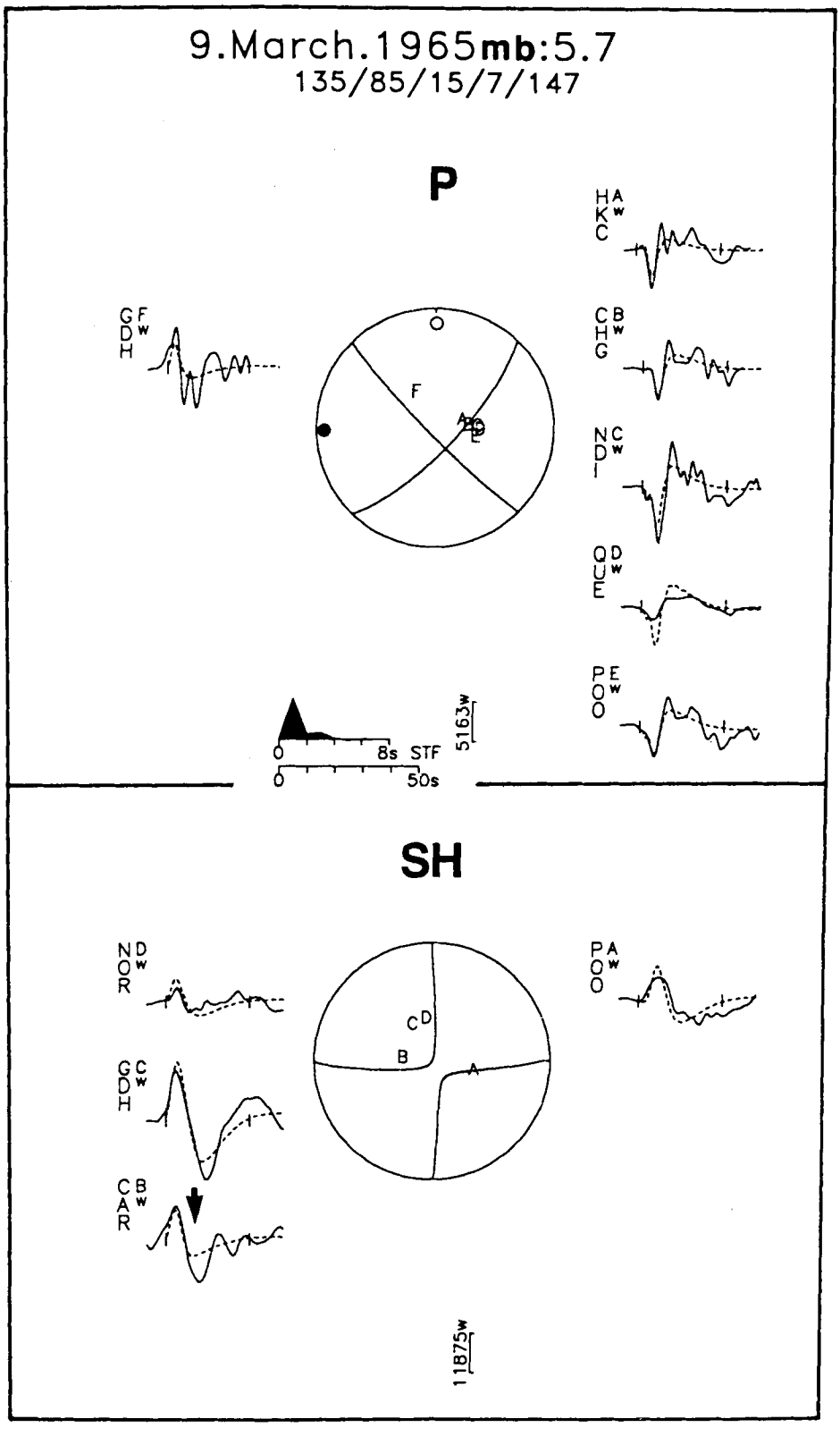

Figure A3. Minimum misfit solution for the earthquake of 1965 March 9. The display convention is the same as in Fig. 5.

readings (Fig. 4c), and by nodal onsets at eastern stations suggesting a relatively steep dip to a nodal plane dipping north-east. The waveforms for this event are clearly different from the two normal faulting events above. The later parts of the *P*-waveforms show complexities that we did not attempt to model, because of the poor station distribution. The strike and dip are well constrained by the nodal position of the *P*-waveforms at HKC, CHG, and NDI, and that of the *SH*-waveforms at POO, CAR, and NOR (Fig. A3).

1967 March 4

This event is discussed in the main text (Figs 5 and 6).

1967 July 22

This was the largest event in our study ($M_s = 7.1$) and was well recorded at all azimuths. Most of the *SH*-waveforms recorded for this event were clipped or too faint to digitize. Many of the *P*-waveforms are complex, and variable in shape even between neighbouring stations on the focal sphere (Fig. A4a).

This earthquake produced about 80 km of surface faulting on the North Anatolian Fault, with offsets of up to 2 m right-lateral strike-slip (Ambraseys & Zatopek 1969). First motion polarities (Fig. 4e) and our analysis of the early part of the waveform data, which is well constrained by the changes in *P* and *SH* polarities across nodal planes (Fig. A4a), indicate that most of the moment release in this earthquake was in an orientation compatible with the observed surface faulting. Furthermore, the moment of 7.5×10^{19} N m found in Fig. A4(a) can account for 2 m of slip on a fault 80 km long and 15 km deep, which is almost all the observed displacement. However, the obvious complexities in the waveform data suggest that the earthquake may have involved rupture in later subevents (see also Stewart & Kanamori 1982), which would not be unusual in an earthquake of this size. The most complex *P*-waveforms are those at stations closest to the nodal planes on the focal sphere, whereas large, relatively simple pulses are observed at, for example, GDH and KTG.

This earthquake occurred at the western end of the relatively simple, localized, part of the North Anatolian Fault system, where it starts to branch and become involved in the normal faulting farther west. There is evidence that the 1967 Mudurnu sequence involved faulting with orientations different from that in Fig. A4(a). Ambraseys & Zatopek (1969) report a decrease in *S–P* time of the aftershocks recorded at Istanbul (100 km to the west) as the sequence progressed, suggesting a westwards migration of activity into a region where an aftershock of $m_b = 5.6$ occurred on 1967 July 30 at the western end of the observed surface faulting. The waveforms of this aftershock were too small to model by our procedure, but first motions require normal faulting, with nodal planes striking roughly NNW (McKenzie 1972; Jackson & McKenzie 1984; Jackson & White 1989).

The most obvious candidate for a second subevent is the pulse observed at about 30 s after the *P* arrival at southern and eastern stations (PRE, BUL, AAE, NAI, SDB, WIN, KOD, POO) and possibly at NOR. A pulse with about the same delay after the *S* arrival is seen in the *SH*-waveforms at NOR and GDH. These are not well matched by a single event (Fig. A4a). We attempted to match them with a second subevent 30 s after the first.

We found that we could not do so with a strike-slip mechanism of the same orientation as in the first subevent, because the *P* polarities needed to be different at the southern stations. A mechanism for the second subevent which was similar to that of the first, but rotated 35° anticlockwise, produced a better fit for the later part of the *P*-waveforms at southern and eastern waveforms and to the *SH*-waveforms at NOR, GDH and KOD (Fig. A4b). However, it makes little difference at other stations, and its mechanism, if it really existed at all, is clearly not well resolved, though its moment must be small compared with that of the first subevent. There is no evidence for surface faulting of the orientation shown for the second subevent in Fig. A4(b). The ringing *P* seismograms at MAT and HKC are not seen at other stations and are presumably caused by a path effect. We are unconvinced that any of the waveform complexities represent substantial moment release after the first subevent, rather than path effects. If there was a second subevent within the first 40 s its moment was small compared with that of the first, which seems to have accounted for most of the surface faulting.

The polarities of the long-period horizontal components appear to have been reversed at PRE, and we corrected them in Fig. A4. This was noticed for another event, on 1965 April 9, by Taymaz *et al.* (1990).

1968 February 19

This was one of the largest events in our study $M_s = 7.0$, and was well recorded at all azimuths. It occured on the northern side of the Skyros basin, though its ISC location could be in error up to 50 km (Fig. 7). The source parameters of the minimum misfit solution Fig. A5(a) are compatible with all first motion *P* polarities, shown in Fig. 4(f). The *P* and *SH* pulses (mainly at the nodal stations) are complicated at all azimuths and characteristic of a large strike-slip faulting earthquakes.

Like the North Aegean Trough, the Skyros basin is also the site of strike-slip faulting, with right-lateral slip on NE to ENE trending nodal planes (Fig. 7). Drakopoulos & Ekonomides (1972) report almost 3000 aftershocks of this event with ($M_L \geq 2.1$) which occurred in a zone elongated 100 km NE, suggesting that the NE striking nodal plane was the fault plane.

The orientation of the mechanism responsible for the early part of the seismograms is well constrained by first motion polarities (Fig. 4f) and the change in polarities of *P*- and *SH*-waveforms. There is a hint of a secod subevent that might be responsible for the pulses observed 20–25 s after the *P* arrivals at eastern and southern stations; but there is no obvious necessity for this in the *SH*-waveforms. We were able to improve the fit of these *P*-waveforms by including a second subevent 16.5 s after the first, with a similar mechanism (Fig. A5b) but with the NE striking nodal plane dipping 70°SE rather than 70°NW. We are unconvinced that the waveforms require a second subevent. If it occurred, its mechanism is not well resolved, and most importantly, it involved a moment much smaller than that in the first subevent.

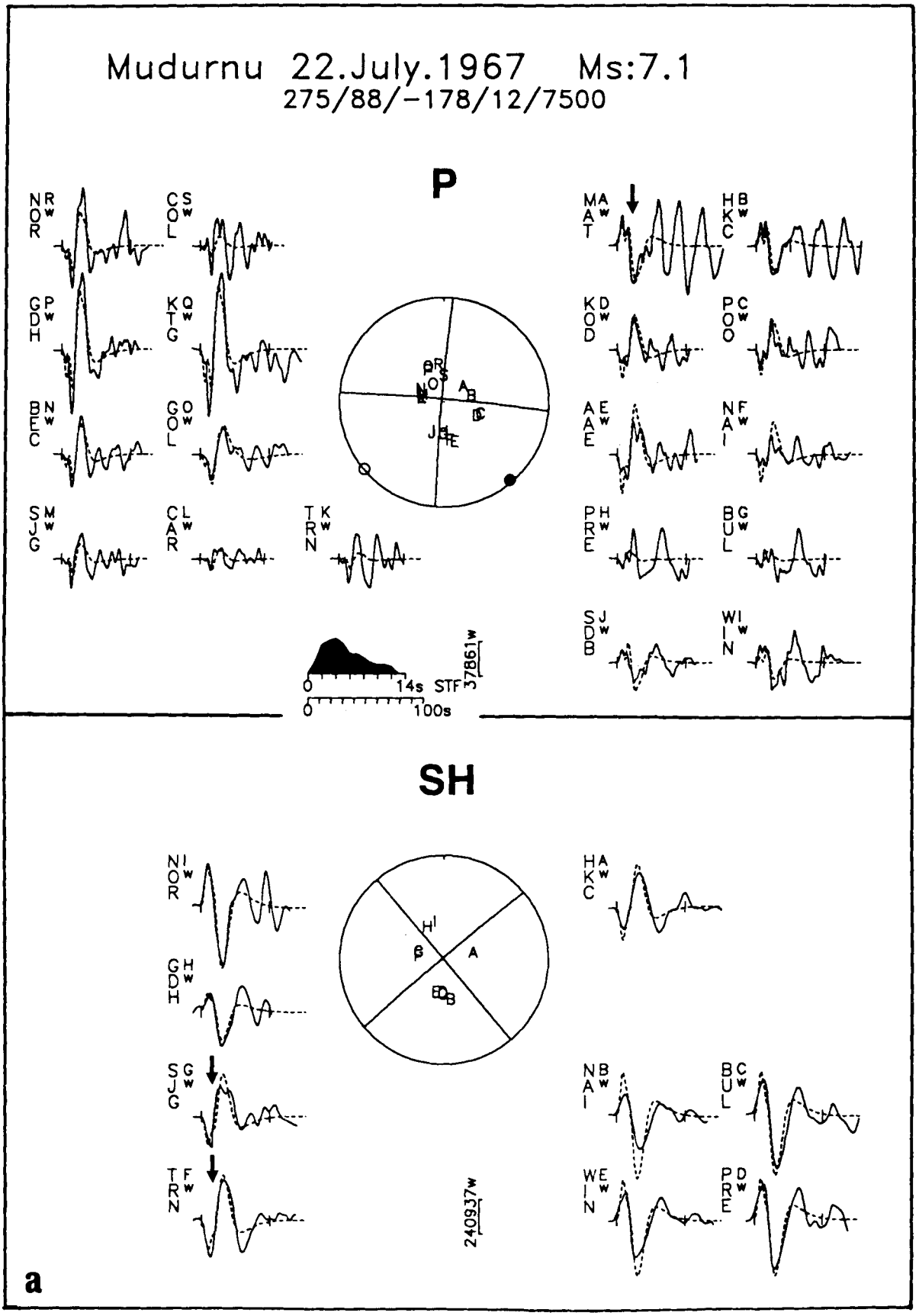

Figure A4. Minimum misfit solutions for the earthquakes of 1967 July 22. The display convention is the same as in Fig. 5. (a) The solution involving a single source. (b) The solution involving a second subevent 30.7 s after the first. The nodal planes and source time function of the postulated second subevent are shown by dashed lines.

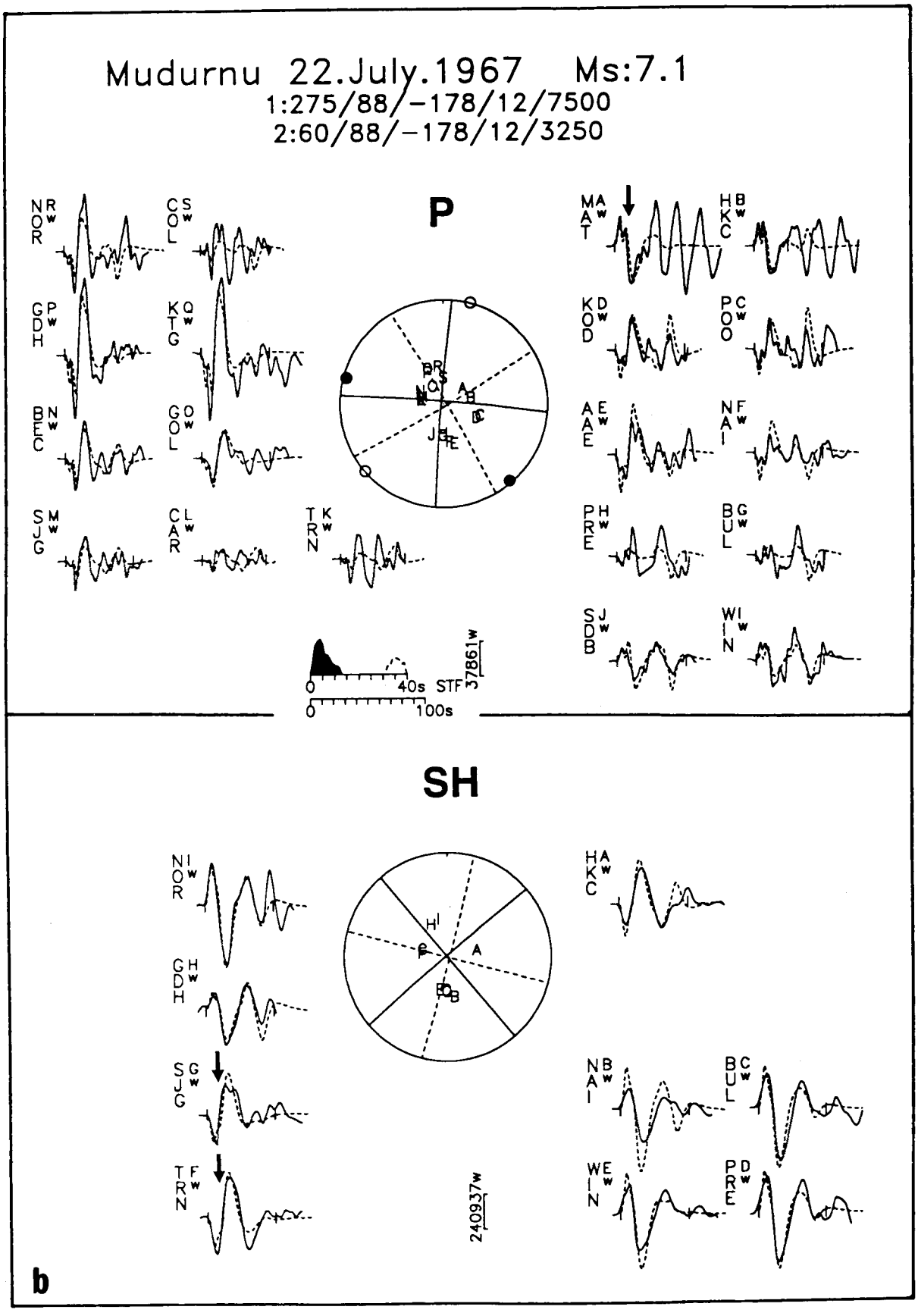

Figure A4. (*continued*)

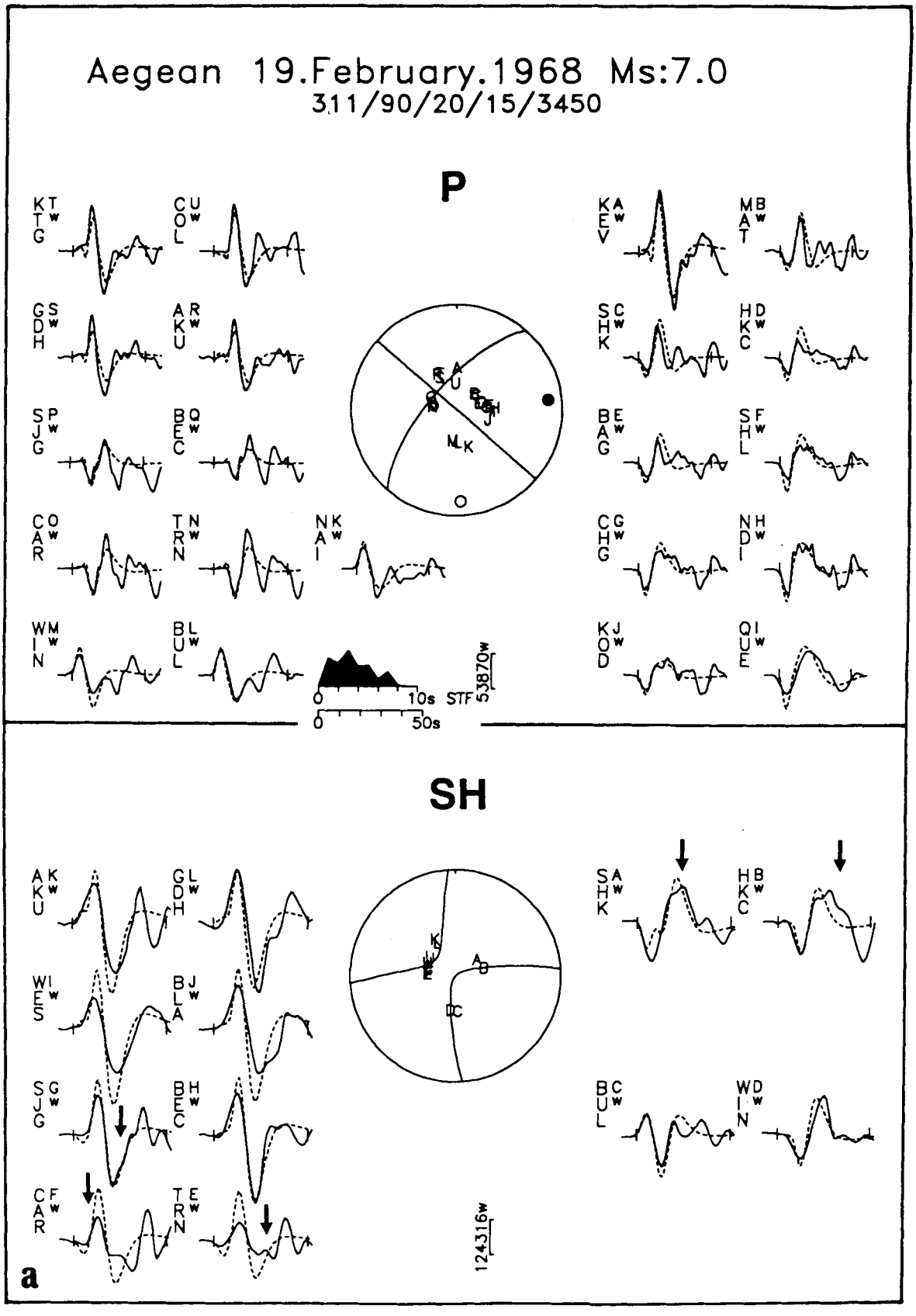

Figure A5. Minimum misfit solutions for the earthquake of 1968 February 19. The display convention is the same as in Fig. 5. (a) The solution involving a single source. (b) The solution involving a second subevent 16.5 s after the first. The nodal planes and source time function of the postulated second subevent are shown by dashed lines.

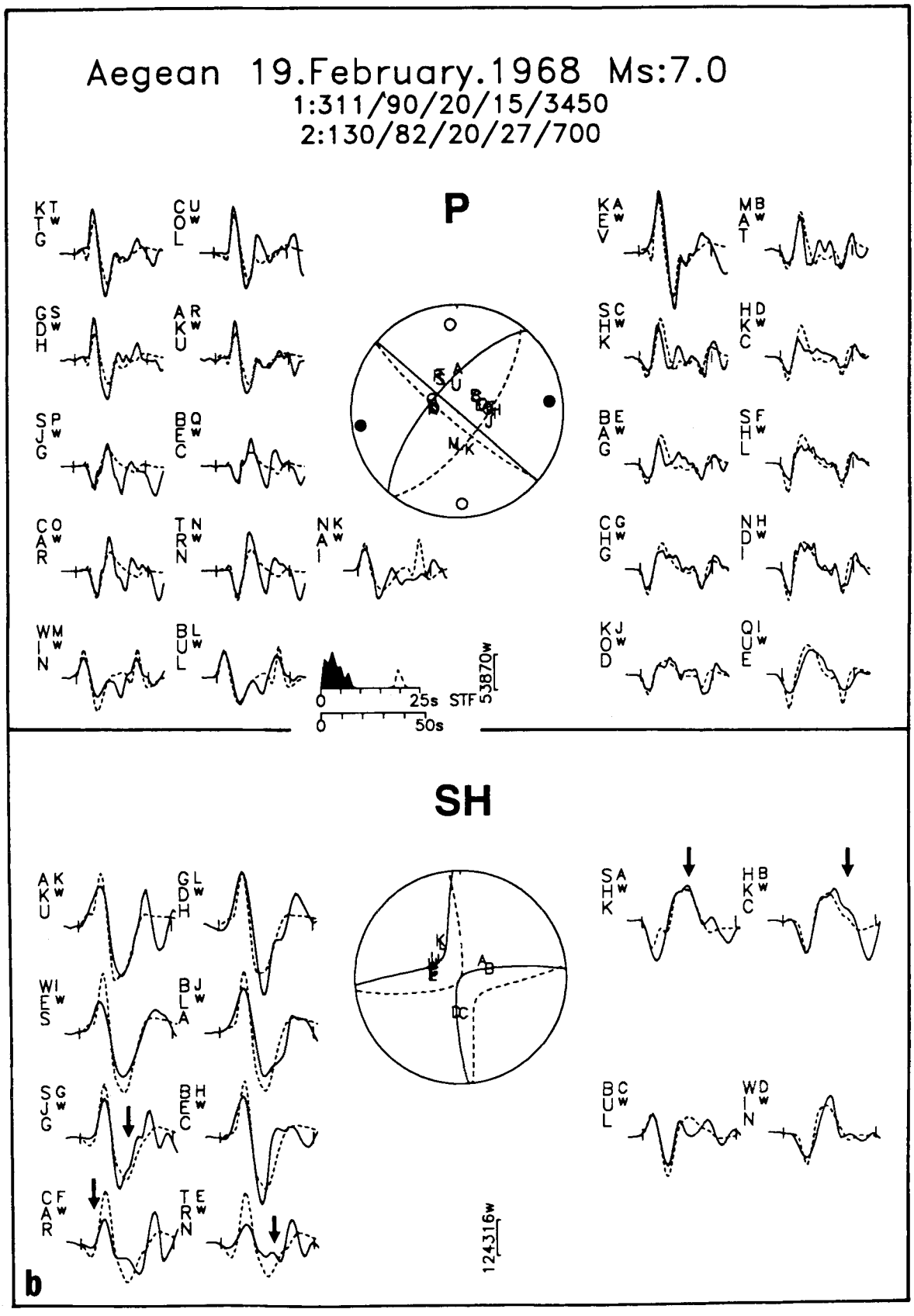

Figure A5. (*continued*)

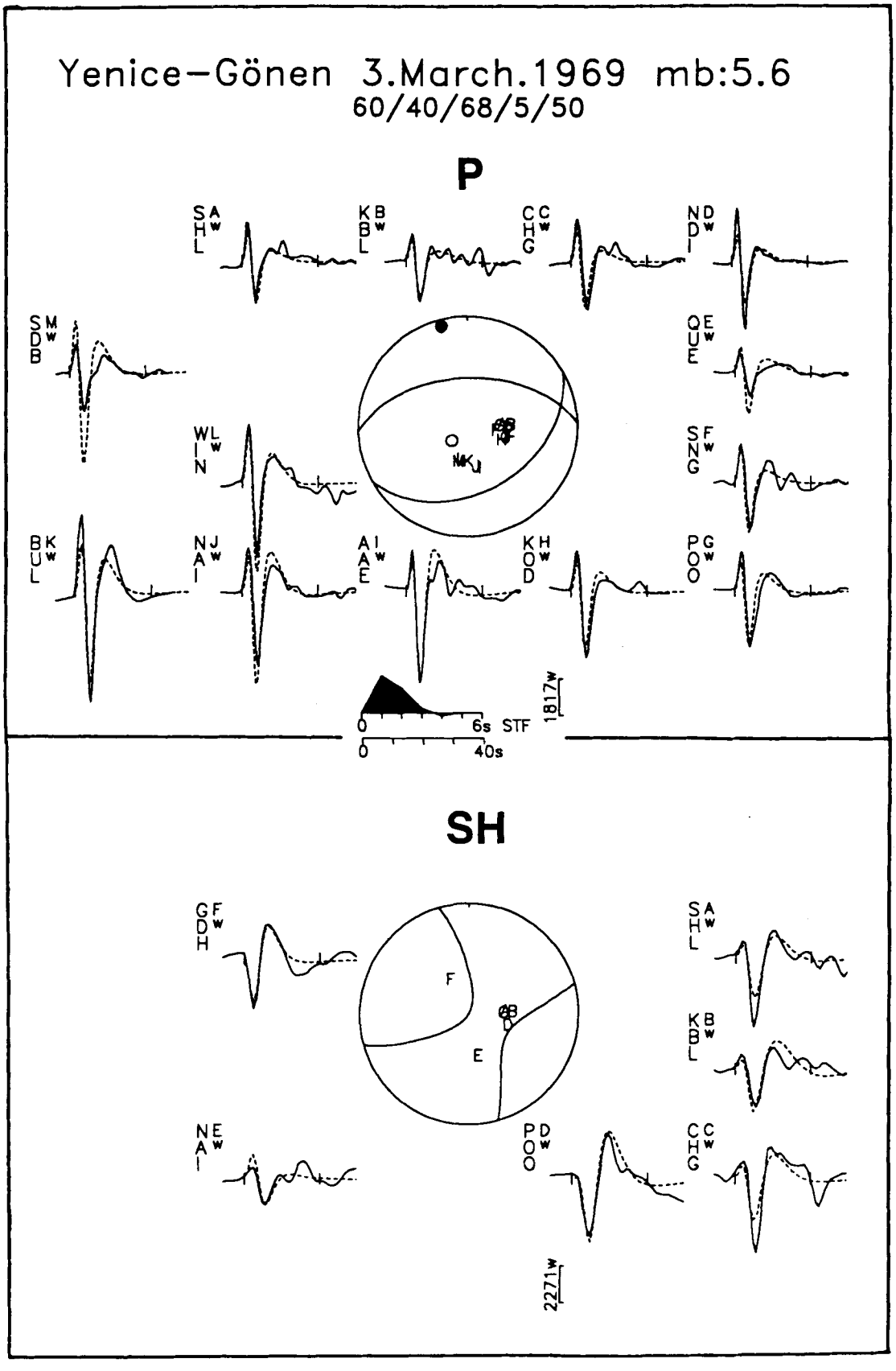

Figure A6. Minimum misfit solution for the earthquake of 1969 March 3. The display convention is the same as in Fig. 5.

1969 March 3

This was one of the smallest events ($M_o = 50 \times 10^{16}$ N m) in our study, and was reasonably well recorded at all azimuths. This is the anomalous solution with the high-angle reverse faulting (No. 7 in Fig. 7 and Table 1) in NW Turkey, which shows shortening in a roughly N–S direction.

Our solution for this event is well constrained by first motion polarities (Fig. 4g) and waveforms (Fig. A6), and is similar to that given by McKenzie (1972), which was based on first motions only. In spite of the absence of *P*-waveforms at European stations, *SH*-waveforms sample the focal sphere quite well and the mechanism is well constrained, particularly by the change in polarity of *SH*-waves between KBL and POO.

1975 March 27

The waveforms for this event are shown in Fig. A7. Its mechanism is well constrained by both waveforms and first motion polarities (Fig. 4h).

The azimuthal coverage of the focal sphere is good for both *P*- and *SH*-waveforms, and there is excellent coherence between waveforms from adjacent stations on the focal sphere. The large amplitudes observed in the later part of some *P*-waveforms show complexities that may be related to the rupture process of this event. We tried, unsuccessfully, to model these pulses with later subevents.

As with the events of 1963 September 18, and 1964 October 6, the seismograms at NDI are displayed with a gain of 3000, not the 1500 shows on the WWSSN records. It appeared that the polarities of the long-period horizontal instruments at NDI were reversed. Because the stations are weighted azimuthally, these changes to NDI made no difference to the inversion routine (Fig. A7).

1979 June 14

This earthquake was one of the smaller events in our study, and was well recorded at all azimuths. It occured on the SE coast of Lesbos, and its mechanism is constrained by both waveforms and first motion polarities (Figs 4i and A8).

The minimum misfit solution (Fig. A8) is consistent with motion on a fault bounding the deep basin off the SW coast of Lesbos. It was followed by an aftershock, $m_b = 4.9$, whose waveforms were too small to use in our inversion routine, but whose CMT solution (No. 3* in Fig. 8) reported by Ekström & England (1989) is similar to that of the main shock.

1981 December 19

The waveforms used in this event include long-period *P*- and *SH*-waves recorded by the WWSSN, and the digitally recorded seismograms of the DWWSSN, SRO, and ASRO networks. This was one of the largest events in our study ($M_o = 2.6 \times 10^{19}$ N m), and was very well recorded at all azimuths. The minimum misfit solution for this event is shown in Fig. A9. Because of its magnitude, some of the *SH*-waveforms recorded for this event were clipped or too faint to digitize. The nodal surfaces constrained by the inversion are compatible, within a few degrees, with virtually all first motion polarities (Fig. 4m).

The fit between observed and synthetic waveforms is good, except for the amplitudes of the *SH*-waveforms at stations MAT, SHK, and HKC (all WWSSN stations). These stations are close to the null axis in the radiation pattern and extremely sensitive to small perturbations in the mechanism. We could not improve their fit without severely worsening the fit at other stations.

This event was followed by numerous aftershocks, the largest of which, of $m_b = 5.4$, is marked B in Fig. 10(a) and occured at the SW termination of the aftershock zone, near Skyros. This aftershock is discussed below (1981 December 27).

The aftershock zone following this event is elongated NE (Fig. 10a) suggesting that the NE striking nodal plane was the fault plane. The slip vector and strike of the NE trending nodal plane in this event differ from that of its biggest aftershock, and may correlate with a similar change in bathymetric trend in the eastern part of the Skyros basin (Figs 7 and 10).

1981 December 27

This earthquake occured on the southern edge of the Skyros basin (Fig. 7). The source characteristics of this event are similar to that of the one discussed above. The minimum misfit solution (Fig. A10) is well constrained by both the waveforms and first motion *P* polarity readings (Fig. 4n), and is consistent with right-lateral slip on the NE trending nodal plane. The aftershock zone of this event is shown with that of the main shock in Fig. 10(a).

The waveforms used in this event include the WWSSN, and the digitally recorded seismograms of the DWWSSN, SRO and ASRO networks. Although this event is much smaller than the 1981 December 19 event, it contains more *SH*-waveforms than main shock itself, because fewer seismograms were clipped.

The source mechanism is tightly constrained by the first motions and by the changes in *P* polarity between COL and MAT and SH polarity between TATO and BAG and between LON and KEV. Our strike (216°) for this event is almost the same as that (219°) in the CMT solution for this earthquake reported by Ekström & England (1989). Though they give the same strike (220°) for the main shock of 1981 December 19, both the first motions (Fig. 4m) and our waveform data (Fig. A9) require the main shock to have a more easterly strike.

1982 January 18

The minimum misfit solution for this earthquake is shown in Fig. A11. The source orientation is well constrained by waveforms (especially *SH*) at nodal stations and by first motion polarities (Fig. 4o), with which minimum misfit solution is compatible. The body waveform data, obtained from the WWSSN and the digital DWWSSN, SRO and ASRO networks, have an excellent station distribution for both *P*- and *SH*-waves. Some complications are observed on the *P*-waveforms from WWSSN stations to the east, indicating that the rupture history may be more complicated than our simple solution suggests. We did not have sufficient higher frequency data to investigate this further.

This event occured within the Sporades basin in the western part of the North Aegean trough. Fig. 10(b) shows the aftershock zone of this earthquake, which is elongated NE suggesting that the nodal plane with this strike was the

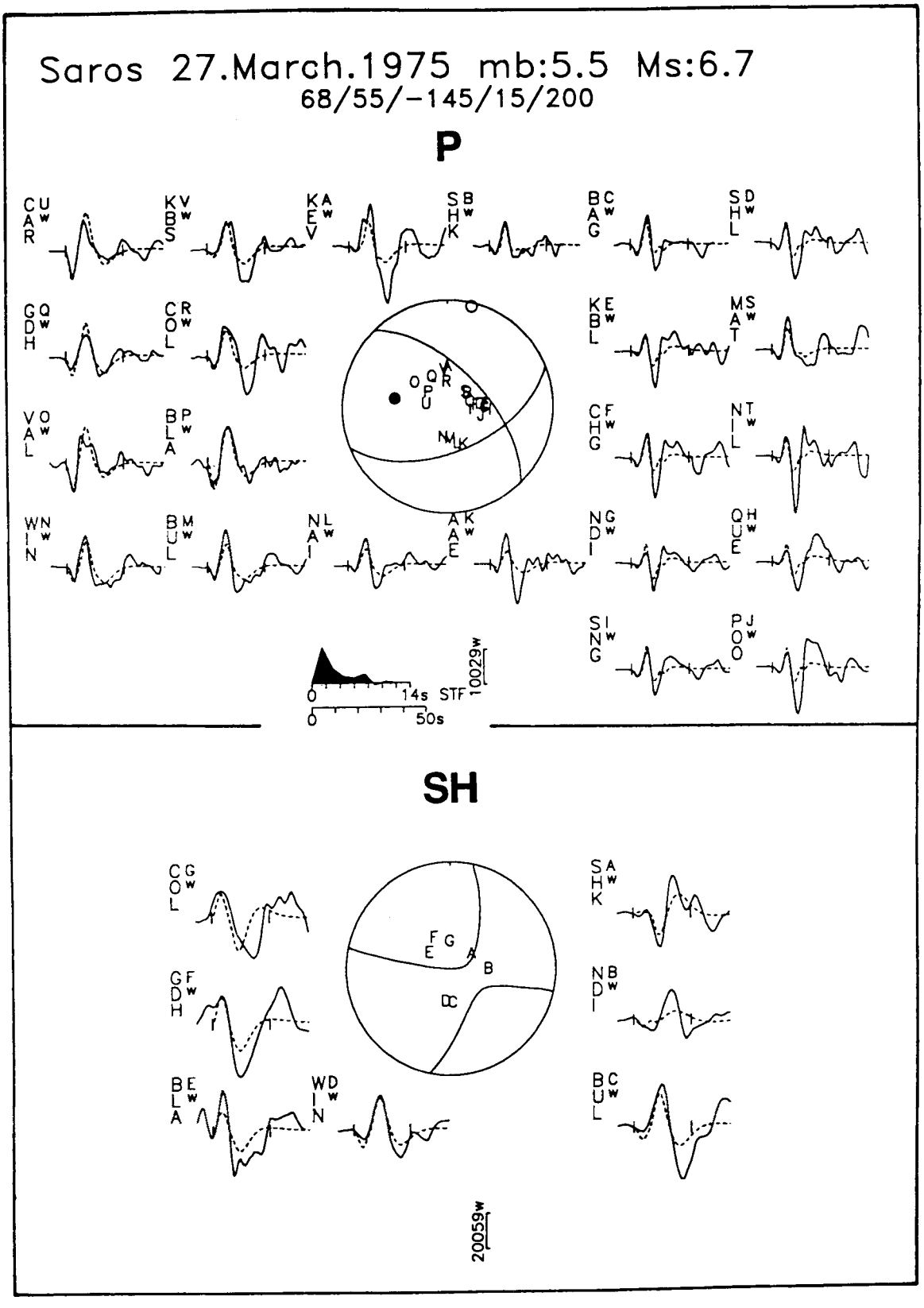

Figure A7. Minimum misfit solution for the earthquake of 1975 March 27. The display convention is the same as in Fig. 5.

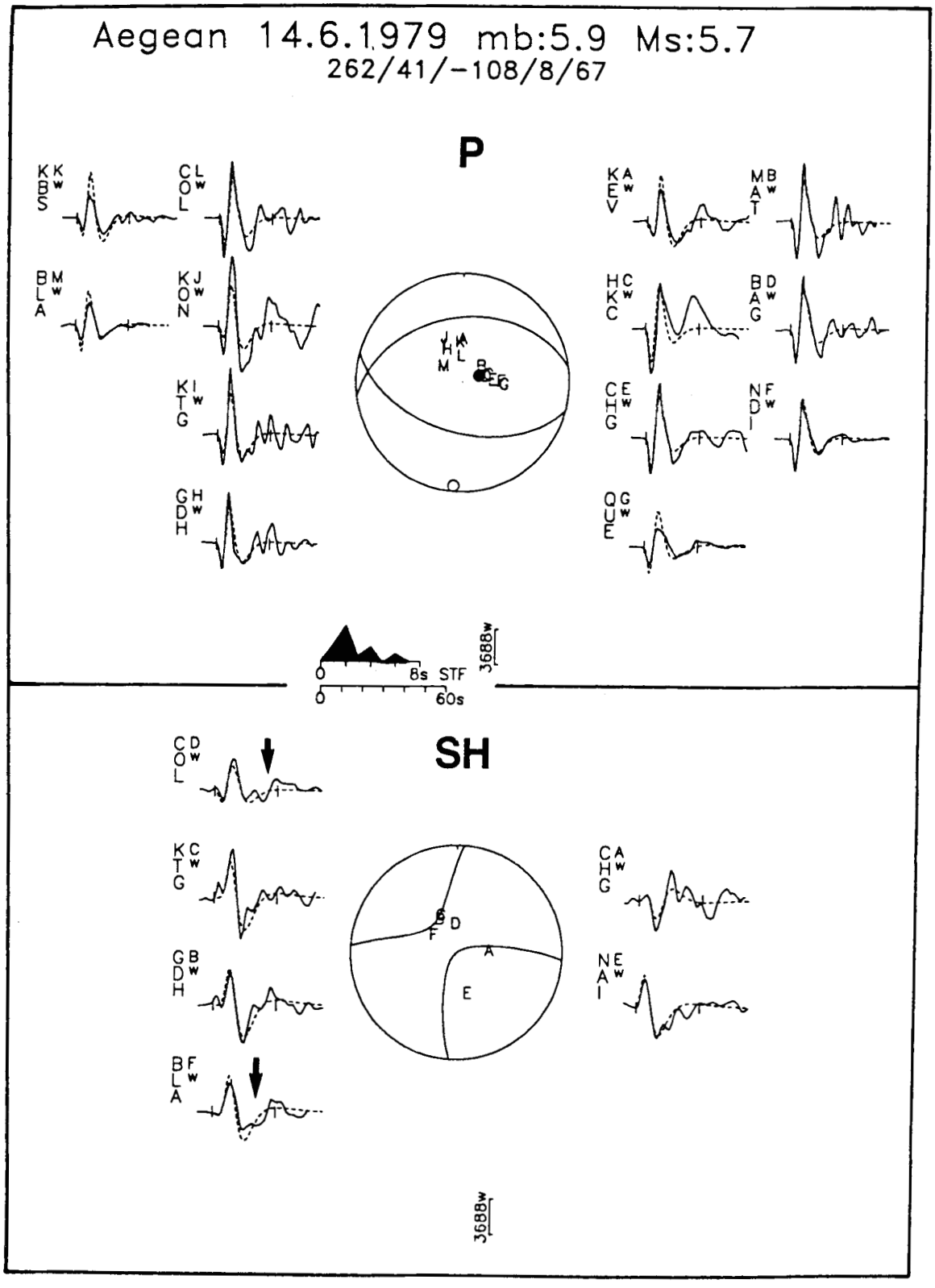

Figure A8. Minimum misfit solution for the earthquake of 1975 June 14. The display convention is the same as in Fig. 5.

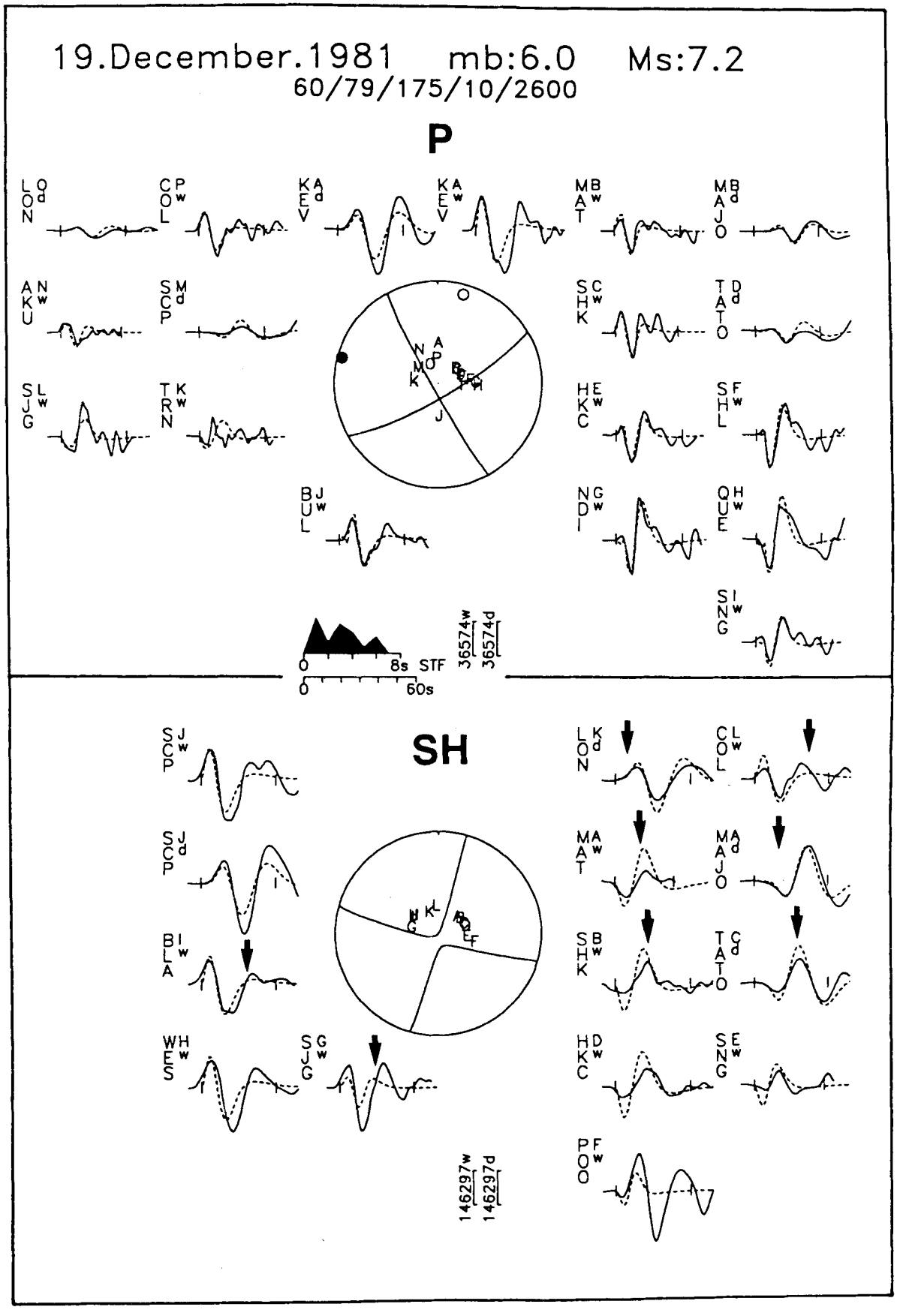

Figure A9. Minimum misfit solutions for the earthquake of 1981 December 19. The display convention is the same as in Fig. 5.

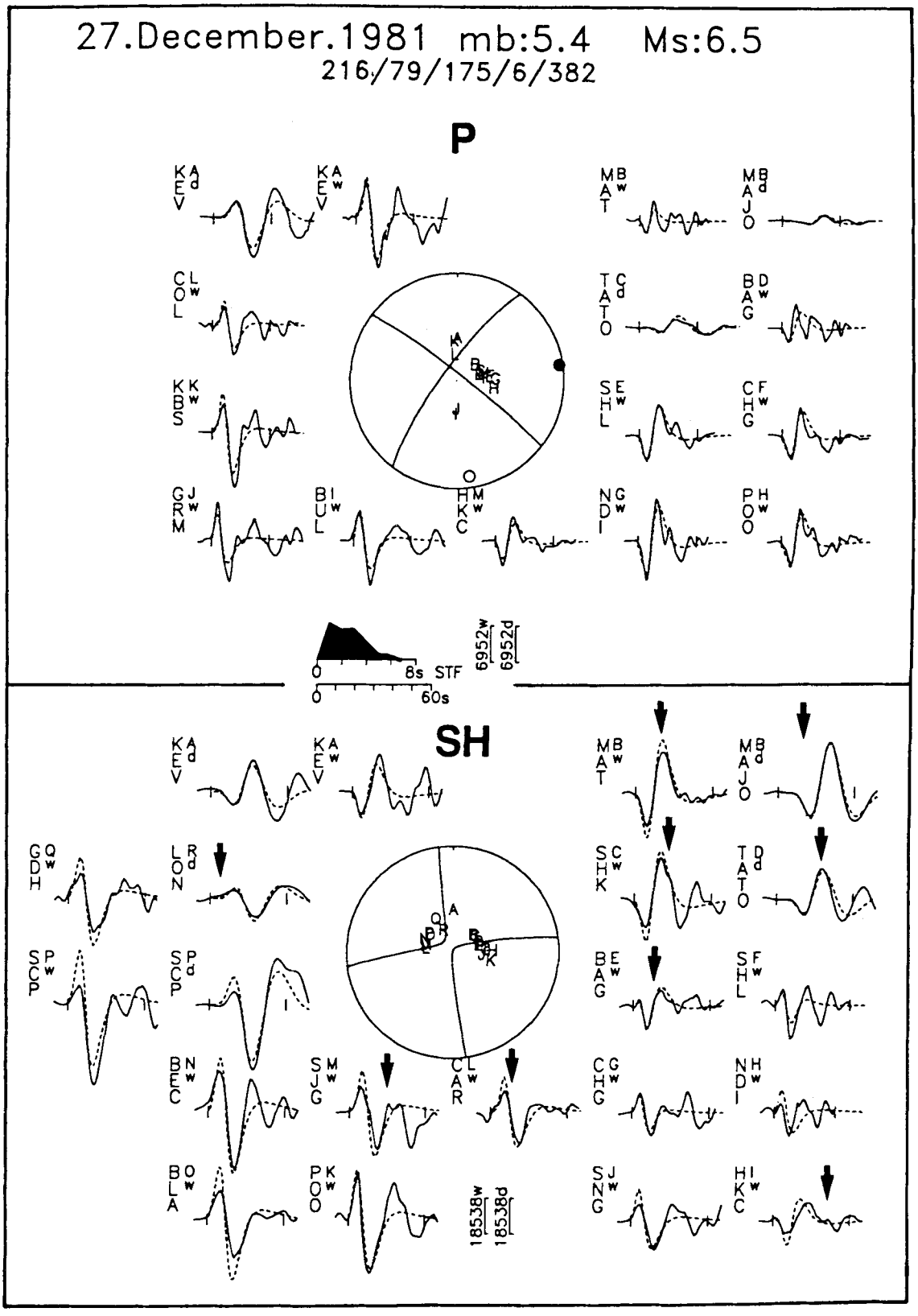

Figure A10. Minimum misfit solution for the earthquake of 1981 December 27. The display convention is the same as in Fig. 5.

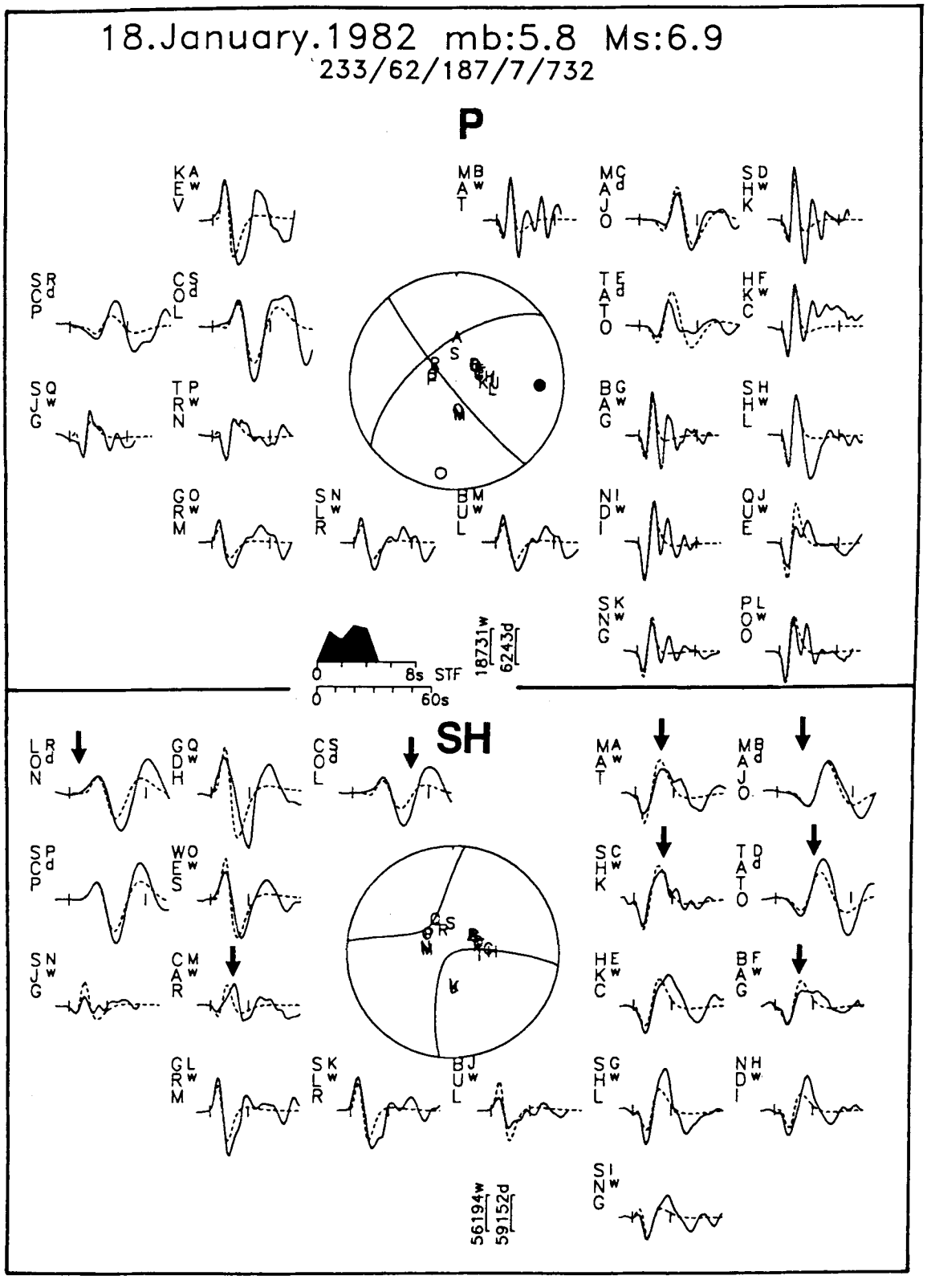

Figure A11. Minimum misfit solution for the earthquake of 1982 January 18. The display convention is the same as in Fig. 5.

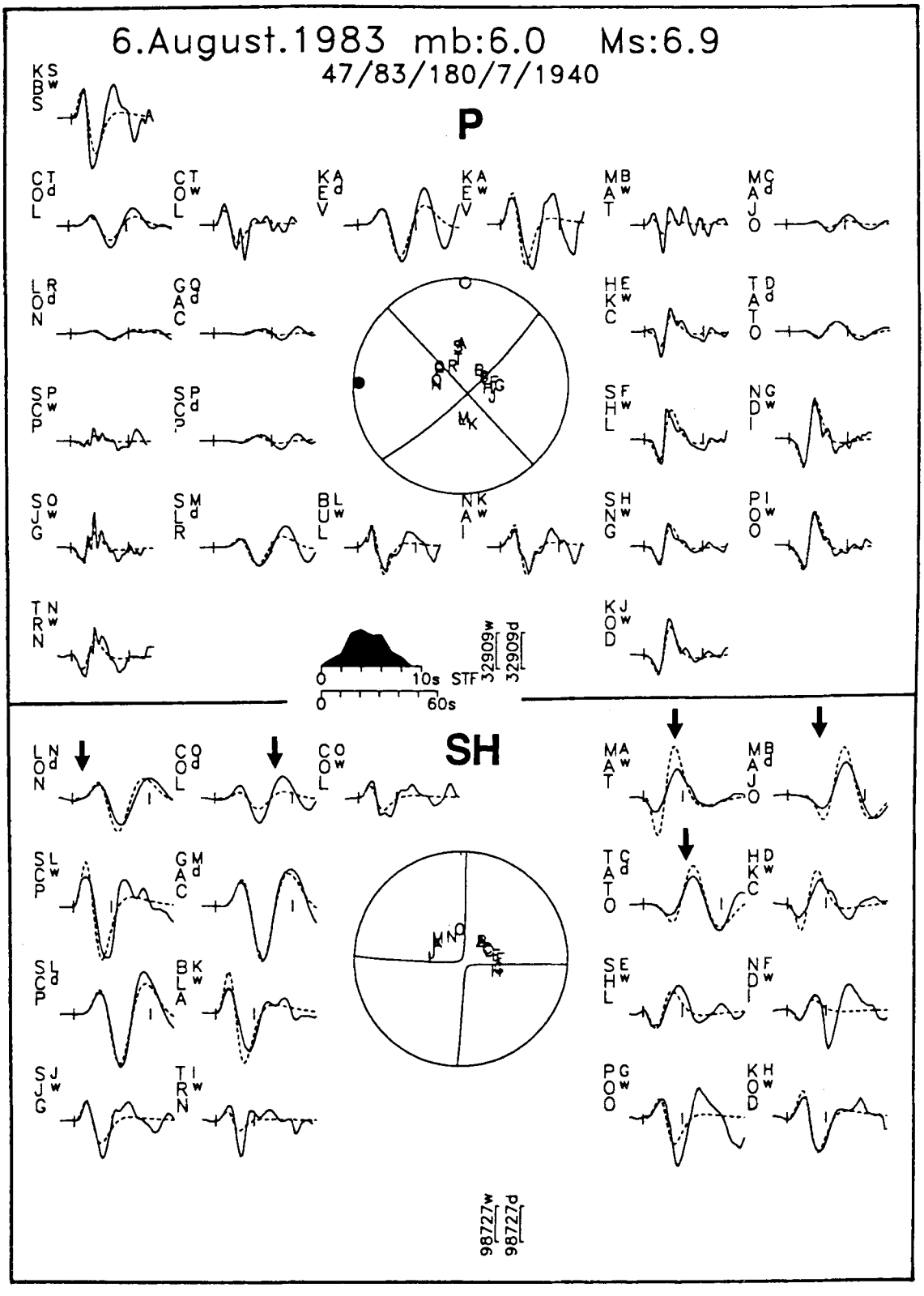

Figure A12. Minimum misfit solution for the earthquake of 1983 August 6. The display convention is the same as in Fig. 5.

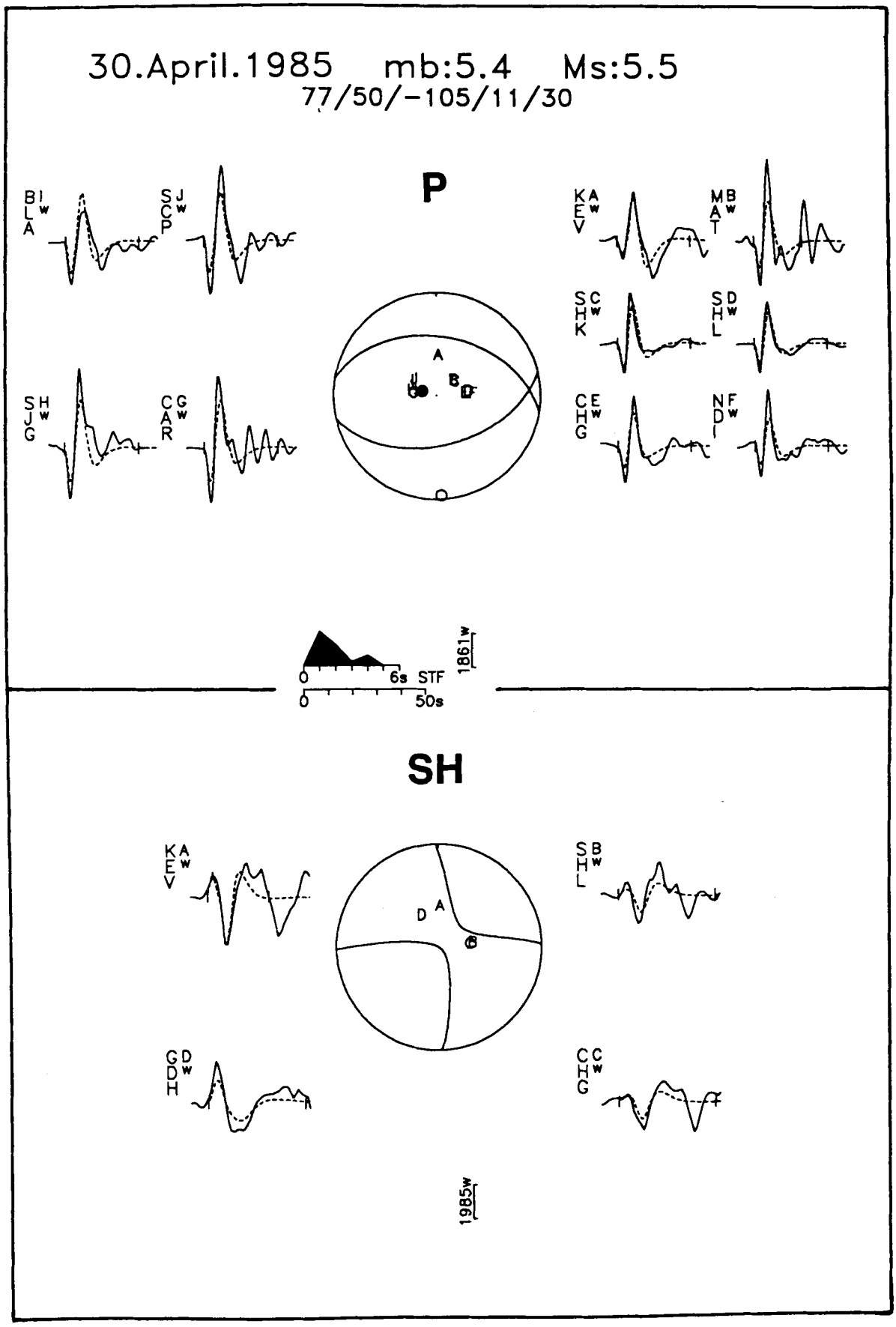

Figure A13. Minimum misfit solution for the earthquake of 1985 April 30. The display convention is the same as in Fig. 5.

fault plane. Our solution for this event is, within our estimated errors, the same as that of the CMT solution (241/57/−176) by Ekström & England (1989).

1983 August 6

This was one of the larger events in our study, $M_o = 1.94 \times 10^{19}$ N m. It was well recorded at all azimuths, and there is excellent coherence between waveforms at adjacent stations on the focal sphere. Fig. A12 shows the minimum misfit solution, which is compatible with all first motion *P* polarities (Fig. 4p).

This event occured in the NE part of the Sporades basin. Its aftershock distribution (Fig. 10c) is elongated NE–SW suggesting that the nodal plane with this strike was the fault plane. Our solution for this event is very similar to that (229/81/−174) of the CMT solution by Ekström & England (1989): the only difference is that their fault plane dips 81°NW whereas ours dips 83°SE. Theirs violates the first motion polarity at MAT.

1985 April 30

This was the smallest event ($M_o = 30 \times 10^{16}$ N m) in our study. In spite of the paucity of waveforms available for this event (Fig. A13), its focal parameters are well determined, and consistent with all first motion *P* polarities (Fig. 4q) except at IST, which is a close station, whose position on the focal sphere is uncertain. The source orientation is mainly constrained by the first motions and by *SH*-waveforms at KEV, SHL and CHG (Fig. A13).

This event occured in the epicentral region of 1980 Volos sequence (5*, 6*, 7* in Fig. 8), with a similar mechanism to those earlier events. Our mechanism for this event is almost identical to that of the CMT solution reported by Ekström & England (1989).

APPENDIX B: A RE-EVALUATION OF THE FAULTING IN THE 1981 GULF OF CORINTH EARTHQUAKES

In the course of this study we reanalysed the teleseismic waveform and location data for the 1981 earthquake sequence in the Gulf of Corinth. The sequence consisted of three events with M_s larger than 6.0, which produced over 20 km of normal faulting at the surface. The surface ruptures occurred on pre-existing faults that dip both N and S on both sides of the Gulf of Corinth, which is an active asymmetric graben. The surface faulting was described by Jackson *et al.* (1982a) and Mariolakos *et al.* (1982), and the aftershocks of the sequence were studied by King *et al.* (1985). Sebrier (1977), Jackson *et al.* (1982a), Vita Finzi & King (1985), Keraudren & Sorel (1987), Collier (1990), Doutsos & Piper (1990) and Roberts & Jackson (1991) discuss various aspects of the surrounding geology and geomorphology, including the uplift and subsidence of the coastline, and its relation with the normal faulting. The seismograms of the three largest earthquakes were studied by Jackson *et al.* (1982a), Kim, Kulhánek & Meyer (1984), Bezzeghoud, Deschamps & Madariaga (1986) and Ekström & England (1989). Jackson *et al.* (1982a) refined the teleseismic locations of the main events using relative locations.

The reason for discussing these events separately, and in more detail than the others, is that in 1981 it was not obvious which segments of surface faulting were associated with each large earthquake of the sequence, though Jackson *et al.* (1982a) suggested an answer, based on the limited data that were then available. Since the study by Jackson *et al.* (1982a) much more waveform and teleseismic arrival time data have become available. These have allowed improved location and focal mechanism determinations for the main events of the sequence, which are discussed here, together with a reassessment of the faulting related to each event.

B1 Focal mechanisms

1981 February 24

This was the first and largest event of the sequence. The minimum misfit solution is shown in Fig. B1, and the first motions in Fig. 4(j). The solution is well constrained by waveform and first motion data at all azimuths. The only inconsistent first motion is at IST (Istanbul), which is a nearby station close to a nodal plane, and whose position on the focal sphere is uncertain. In Fig. B2, we compare, at selected stations, the waveforms from this minimum misfit solution with those from some of the other solutions that have been published for this event. The new solution is clearly much better constrained than that of Jackson *et al.* (1982a), which had fewer first motions and waveforms and no *SH*-waves, and which produces a poor fit of the observed seismograms at several stations (row 2). In row 3 we fixed the source orientation to that given by Kim *et al.* (1984), and inverted for depth and time function. Their solution is not very different from ours, but produces a marginally worse fit to the *P*-wave at AAE and some *SH* shapes. The CMT solution by Ekström & England (1989) differs from our solution by 20° in strike, 5° in dip and 10° in rake. The differences in strike and rake are marginally outside the acceptable errors in our solution (Table 1), and their solution (row 4) produces a slightly worse fit to the *P*-wave at AAE and *SH* at SHK, WIN and BLA. We conclude that the best single source fit to this event has the orientation: strike 264° ± 15°; dip 42° ± 5°; rake −80° ± 10°. Our estimate of the centroid depth is 12 ± 2 km.

1981 February 25

This was the second-largest event of the sequence, occurring only 5.5 hr after the largest shock. The minimum misfit solution is shown in Fig. B3, and the first motion polarities, all of which are compatible with this solution, in Fig. 4(k). The main change from the solution of Jackson *et al.* (1982a) is in the strike of the nodal plane dipping SE, which is much better constrained by the new first motion and waveform data. The waveforms generated by the solution of Jackson *et al.* (1982a) produce an unacceptable fit to the observed seismograms (Fig. B4, row 2). The solution of Kim *et al.* (1984) is effectively within the acceptable errors of our own solution, though their strike (9° more than ours) produces a worse fit to the *P*-wave amplitude at AAE, close to a nodal plane (row 3). The CMT solution of Ekström & England

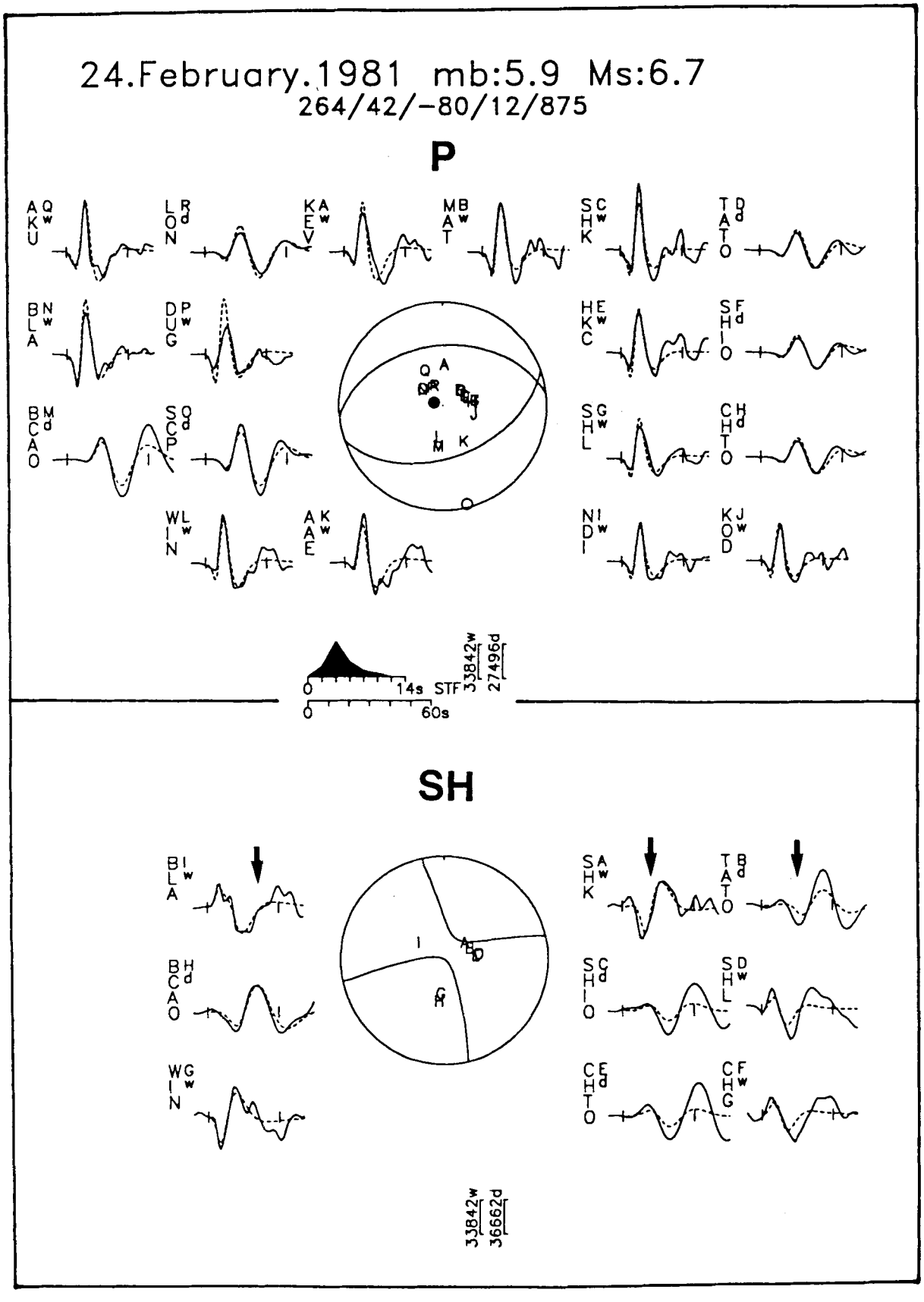

Figure B1. Minimum misfit solution for the earthquake of 1981 February 24. The display convention is the same as in Fig. 5.

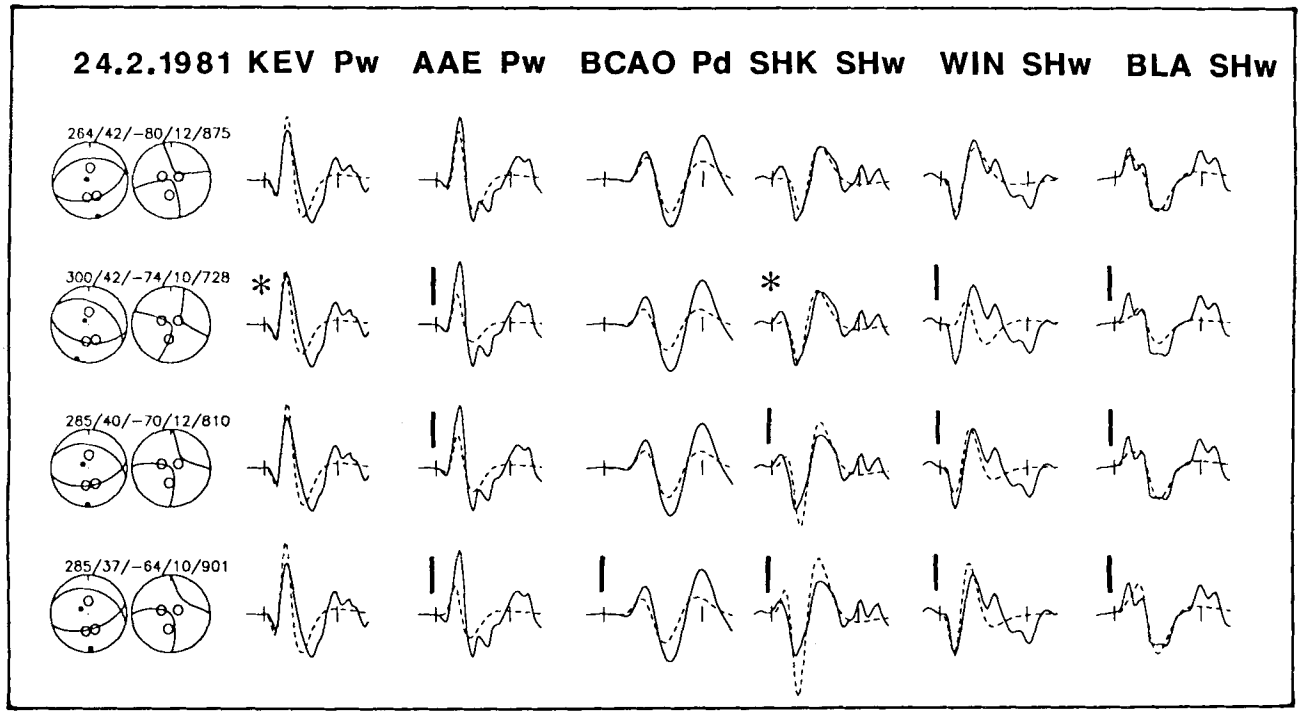

Figure B2. A comparison of different source orientations for the event of 1981 February 24. The display convention is the same as in Fig. 6. The first row shows the minimum misfit solution. In following rows the strike, dip and rake were fixed to the values of Jackson *et al.* (1982), Kim *et al.* (1984) and Ekström & England (1989) respectively, while the other parameters were left free.

(1989) differs from ours by 23° in strike, 10° in dip and 34° in rake. These differences are outside the estimated errors in our solution. In row 4 we held the strike, dip and rake to their solution, allowing the moment and depth to be free in the inversion. The fit of waveforms is noticeably worse than in the minimum misfit solution, with the wrong polarity for the *P*-wave at AAE. Our estimate of the source orientation is: strike 241° ± 6°; dip 44° ± 5°; rake −85° ± 15°.

1981 March 4

The minimum misfit solution to this event is similar to that of February 25 (Fig. B5). First motions are all compatible with this solution (Fig. 4l), which differs from that of Jackson *et al.* (1982a) mainly in the strike of the nodal plane dipping SE. The solution of Jackson *et al.* (1982a) produces a poor fit to the *SH*-waveforms (Fig. B6, row 2). Our solution differs in strike by 10° from that of Kim *et al.* (1984). This difference is close to the uncertainty in our solution, but Kim *et al.*'s solution does produce a worse fit to the *SH* pulse at BLA (row 3). The solution of Ekström & England (1989) differs from ours by almost 30° in both strike and rake. Their solution is not compatible with first motions at stations to the east, and produces an inferior fit to the waveforms, particularly SH at BLA. It is significant that of the three main events in this sequence, only this one has a large non-double component in the Ekström & England's CMT solution (the eigenvalues of their moment tensor are 1.04, 1.81, −2.85). Their best double couple solution is thus significantly different from the moment tensor that produced the best results in their inversion. Our estimate of the source orientation in this event is: strike 230° ± 5°; dip 45° ± 5°; rake −90° ± 10.

B2 Locations

In 1981 there were few permanent seismic stations in Greece, and epicentral locations based on teleseismic arrival times can be in error by more than 10 km (Soufleris 1980; Soufleris *et al.* 1982). In an attempt to improve the epicentral estimates for the Gulf of Corinth earthquakes, Jackson *et al.* (1982a) used a relative location procedure to produce a pattern of relative epicentres for the three largest events and a fourth, reference shock, that was also accurately located by a dense temporarly local network, and thus allowed the pattern to be positioned geographically. In Jackson *et al.*'s (1982a) report about 100 relative arrival times could be used in each relative location. Much more data is now available with better azimuthal coverage, so we have again relocated these earthquakes, using the same procedure, which is that described by Jackson & Fitch (1979). This time, more than 300 relative arrival times are used for each of the three main events, and we have added the large aftershock of 1981 March 5 as well the aftershock of 1981 March 7, which was once again used as the reference shock to position the pattern geographically (Table B1).

Figure B7 shows our relocations. The five symbol shapes, with adjacent numbers 1–5, refer to the five earthquakes (Table B1). There are several locations given for each event: the type of shading within each symbol refers to the way in which the location was obtained. Symbols of the smallest size are: USGS–PDE locations (open), ISC locations (filled) and locations estimated by Jackson *et al.* (1982a) using the relative location procedure. The open diamond marked 5R is the epicentre of the reference shock, the aftershock of $m_b = 5.4$ on 1981 March 7, determined by the local network (King *et al.* 1985). Each of the events 1–4

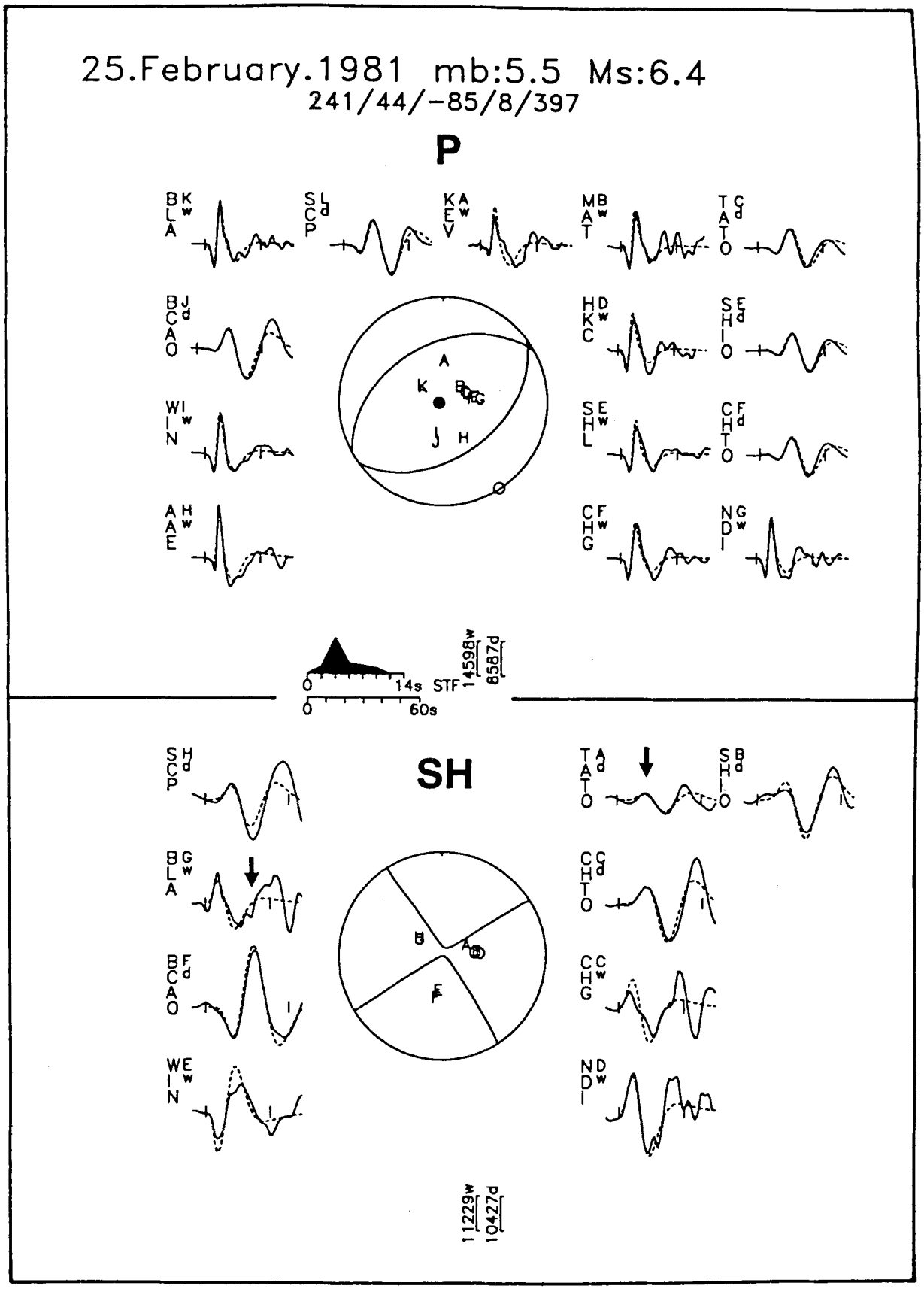

Figure B3. Minimum misfit solution for the earthquake of 1981 February 25. The display convention is the same as in Fig. 5.

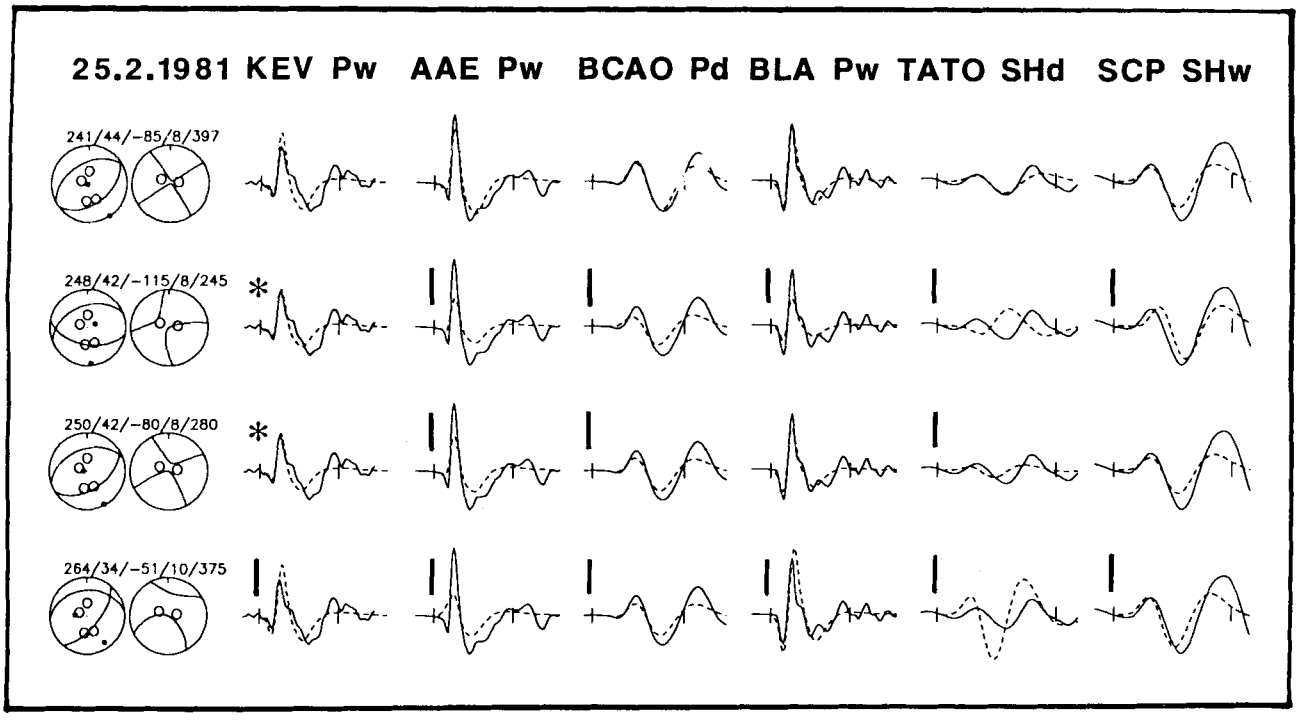

Figure B4. A comparison of different source orientations for the event of 1981 February 25. The display convention is the same as in Fig. 6. The first row shows the minimum misfit solution. In following rows the strike, dip and rake were fixed to the values of Jackson *et al.* (1982), Kim *et al.* (1984) and Ekström & England (1989) respectively, while the other parameters were left free.

has three large symbols, each with different shading. These refer to whether the first, second or third main event was used as the master event, relative to which the others, including the reference shock, were located. Thus, to obtain the locations shown by the large filled symbols, earthquakes 2–5 were relocated relative to event 1. This pattern was then shifted so that event 5 (the reference) was positioned over its known epicentre (the open diamond marked 5R). To obtain the locations shown by diagonal shading, events 1 and 3–5 were relocated relative to event 2, and then repositioned, and so on. There are therefore three estimated epicentres for each of events 1–4. Details of the relocation procedure are given by Jackson & Fitch (1979): we used a P velocity of 6.8 km s^{-1} to represent the average lower crustal velocity between the hypocentres, and used all arrival times with relative residuals up to ±3.0 s.

The true uncertainties in these new locations are difficult to estimate, and are likely to be larger than the 3–4 km formal standard errors returned by the relocation program. A better guide is probably the spread of the three large symbols for each event. Note that the large symbols with diagonal shading (the relocations using No. 2 as master) are at the SW end of the group for each earthquake, whereas the filled and lightly shaded large symbols (the relocations using Nos 1 and 3 as master) are close together. Events 1 and 3 produced clear impulsive onsets for teleseismic short-period records, whereas onsets for event 2 were generally emergent, and may have been led to more errors in the identification of the arrival time. Thus the locations that used event 2 as the master may be the least reliable.

All the events show a S to SSW shift of up to 10 km with respect to the USGS and ISC locations, which was noted by Jackson *et al.* (1982a), and is seen elsewhere in Greece (Soufleris 1980; Soufleris *et al.* 1982). The relative pattern of epicentres for events 1–3 has not changed much from those of Jackson *et al.* (1982a), but the geographical position has shifted east. This reflects the great increase (from 58 to about 270, see Table B1) in the number of stations and to locate the reference shock relative to the rest of the pattern.

B3 A reassessment of the faulting in 1981

Figure B8 shows is a map of the faulting in the eastern Gulf of Corinth, including our prefered focal mechanisms for the three largest events (1–3) and the CMT solutions by Ekström & England (1989) for the two largest aftershocks (4 and 5), which are shown centred over our new epicentral locations.

The faulting that was reactivated at the surface in the 1981 sequence is shown in Fig. B8 with filled blocks in the hanging walls. On the south side of the Gulf, the main faulting was in the segments marked 1 and 2, along the north side of Mt Gerania. The combined length of these segments is 12 km, and the average displacement on them was 0.9 ± 0.3 m, down to the north. Segment 3 showed surface displacements at various locations along a 5–7 km length: these were less continuous than in segments 1 and 2, and generally smaller in amplitude (about 0.3 m). Small displacements (about 10 cm) were observed along a relatively minor fault (segment 4) that outcropped on land for about 1 km, in the NW part of the Perakora peninsula. On the north side surface faulting was observed in two segments (5 and 6) each about 6 km long, and offset by about 3 km. Average displacements on each segment were 0.6 ± 0.2 m, downthrown to the south.

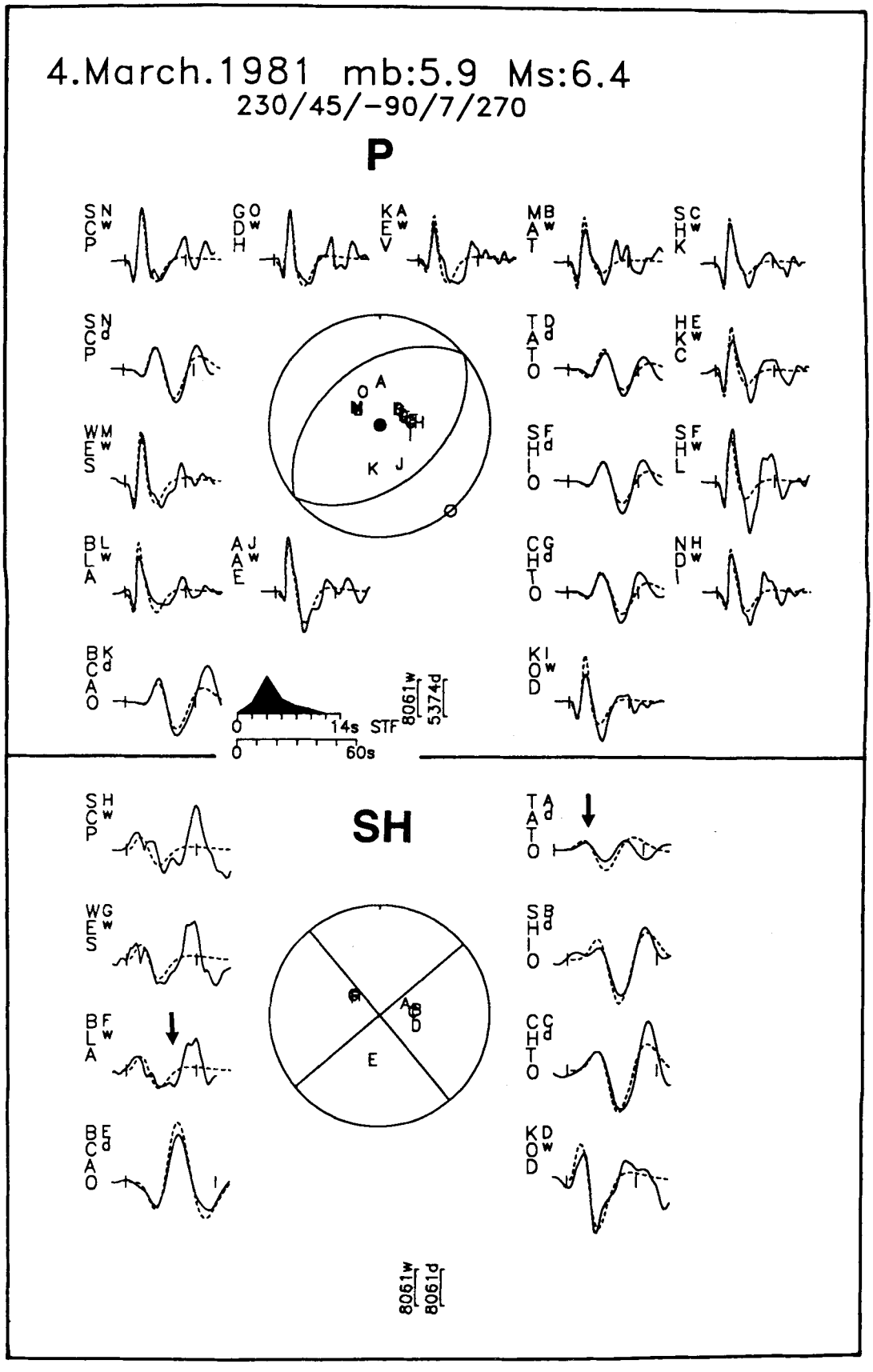

Figure B5. Minimum misfit solution for the earthquake of 1981 March 4. The display convention is the same as in Fig. 5.

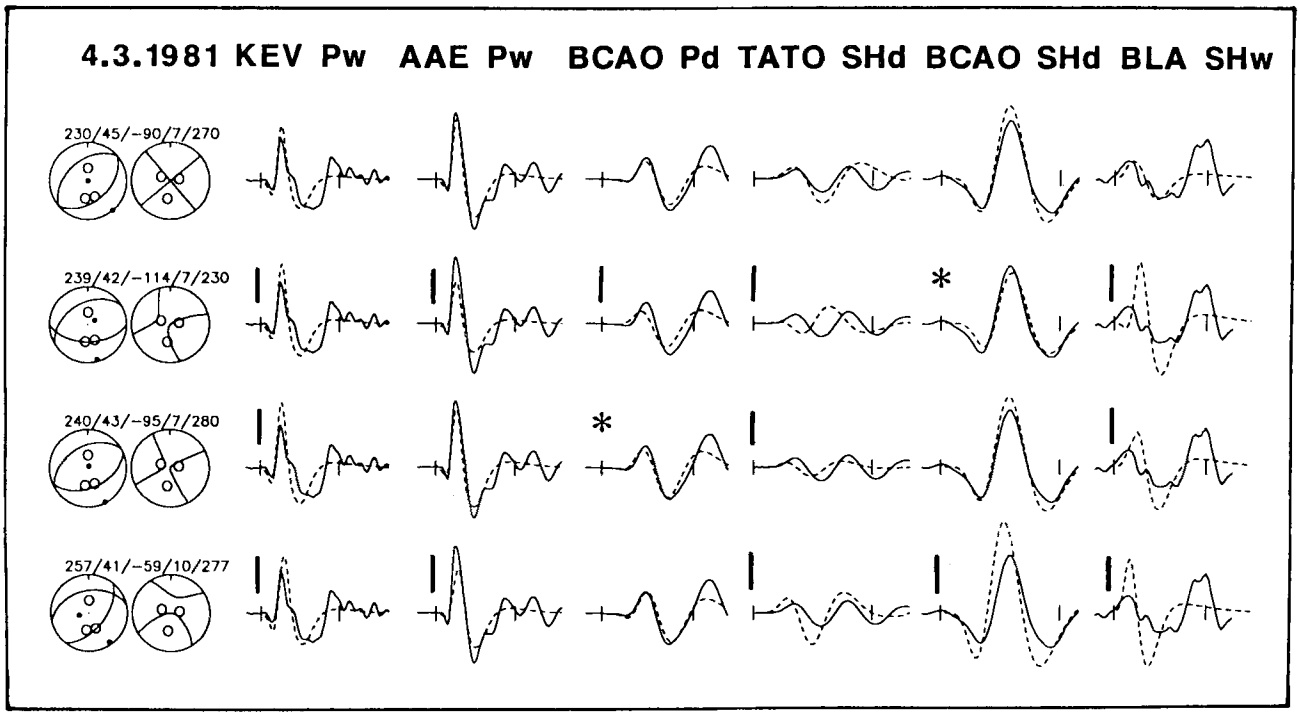

Figure B6. A comparison of different source orientations for the event of 1981 March 4. The display convention is the same as in Fig. 6. The first row shows the minimum misfit solution. In following rows the strike, dip and rake were fixed to the values of Jackson *et al.* (1982), Kim *et al.* (1984) and Ekström & England (1989) respectively, while the other parameters were left free.

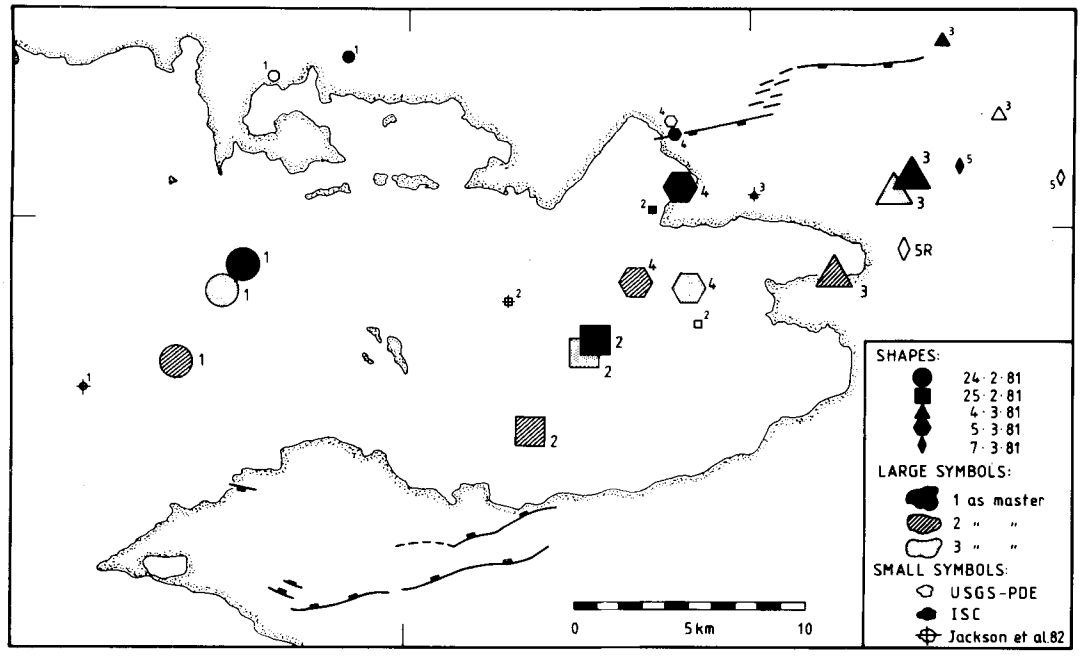

Figure B7. Relative relocations of the five largest events in the 1981 sequence (Table B1). Each event is identified by shape (circles, squares, triangles, hexagons, diamonds: see inset), and there are five or six locations for each of events 1 to 4. The smallest symbols are the USGS (open) and ISC (filled) locations. The three largest symbols for each event depend on whether event 1 (black), 2 (diagonal shading) or 3 (stippled) was used as the master event (see text). The small symbols with a cross for events 1 to 3 are the earlier relocations of Jackson *et al.* (1982a). Three locations are given for the reference event (no. 5): the two small diamonds are the USGS and ISC locations, the large diamond marked 5R is the location determined by the local seismic network installed to monitor aftershocks (Jackson *et al.* 1982a). The faulting that moved at the surface in the 1981 sequence is marked with black blocks in the hanging walls.

Table B1. Source parameters of the 1981 Gulf of Corinth earthquakes.

No.	Date (d m y)	I.S.C m_b	I.S.C M_s	M_o $\times 10^{16}$ (N m)	Centr. Depth (km)	Str. (°)	Dip (°)	Rake (°)	N1	N2	N3
1.	24.02.1981	6.1	6.7	875	12	264	42	-80	—	371	336
2.	25.02.1981	5.7	6.4	397	8	241	44	-85	371	—	329
3.	04.03.1981	5.8	6.3	270	7	230	45	-90	336	329	—
4.	05.03.1981	5.3	5.3	18	15F	276	43	-59	245	239	267
5.	07.03.1981	5.4	5.4	15	15F	091	41	-84	263	263	277

– No. refers to number in Figs. B7 and B8.
– Strike, dip, rake, depth (fixed at 15 km), and moments for numbers 4 and 5 are from Ekström & England (1989).
– N1, N2, N3 are the number of stations used in the relocation of the event's epicentre. Event no 1 was used as the master event for column N1; event no 2 for N2, and no 3 for N3.

The faulting in segments 5 and 6 can be definitely associated with event 3 (1981 March 4), as the surface displacements were not present before this earthquake, and were observed following it. Any amplification of the observed displacements by events 4 and 5 must be insignificant, as their combined moments can only account for about 0.07 m slip on each segment. Our estimate of the centroid depth for event 3 was 7 ± 3 km, and the aftershocks in this region extended to a depth of about 10 km. If we assume a depth of faulting of 8–10 km, the seismic moment of 2.7×10^{18} N m we obtained for event 3 [close to that from Ekström & England (1989), of 2.8×10^{18} N m] can account for 0.7–0.9 m slip on a fault 12 km long: which is close to what was observed. Our principal new result for the March 4 earthquake is the definite disagreement between the slip vector observed at the surface, which was in the direction 010°–030° (Jackson *et al.* 1982a), and that on the SE-dipping nodal plane of the teleseismically determined focal mechanism, which was 320° (Table 1). The teleseismic slip vector is well constrained by the first motion polarities in Europe (Fig. 4l), as well as by waveforms, and the discrepancy of 50°–80° between this and the surface slip vector is certainly greater than their respective errors. It is rare for surface slip vectors to be reported after earthquakes, and we are not aware of any other cases where their disagreement with teleseismic determinations can be demonstrated. Of course, our inversion of long-period teleseismic data assumes that the faulting may be represented by a point source in space. The faulting in this earthquake was obviously segmented, though the scale of the discontinuities in an earthquake of this size cannot be resolved with the data we used. An indication of the complexity of this event may be the large (42 per cent) non-double couple component found in the CMT inversion by Ekström & England (1989).

The faulting on the south side of the Gulf is more difficult to associate with particular events. Both events 1 and 2 occurred during the night (22 53 and 04 35 hr local time) of February 24–25, and the faulting in segments 1 and 2 (Fig. B8) was not discovered until the following morning. Jackson *et al.* (1982a) suggested that the first event moved a fault offshore, west of Perakora peninsula. Their main reasons for this were: (a) a reported tsunami following the event; (b) a discrepancy between the strike and slip vector in their (poorly constrained) focal mechanism and that observed at the surface on segments 1 and 2; and (c) a location for the event west of the Perakora peninsula (see Fig. B7). With the information now available, these reasons are not convincing. Large submarine slumps in the eastern Gulf of Corinth were later identified by Perissoratis, Mitropoulos & Angelopoulos (1986) using seismic sparker data, and could have been responsible for the tsunami. The new focal mechanism has a strike and slip vector (340°) that are compatible with those observed at the surface (slip vector $350° \pm 10°$). The new location of the epicentre is farther east, and, if the depth of the hypocentre is close to that of the centroid (12 ± 2 km), is compatible with a fault that is planar in cross-section from the surface to about 12 km. The aftershocks around Perakora extend a little deeper than those to the east (King *et al.* 1985). If we assume a depth of faulting of 12 ± 2 km, then the moment we estimated for event 1, of 8.75×10^{18} N m [cf 9.01×10^{18} N m from Ekström & England (1989)] can account for a displacement on a fault 12 km long of 1.4 ± 0.2 m. This is more than enough to account for the surface displacements on segments 1 and 2 in Fig. B8, which averaged 0.8 ± 0.3 m. Thus the available data are compatible with the faulting in segments 1 and 2 having occurred during the first event, on 24 February.

What of event No. 2? Jackson *et al.* (1982a) thought that this event accounted for the faulting in segments 1 and 2. The new data also cannot rule this out. The teleseismic (324°) and surface ($350° \pm 10°$) slip vectors are not greatly different. The centroid depth is shallower (8 ± 2 km) than that of the first event (12 ± 2 km). If we take a depth of faulting of 10 ± 2 km, then our moment determined for this event, of 3.97×10^{18} N m [cf. 3.75×10^{18} N m from Ekström & England (1989)], can account for a displacement on a fault 12 km long of 0.8 ± 0.2 m. This, too, is close to that observed on segments 1 and 2. The epicentre and depth of this earthquake are also compatible with roughly planar faulting from the surface to a depth of 10–12 km.

Both earthquakes 1 and 2 have dips to their NW nodal planes (42° and 44°) that are similar to that observed at the surface on segments 1 and 2 ($45° \pm 15°$), further reinforcing the likelihood of planar faulting. It is improbable that both earthquakes moved the same fault segments 1 and 2: their combined moments would yield an average slip of 2.2 ± 0.2 m, which is larger than that observed. But even this unlikely possibility cannot be ruled out. The epicentres of the two events are at opposite ends of the surface faulting in segments 1 and 2, implying propagation eastwards, if event 1 was responsible, or westwards in event 2.

What of the faulting in segment 3? The observed displacements on this segment were smaller and less continuous than in segments 1 and 2. At their eastern end they could not be traced into coarse conglomeratic fan material and then a change in footwall lithology from hard, crystalline limestone (in which faulting in segments 1, 2, 5 and 6 was easily seen) to soft, easily eroded basic igneous rocks. The coastal fault clearly continues east of the observed surface ruptures, but with less obvious morphological expression, and goes offshore west of Alepohori (Fig. B8). It is possible that faulting in 1981 continued east of the observed displacements in segment 3, but had no surface expression. This is consistent with both the smaller size of event 2 (relative to event 1), and the change in

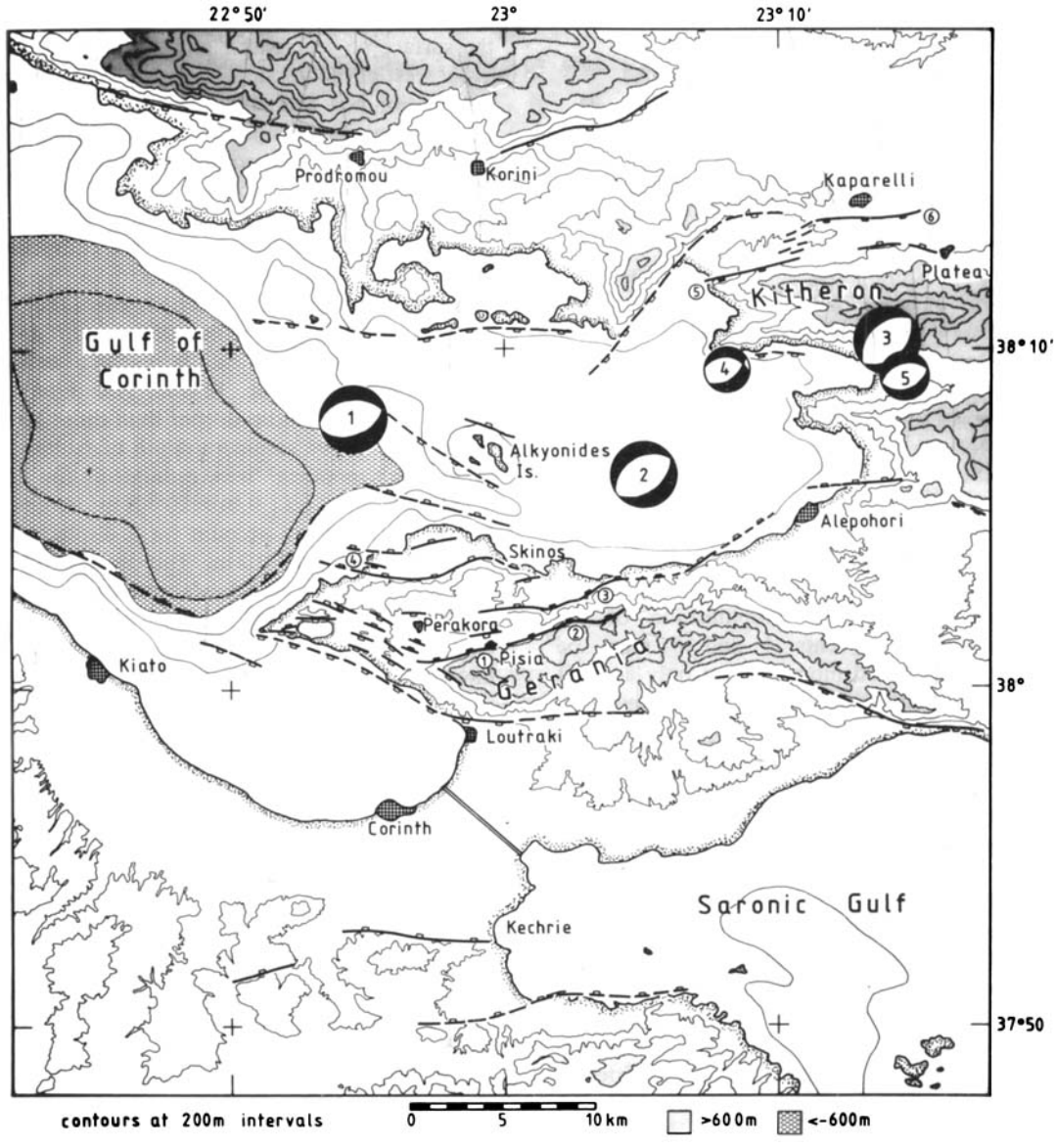

Figure B8. Summary tectonic map of the eastern Gulf of Corinth. Focal mechanisms are for events 1 to 5 in Table B1, and are positioned at their redetermined epicentres (Fig. B7). Normal faults that moved at the surface in the 1981 earthquake sequence are numbered 1 to 5 and have filled blocks in their hanging walls. Other normal faults are marked with open blocks. Faulting offshore is based partly on the work of Perissoratis *et al.* (1986). Faulting onshore is from our own observations, and those of Collier (1988).

footwall lithology. Subsidence of parts of the coastline east of the eastern termination of segment 3 marked in Figs B7 and B8 was observed after the 1981 earthquakes, and would be expected in the hangingwall of the coastal fault: but in the soft coastal deposits this subsidence was not easily distinguishable from slumping. We conclude that it is possible that the second event (on 25 February) moved this coastal fault, including segment 3 and farther east.

Thus the conclusions of Jackson *et al.* (1982a) may be correct, and the first event may have moved a large fault dipping north, west of the Perakora peninsula. Such faults are clear in the bathymetry and in seismic reflection records (Brooks & Ferentinos 1984; Perissoratis *et al.* 1986). But their conclusions are not secure. It is also possible, and, on balance, we think more likely, that the first earthquake, on 1981 February 24, moved the fault along Mt Gerania (segments 1 and 2), and the second, on 1981 February 25, moved the coastal fault between Skinos and Alepohori (segment 3 and eastwards).

APPENDIX C

In this Appendix we derive the expressions necessary to calculate the velocity field associated with the broken slat model illustrated in Figs 15(c) and 16.

The geometry is shown in Fig. C1. Lines OA and DC are on the margins of rigid plates that rotate at rates Ω_1, and Ω_2 (positive anticlockwise) about a vertical axis in the frame given. ABC is the nth broken slat with left (AB) and right (BC) arms pivoted about screws A and C, attached to plates 1 and 2, and about point B. The two arms rotate about vertical axes at rates ω_1^n and ω_2^n. Point D may have a

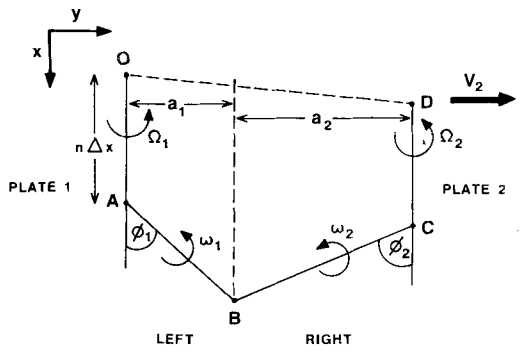

Figure C1. Sketch of the geometry used to calculate the velocity field in the broken slat model (see Fig. 15c).

velocity in the y direction of V_2, relative to the origin O. The separation of the slats along the margins is Δx, so that $OA = DC = n\,\Delta x$. We wish to calculate the velocity of any point on either the left or right arm of the broken slat, as a function of position (x, y), relative to the origin O. We can then use the velocities on neighbouring slats to find the relative velocity between them (equivalent to the slip vector on the fault) by subtraction. In our notation ${}_P\mathbf{v}_Q$ is the velocity of point Q relative to point P. Thus:

$${}_O\mathbf{v}_A^n = (0, n\Omega_1\,\Delta x), \tag{1}$$

$${}_A\mathbf{v}_B^n = \omega_1^n a_1(-1, \cot\phi_1), \tag{2}$$

$${}_B\mathbf{v}_C^n = \omega_2^n a_2(-1, -\cot\phi_2). \tag{3}$$

The velocity of C relative to O may be found by addition:

$${}_O\mathbf{v}_C^n = {}_O\mathbf{v}_A^n + {}_A\mathbf{v}_B^n + {}_B\mathbf{v}_C^n, \tag{4}$$

$${}_O\mathbf{v}_C^n = (-\omega_1^n a_1 - \omega_2^n a_2,\ n\Omega_1\,\Delta x + \omega_1^n a_1 \cot\phi_1 - \omega_2^n a_2 \cot\phi_2). \tag{5}$$

Now,

$${}_O\mathbf{v}_D = (0, V_2), \tag{6}$$

and

$${}_D\mathbf{v}_C^n = [0, \Omega_2(n\,\Delta x + a_1 \cot\phi_1 - a_2 \cot\phi_2)], \tag{7}$$

so, also by addition,

$${}_O\mathbf{v}_C = [0, V_2 + \Omega_2(n\,\Delta x + a_1 \cot\phi_1 - a_2 \cot\phi_2)]. \tag{8}$$

Equations (5) and (8) must be equal, so

$$\omega_2^n = \frac{-\omega_1^n a_1}{a_2} \tag{9}$$

and

$$\omega_1^n = A_L + B_L n\,\Delta x, \tag{10}$$

$$\omega_2^n = A_R + B_R n\,\Delta x, \tag{11}$$

where

$$A_L = [V_2 + \Omega_2(a_1 \cot\phi_1 - a_2 \cot\phi_2)]/a_1(\cot\phi_1 + \cot\phi_2), \tag{12}$$

$$B_L = (\Omega_2 - \Omega_1)/a_1(\cot\phi_1 + \cot\phi_2), \tag{13}$$

$$A_R = -a_1 A_L/a_2, \tag{14}$$

$$B_R = -a_1 B_L/a_2. \tag{15}$$

The velocity of a point L at (x, y) on the left-hand arm, which is rotating about point A is

$${}_A\mathbf{v}_L^n = \omega_1^n \times \mathbf{r} \tag{16}$$

where

$$\mathbf{r} = (x - n\,\Delta x, y) \tag{17}$$

so

$${}_A\mathbf{v}_L^n = [-\omega_1^n y, \omega_1^n(x - n\,\Delta x)], \tag{18}$$

and, by addition of (1) and (18)

$${}_O\mathbf{v}_L^n = [-\omega_1^n y, \omega_1^n x + (\Omega_1 - \omega_1^n)n\,\Delta x] \tag{19}$$

For a point R at (x, y) on the right-hand arm,

$${}_B\mathbf{v}_R^n = \omega_2^n \times \mathbf{s} \tag{20}$$

where

$$\mathbf{s} = (x - n\,\Delta x - a_1 \cot\phi_1, y - a_1) \tag{21}$$

and

$${}_O\mathbf{v}_R^n = {}_O\mathbf{v}_A^n + {}_A\mathbf{v}_B^n + {}_B\mathbf{v}_R^n, \tag{22}$$

$${}_O\mathbf{v}_R^n = \left\{\frac{\omega_1^n a_1}{a_2}[y - (a_1 + a_2)],\ \Omega_1 n\,\Delta x + \frac{\omega_1^n a_1}{a_2}[n\,\Delta x - x + (a_1 + a_2)\cot\phi_1]\right\}. \tag{23}$$

Equations (19) and (23) give the velocities of points on the left and right arms respectively. Velocities $\mathbf{V}^n$ between neighbouring blocks are calculated by subtracting the velocities on the nth and $(n+1)$th slats:

$$\mathbf{V}^n = {}_O\mathbf{v}_L^n - {}_O\mathbf{v}_L^{n+1}. \tag{24}$$

The rotation rates of the arms are given by equations (10) and (11), and the velocities of the break points B^n, are obtained by adding equations (1) and (2).

Note that if $\Omega_1 = \Omega_2 = 0$, $a_1 = a_2 = a$ and $\phi_1 = \phi_2 = \phi$ then each set (right or left) of arms is identical to the *pinned* block model of McKenzie & Jackson (1983, 1986). Considering the left-hand side,

$$\omega_1^n = V_2/2a \cot\phi = W, \tag{25}$$

which is a constant. On slat n,

$${}_O\mathbf{v}_L^n = (-Wy, Wx - Wn\,\Delta x), \tag{26}$$

on slat $(n+1)$

$${}_O\mathbf{v}_L^{n+1} = [-Wy, Wx - W(n+1)\,\Delta x] \tag{27}$$

and the relative velocity between slats is

$${}_O\mathbf{v}_L^n - {}_O\mathbf{v}_L^{n+1} = (0, W\,\Delta x), \tag{28}$$

which is in the y direction, as it should be (see McKenzie & Jackson 1983, 1986). In the notation of McKenzie & Jackson (1983),

$$V_2 = -4Ta \tag{29}$$

so

$$\tan\phi = -\frac{W}{2T} \tag{30}$$

as it should [see equation (48) of McKenzie & Jackson (1983)].

The model in Fig. 15(c) can also be used to calculate the horizontal components of the moment rate tensor $\dot{\mathbf{M}}$. The contribution $d\dot{\mathbf{M}}^n$ that slip on an area dA between the nth and $(n+1)$th slats makes to $\dot{\mathbf{M}}$ given by

$$d\dot{\mathbf{M}}^n = \mu dA(\mathbf{V}^n\hat{\mathbf{n}} + \hat{\mathbf{n}}\mathbf{V}^n), \tag{31}$$

where μ is the shear modulus, and $\hat{\mathbf{n}}$ the normal to the fault plane. This sign convention gives the slip vectors in the direction shown in Fig. 16. If all faults between slats dip towards the top of the figure at an angle θ, then

$$\hat{\mathbf{n}} = (-\sin\theta\sin\phi_1, \sin\theta\cos\phi_1, \cos\theta), \tag{32}$$

$$\hat{\mathbf{n}} = (-\sin\theta\sin\phi_2, -\sin\theta\cos\phi_2, \cos\theta), \tag{33}$$

for the left and right slats respectively, and

$$dA = \frac{tds}{\sin\theta}, \tag{34}$$

where t is the thickness of the brittle zone and ds is an element of length measured along the slat. Substitution into equation (31) then gives

$$d\dot{\mathbf{M}}^n = \mu tds \times \begin{pmatrix} -2V_x^n\sin\phi_1 & V_x^n\cos\phi_1 - V_y^n\sin\phi_1 \\ V_x^n\cos\phi_1 - V_y^n\sin\phi_1 & 2V_y^n\cos\phi_1 \end{pmatrix}, \tag{35}$$

$$d\dot{\mathbf{M}}^n = -\mu tds \times \begin{pmatrix} 2V_x^n\sin\phi_2 & V_x^n\cos\phi_2 + V_y^n\sin\phi_2 \\ V_x^n\cos\phi_2 + V_y^n\sin\phi_2 & 2V_y^n\cos\phi_2 \end{pmatrix}, \tag{36}$$

for the left and right slats respectively. Integration over each boundary between slats, followed by summation over all boundaries, gives

$$\dot{M}_{11} = -\mu tB_L a_1^2 N\,\Delta x, \tag{37}$$

$$\dot{M}_{22} = \frac{\mu ta_1}{\tan\phi_1}\left[\left(-\frac{B_L a_1}{\tan\phi_1} - 2\Omega_1 + 2A_L\right)N\,\Delta x + B_L N^2\,\Delta x^2\right], \tag{38}$$

$$\dot{M}_{12} = -\frac{1}{2}\left(\frac{\dot{M}_{11}}{\tan\phi_1} + \dot{M}_{22}\tan\phi_1\right), \tag{39}$$

for the left slats, and

$$\dot{M}_{11} = \mu tB_R a_2^2 N\,\Delta x, \tag{40}$$

$$\dot{M}_{22} = -\frac{\mu ta_2}{\tan\phi_2}\left[\left(\frac{2B_R a_2}{\tan\phi_1} + \frac{B_R a_2}{\tan\phi_2} - 2\Omega_1 + 2A_R\right)N\,\Delta x + B_R N^2\,\Delta x^2\right], \tag{41}$$

$$\dot{M}_{12} = \frac{1}{2}\left(\frac{\dot{M}_{11}}{\tan\phi_2} + \dot{M}_{22}\tan\phi_2\right), \tag{42}$$

for the right slats. All these expressions depend only on $N\,\Delta x$, the distance between the screws through the first and the last slat measured along the x axis. Provided $N\,\Delta x$ is constant, the moment rate tensors are therefore independent of the number of slats within the deforming zone. The values of the constants in Fig. 16 give

$$\dot{M}_{11} = 3613\mu t, \quad \dot{M}_{12} = -2776\mu t, \quad \dot{M}_{22} = 2001\mu t \quad \text{N m yr}^{-1} \tag{43}$$

for the left slats, and

$$\dot{M}_{11}7227\mu t, \quad \dot{M}_{12} = -12650\mu t, \quad \dot{M}_{22} = -7925\mu t \quad \text{N m yr}^{-1} \tag{44}$$

for the right slats.